NTNU – Trondheim
Norwegian University of
Science and Technology

Numerical Modelling of Irregular waves and Irregular Wave Forces with REEF3D

Ankit Aggarwal

Coastal and Marine Engineering and Management
Submission date: June 2015
Supervisor: Øivind Asgeir Arntsen, BAT
Co-supervisor: Hans Bihs, BAT
Arun Kamath, BAT

Norwegian University of Science and Technology
Department of Civil and Transport Engineering

Masters Thesis

NTNU
Norwegian University of
Science and Technology
Faculty of Engineering Science and Technology
Department of Civil and Transport Engineering

Ankit Aggarwal

Numerical Modelling of Irregular Waves and Irregular Wave Forces using REEF3D

Trondheim, 29 June 2015

NTNU
Norwegian University of
Science and Technology

ERASMUS MUNDUS MSC PROGRAMME
COASTAL AND MARINE ENGINEERING AND MANAGEMENT
(COMEM)

Numerical Modelling of Irregular Waves and Irregular Wave Forces using REEF3D

Norwegian University of Science and Technology, Trondheim, Norway
29th June 2015

ANKIT AGGARWAL
746234

The Erasmus Mundus MSc Coastal and Marine Engineering and Management is an integrated programme organized by five European partner institutions, coordinated by Norwegian University of Science and Technology (NTNU). The joint study programme of 120 ECTS credits (two years full-time) has been obtained at least two of the five CoMEM partner institutions:

- Norwegian University of Science and Technology (NTNU) Trondheim, Norway
- Technische Universiteit (TU) Delft, The Netherlands
- City University London, Great Britain
- Universitat Politècnica de Catalunya (UPC), Barcelona, Spain
- University of Southampton, Southampton, Great Britain

The full range of distinctive skills offered by the five partners is brought together: these can only be accessed by student mobility. Thus CoMEM is divided into five tracks (specialisations): 1: Arctic Marine Coastal Engineering (NTNU); 2: Marine Operations and Management (City, London); 3: Environment and Management (Southampton); 4: Coastal Engineering (TU Delft); 5: Engineering and Environment (UPC, Barcelona). During semester 1, all students attend NTNU for a common foundation suitable for the five different tracks. Courses are taken with a focus on advanced topics in the selected area of specialization.

In the fourth and final semester an MSc project and thesis have to be completed. The two year CoMEM programme leads to two/three officially recognized MSc diploma certificates. These will be issued by the two/three universities which have been attended by the student. The transcripts issued with the MSc Diploma Certificate of each university include grades/marks for each subject. A complete overview of subjects and ECTS credits is included in the Diploma Supplement, as received from the CoMEM coordinating university, the Norwegian University of Science and Technology (NTNU). Information regarding the CoMEM programme can be obtained from the programme coordinator

Professor Øivind A. Arntsen
Department of Civil and Transport Engineering
Norwegian University of Science and Technology (NTNU)
NO-7491 Trondheim, Norway
E-mail: comem@ivt.ntnu.no

NORWEGIAN UNIVERSITY OF SCIENCE AND TECHNOLOGY
DEPARTMENT OF CIVIL AND TRANSPORT ENGINEERING

Report Title:	Date: 29/06/2015			
	Number of pages (incl. appendices): 76			
Numerical Modelling of Irregular Waves and Irregular Wave Forces using REEF3D	Master Thesis ✓		Project Work	
Name: Ankit Aggarwal				
Professor in charge/supervisor: Dr. Øivind Asgeir Arntsen				
Other external professional contacts/supervisors: Dr. Hans Bihs, PhD stipendiat Arun Kamath				

Abstract:
This thesis presents the validation of irregular wave generation and propagation using the numerical wave tank in the open-source CFD model REEF3D. The numerical model has been extensively used to study wave hydrodynamics and interaction with structures using regular waves. The numerical model solves the Reynolds-Averaged Navier Stokes (RANS) equations in three dimensions. A conservative finite difference scheme is employed on a staggered grid. Convective terms are discretized using the WENO scheme and time discretization is done using the third-order TVD Runge Kutta Scheme. The adaptive time stepping technique is used to ensure the stability of the solution. The projection method is used to compute the pressure term in the RANS equation. Turbulence modelling is done using the k – ω model. The level set method is employed for the modelling of the free surface. Waves are generated using the relaxation technique. The ghost cell immersed boundary method is used to implement complex geometries in the numerical model. The numerical code is parallelized to make the numerical model faster and more effective. The Message Passing Interface (MPI) is used for the exchange of the ghost cell values.
In the present work, irregular waves are generated and validated in REEF3D. In the model, irregular waves are based on the either on the Pierson-Moskowitz (PM) spectrum or the Joint North Sea Wave Observation Project (JONSWAP) spectrum. The effect of the grid size, the number of wave components and the length of the simulation on the generated wave spectrum in the wave tank is investigated. In addition, the influence of the spectral peak period on the requirements for the grid size and the length of the simulations is also studied. The numerical model is also validated with experimental observations to study the wave hydrodynamics of irregular waves for a submerged bar (Beji and Battjes, 1993). Two cases, breaking waves and non- breaking waves, are investigated. The numerical model shows a good agreement with the experimental results.
The next section of the study deals with the study of wave forces for a horizontal and a vertical submerged cylinder. For the horizontal cylinder case, numerical simulations are performed with different grid sizes to study the effect of grid sizes and then comparison is made with experimental data. Numerical tests are also done for different KC numbers. A simulation for a case with regular waves is also run and compared with the experiments. (Chaplin and Subbiah, 1997). For a vertical circular cylinder, different grid sizes are tested. Later, the effect of the peak time period Tp on the wave forces is also studied.
This study is concluded with a comparison between the regular and the irregular wave force spectra for the vertical cylinder case. It illustrates that the longer waves tend to have a higher force on submerged horizontal and vertical cylinders. Regular waves with the same wave height, H and time period, T corresponding to the significant wave height Hs and peak wave period Tp for the irregular waves have a higher peak value in the force spectrum.

Keywords:

1. Irregular waves
2. Wave forces
3. REEF3D
4. Numerical modelling

Ankit

Numerical Modelling of Irregular Waves and Irregular Wave Forces using REEF3D

A Masters' Thesis
submitted to the Faculty of Civil & Transport Engineering
at the Norwegian University of Science and Technology

by

Ankit Aggarwal

Acknowledgements

This thesis work is done as per the requirement for a graduate student in the two year mobility, Erasmus Mundus Masters Course: Coastal and Marine Engineering and Management (CoMEM). This thesis work is done at the Department of Civil and Transport Engineering, NTNU. Thereby I would like to give my sincere thanks to the department and supporting staff providing the work place and all the support.

I am grateful to Associate Professor Øivind Arnsten and Dr. Hans Bihs, for giving me the opportunity to work on REEF3D at the Department of Civil and Transport Engineering (BAT), Norwegian University of Science and Technology (NTNU). I would also like to express my wholehearted thanks to PhD stipendiat and co-supervisor Arun Kamath who helped me to understand my work better, spot my mistakes in time and for helping me to compile this document using LaTeX.

Last but not the least, I would like to thank Mrs Sonja Marie Ekrann Hammer and Mariette van Tillburg for all her support in administrative issues related to the COMEM MSc program.

Contents

1 Introduction **1**
1.1 Wave Hydrodynamics and Computational Fluid Dynamics 1
1.2 Objectives of the study 4

2 Numerical Model **5**
2.1 Governing Equations 5
2.1.1 Navier-Stokes Equations 5
2.2 Numerical Methodology 6
2.2.1 Discretization Methods 6
2.2.2 Convection Discretization 8
2.3 Time Discretization 11
2.4 Adaptive Time Stepping 11
2.5 Solution of the Navier Stokes Equation 12
2.6 Iterative Solver 13
2.7 Turbulence Modelling 13
2.8 Modelling of the Free Surface 15
2.8.1 Reinitialization 17
2.9 Immersed Boundary 17
2.10 Parallelization 18

3 Numerical Wave Tank **20**
3.1 Relaxation Method 21
3.2 Wave Theories 21
3.2.1 Linear Wave Theory 22
3.3 Irregular Waves 23
3.3.1 Direct analysis of the irregular waves 24
3.3.2 Spectral analysis of the irregular waves 24
3.3.3 Rayleigh Distribution 25
3.4 Irregular Wave Generation 26
3.5 Conversion of free surface elevation to spectrum 28
3.5.1 Fast Fourier Transformation 28

4 Validation for irregular waves in the numerical wave tank **30**
4.1 Setup of the Numerical Wave Tank 30
4.1.1 Study with the different grid sizes 31
4.1.2 Effect of number of waves 33
4.1.3 Generation of different peak periods 35
4.1.4 Effect of length of simulation time 38
4.2 Irregular wave propagation over a submerged bar 42
4.2.1 Experimental Setup 43
4.2.2 Numerical Setup 43
4.2.3 Case 1: Non-breaking Irregular Waves 44
4.2.4 Case 2: Breaking Irregular Waves 44

5 Wave forces on a horizontal cylinder **48**
5.1 Different kinds of the wave forces on the structures 48
5.1.1 Morison Formula 49
5.2 Force Calculation in REEF3D 49
5.3 Numerical wave tank setup 49
5.4 Validation with regular waves 50
5.5 Irregular Waves 52
5.5.1 Validation with the experiment and grid convergence tests . . 52
5.5.2 Testing with different KC numbers 55

6 Wave forces on a vertical cylinder **59**
6.1 Numerical Wave Tank Setup 59
6.2 Validation with the regular waves 60
6.3 Irregular waves: grid convergence study 60
6.4 Different Peak Periods 64
6.5 Comparison between irregular wave force and regular wave force . . . 65

7 Conclusions and outlook **68**
7.1 Conclusions 68
7.2 Outlook 70

List of Figures

2.1 Stencil for the FOU scheme 8
2.2 Ghost Cell Immersed Boundary 18
2.3 Exchange of data between inter-processor ghost points 19

3.1 Shapes of Relaxation Functions in different zones of NWT 22

4.1 Setup of the Numerical Wave Tank 30
4.2 $T_p = 1.18$ s, $N = 25$, $H_s = 0.02$ m, $dx = 0.05$ m 31
4.3 T_p=1.18 s, $N = 25$, H_s =0.02 m, $dx = 0.025$ m 32
4.4 $T_p = 1.18$ s, $N = 25$, H_s= 0.02 m, $dx = 0.01$ m 33
4.5 $T_p = 1.18$ s, $dx = 0.01$ m, $H_s = 0.02$ m, $N = 25$ 34
4.6 $T_p = 1.18$ s, $dx = 0.01$ m, $H_s = 0.02$ m, $N = 100$ 34
4.7 $dx = 0.01$ m, $H_s = 0.02$ m, $N = 25$ 35
4.8 $N = 25$, $dx = 0.01$ m, $H_s = 0.02$ m, $T_p = 2.5$ s 36
4.9 $N = 25$, $dx = 0.01$ m, $H_s = 0.02$ m, $T_p = 2.0$ s 37
4.10 $N = 25$, $dx = 0.01$ m, $H_s = 0.02$ m, $T_p = 1.18$ s 37
4.11 $N = 25$, $dx = 0.01$ m, $H_s = 0.02$ m, $T_p = 0.8$ s 38
4.12 Scaled up free surface elevation with horizontal velocity contours in NWT for $N = 25$, $dx = 0.01$ m, $H_s = 0.02$ m, $T_p = 2.5$ s 38
4.13 Scaled up free surface elevation with horizontal velocity contours in NWT for $N = 25$, $dx = 0.01$ m, $H_s = 0.02$ m, $T_p = 1.18$ s 38
4.14 $N = 25$, $T_p = 1.18$ s, $dx = 0.01$ m, $H_s = 0.02$ m, Simulation time = 60 s 39
4.15 $N = 25$, $T_p = 1.18$ s, $dx = 0.01$ m, $H_s = 0.02$ m, Simulation time = 120 s 40
4.16 $N = 25$, $T_p = 1.18$ s, $dx = 0.01$ m, $H_s = 0.02$ m, Simulation time = 240 s 40
4.17 $N = 25$, $T_p = 1.18$ s, $dx = 0.01$ m, $H_s = 0.02$ m, Simulation time = 500 s 41
4.18 $N = 25$, $T_p = 1.18$ s, $dx = 0.01$ m, $H_s = 0.02$ m, Simulation time = 1000 s 41
4.19 $N = 25$, $T_p = 1.18$ s, $dx = 0.01$ m, $H_s = 0.02$ m, Simulation time = 3600 s 42
4.20 Numerical setup with the wave gauge positions for a submerged bar in the numerical wave tank 43
4.21 $T_p = 2.5$ s, $dx = 0.01$ m, $H_s = 0.022$ m, Simulation time = 500 s . . . 45

4.22 $T_p = 2.5$ s, $dx = 0.01$ m, $H_s = 0.05$ m, Simulation time = 500 s . . . 46
4.23 $T_p = 2.5$ s, $dx = 0.01$ m, $H_s = 0.05$ m, Simulation time = 500 s . . . 47

5.1 The Numerical Wave Tank setup of a horizontal cylinder 50
5.2 Free surface elevation before and after the cylinder for the regular waves at WG3 and WG4 respectively, for $D = 0.21$ m, $dx = 0.05$ m, $H = 1.08$ m, $T = 3.5$ s, Simulation time = 500 s 51
5.3 Wave spectra before and after the cylinder at WG3 and WG4 respectively, for $D = 0.21$ m, $dx = 0.05$ m, $H = 1.08$ m, $T = 3.5$ s, Simulation time = 500 s 51
5.4 Comparison between experimental and numerical results for regular waves with $D = 0.5$ m, $dx = 0.05$ m, $H = 1.08$ m, $T = 3.5$ s 52
5.5 Grid convergence in comparison with experimental results for $D = 0.21$ m, $T_p = 5.9$ s, $H_s = 1.5$ m, KC number = 11.12, Simulation time = 500 s 53
5.6 Free surface elevation before and after the cylinder at WG3 and WG4 respectively, for $D = 0.21$ m, $dx = 0.05$ m, $H_s = 1.5$ m, $T_p = 5.9$ s, KC number = 11.12, Simulation time = 500 s 54
5.7 Wave spectra before and after the cylinder at WG3 and WG4 respectively, for $D = 0.21$ m, $dx = 0.05$ m, $H_s = 1.5$ m, $T_p = 5.9$ s, KC number = 11.12, Simulation time = 500 s 54
5.8 Numerical results with the different KC numbers, $D = 0.21$ m, $dx = 0.05$ m, $H_s = 1.5$ m, Simulation time = 500 s 55
5.9 $T_p = 5.9$ s, $dx = 0.05$ m, $H_s = 1.5$ m, Simulation time = 500 s 56
5.10 $T_p = 3.2$ s, $dx = 0.05$ m, $H_s = 1.5$ m, Simulation time = 500 s 58

6.1 Numerical Wave Tank Setup for Vertical Cylinder 60
6.2 Comparison of numerical force with Morison's force for a vertical cylinder of $D = 0.5$ m for T=1.2s, $dx = 0.025$ m, $H = 0.03$ m 60
6.3 Grid Convergence Study for a Vertical Submerged Cylinder with $D = 0.5$ m, $T_p = 1.2$ s, $H_s = 0.03$ m 61
6.4 $D = 0.5$ m, $T_p = 1.2$ s, $dx = 0.05$ m, $H_s = 0.03$ m, Simulation time = 500 s 63
6.5 Study with different peak wave periods, T_p for a vertical cylinder with $D = 0.5$ m, $dx = 0.025$ m, $H_s = 0.03$ m 65
6.6 Comparison of wave spectra before and after the interaction with vertical cylinder of $D = 0.5$ m for T=1.2s, $dx = 0.025$ m, $H = 0.03$ m . 66
6.7 Comparison between Regular and Irregular Wave Force Spectra with $D = 0.5$ m, $dx = 0.05$ m 66

List of Symbols

λ	Wavelength
D	Diameter
ρ	Density
t	Time
∇	Divergence operator
U	Velocity
$_{i,\ j,\ k}$	Vectors along the x, y and z-axes
μ	Fluid viscosity (dynamic)
P	Pressure
g	Acceleration due to gravity
ϕ	Level set function
i (*in numerical schemes*)	Time step of iteration
$\omega_1,\ \omega_2,\ \omega_3$	WENO stencil weights
$\alpha_1,\ \alpha_2,\ \alpha_3$	WENO stencil weight determiner
$IS_1,\ IS_2,\ IS_3$	WENO stencil smoothness indicators
L	Spatial discretization of the function
C	Courant Number
ν	Fluid viscosity(kinematic)
ν_t	Eddy viscosity
V	Maximum viscosity
S_{max}	Source term contribution from surface and volume forces
U^*	Intermediate velocity
k	Turbulent kinetic energy
ω	Specific turbulent dissipation
$c_\mu,\ c_{\omega 1},\ c_{\omega 2},\ \sigma_k,\ \sigma_\omega$	Closure coefficients
S_{ij}	Strain tensor
ω_s	Specific turbulent dissipation at free surface
U^+	Dimensionless wall velocity
y^*	Distance from the nearest wall for a smooth transition
κ	constant = 0.4
d	Water depth
k_s	Equivalent sand roughness

Δy_p	Distance from the wall to cell centre
ϵ_{wall}	Mean wall thickness
2ϵ	Transition zone thickness
$S(\phi)$	Smooth signed distance function
Φ	Velocity potential
$\Psi(x)$	Relaxation function
$_p$	Steepness exponent
η	Free surface elevation
ω_f	Wave angular frequency
k_f	Wave number
a	Wave amplitude
H	Wave height
H_s	Significant wave height
$H_{1/3}$	Highest of one third of the wave heights
H_{rms}	Root mean squared wave height
z	Height to the free surface from bed
dx	Grid cell width
KC	Keulegan-Carpenter number
T	Wave period
T_p	Peak wave period
T_0	Zero crossing wave period
σ	Standard deviation
m_0	Zeroth spectral moment
$p(H)$	Probability density function
$S(f)$	Spectral wave energy
S_p	Peak spectral wave energy
f_p	Peak frequency
N	Number of linear wave components
F	Wave force
Re	Reynolds number
x, y, z	Position of structure in the flume
Δt	Numerical time step

Chapter 1

Introduction

1.1 Wave Hydrodynamics and Computational Fluid Dynamics

Marine civil engineering involves the study of irregular and regular wave propagation and hydrodynamics, study of wave interaction with structures, wave propagation over submerged and emerged structures, study of phenomenon like shoaling, refraction, diffraction and reflection during the wave-structure interaction. Wave propagation is the way in which waves travel. The particles in the water execute a circular motion as the wave passes without significant net advance in their position. The motion of the water is forth and back with the crest and trough of the wave, respectively. Experiments show a slight advance of the water in wave direction, but that advance is small compared to the overall circular motion (Von Arx, 1962). Bascom (1964) described the wave tank experiments in which the circulation of the water was studied.
Various wave theories are used to represent wave and understand hydrodynamics by various researchers namely linear wave theory, 2nd-order, 3rd-order and 5th-order Stokes theory, cnoidal wave theory and solitary wave theory to study regular waves. Linear wave theory is the earliest and simplest wave theory. The linear wave theory is based on the assumption that the wave amplitude is small and the waveform is invariant in time and space. Higher-order non-linear wave theories like Stokes wave theory given by Stokes (1846) overcome some limitations of the linear wave theory. It can be used directly for intermediate and deep water for practical applications. 2nd-order Stokes wave theory can be used for slightly steeper waves. For the further increase in wave steepness, 3rd-order and 5th-order Stokes theory can be used. Cnoidal wave theory is a non-linear wave theory which describes shallow water waves, where the wavelength is fairly large compared to the water depth. These wave theories describe the periodic waves and help in understanding the various wave propagation and interaction problems. In reality, the sea state is random, consisting of waves of different periods, amplitudes and directions. A complete 3D representation of the ocean waves requires the consideration of the sea surface as an irregular wave train with the random characteristics. The random sea surface using Fourier theory can be

transferred into the summation of simple sine waves and then wave characteristics in terms of its spectrum are defined. This allows treatment of the variability of waves with respect to the period and the direction of travel. Irregular waves are defined by frequency spectra like the Pierson Moskowitz (PM) and the Joint North Sea Wave Observation Project (JONSWAP) wave spectra. A wave frequency spectrum represents the distribution of wave energy with respect to the wave frequency. Within certain approximations, all the required properties of the wave can be computed by the spectrum for the fully developed and the young sea state (Arntsen and Krogstad, 2000).

Physical modelling of irregular waves is time consuming and expensive. To study such a complex phenomenon, another option available is numerical modelling. With the aid of numerical modelling real life phenomena can be simulated. Thus, numerical simulations are practical for calculating and studying the wave hydrodynamics. The recent advancements in the computational power of computers, have made it possible to carry out 3D simulations in an acceptable amount of time. There are many numerical models available. The choice of the model depends on the required detail and accuracy. Spectral wave model like SWAN are used for modelling of the large scale processes. The modelled waves are phase averaged in spectral wave models. This describes the wave spectrum evolution in space and time based on the wave energy balance. Rogers et al. (2007) and Xu et al. (2007) have used these models in the past to study the coatsal engineering problems. Numerical models detailing phase information are also available, these models are based on the Boussinesq equations (Nwogu, 1993) and (Madsen et al., 1991). These models can model hydrodynamic phenomena like reflection and diffraction. Fully Nonlinear Potential Flow Models (FNPF) models are also available in the literature. Here, the Laplace equation for the potential flow is solved. This methods neglects the viscosity and rotational flow effects. This has been used in the past by Dommermuth et al. (1988) to study of wave propagation in deep water.

But for studying complex phenomena like the breaking waves or the flow around a cylinder, more detailed solutions are required in order to capture the flow properties. Solving the Navier-Stokes equation in 3D gives a more detailed solution. In this approach, hydrodynamics can be studied by calculations based on the 3D flow field by employing suitable interface capturing techniques for the free surface. Computational fluid dynamics cover the range from the automation of well-established engineering design methods to the use of detailed solutions of the Navier-Stokes equations as substitutes for the experimental research into the nature of complex flows. Several successful investigations are done to use a CFD program as numerical tank. Higuera et al. (2013) and Jacobsen et al. (2011) used the CFD based numerical model OpenFOAM, which calculates the free surface with a Volume-of-Fluid approach based on convection of the fraction function and interface compression. Such CFD based numerical models were applied to laboratory experiments and they showed that with today's available computational resources, complex wave propagation simulations can be performed (Paulsen et al., 2014),(Seiffert et al., 2014).

The present study uses the open-source model REEF3D (Chella et al., 2015) to study

the irregular wave propagation. The appropriate numerical techniques are used in REEF3D in order to ensure a good performance with a focus on the numerical stability and accuracy criteria. REEF3D uses a staggered Cartesian grid and the Weighted Essentially Non-Oscillatory (WENO) scheme for convection discretization (Jiang and Peng, 2000). Time discretization is done using a high-order method with third-order total variation diminishing (TVD) Runge-Kutta scheme (Shu and Oscher, 1988). The Level Set method is used for computing the free surface. Waves are generated using the relaxation method. Ghost cell immersed boundary method is used to implement complex geometries in the numerical model. The numerical code is parallelized to make numerical model faster and more effective. The Message Passing Interface (MPI) is used for the exchange of the value of a ghost cell. As a result, REEF3D can calculate the wave propagation and transformation throughout the wave steepness range up to the point of wave breaking and beyond, with no artificially high air velocities impacting the quality of free surface.

Some experimental and numerical investigations have been carried out in the past to understand the irregular wave propagation and their behaviour during the interaction with the structures. Wheeler (1970) calculated the irregular wave force for risers. Goda and Suzuki (1976) used FFT analysis for random wave experiments. In their study, the amplitudes of the incident and the reflected wave components were estimated from the Fourier components. Later, Rainey (1989) calculated irregular wave loads on offshore structures. An equation for the potential-flow wave loading on a lattice-type offshore structure partially immersed in waves was derived. The incident and reflected wave spectra were constructed by smoothing the estimated periodograms. Beji and Battjes (1993) studied the hydrodynamics of the irregular wave propagation over a submerged bar. The experiments with irregular waves in shallow water depth for the design wave height estimation were carried out by J. William Kamphuis (1996). Attempts have also been made to calculate the wave force on cylinder due to irregular waves apart from the study of irregular wave hydrodynamics. Chaplin and Subbiah (1997) carried out experiments to calculate the wave forces on a horizontal rectangular submerged cylinder. Suryanto (2006) estimated the incident and the reflected waves in with irregular waves. The decomposition of the irregular waves was performed by comparing the general solution of the linear wave equation and the wave elevation measured at some fixed positions. Goullet and Choi (2011) did a numerical and an experimental study on the nonlinear evolution of long-crested irregular waves. Later, in the same year, remote sensing study of irregular waves was also done by Harry et al. (2011). Recently, Shekari and M. (2013) did an experimental study on the reshaping of berm breakwaters under irregular wave attacks.

Little work has been done in the past to study the irregular waves using CFD models. As mentioned above, CFD gives a more detailed and accurate solution of the water wave dynamics. The present thesis work uses an open-source numerical model REEF3D to study the irregular waves. The present study is focused on the validation of irregular wave generation and propagation in REEF3D. The numerical results are compared with experimental observations in chapter 3 to study the wave propagation

over a submerged bar. Later, in chapters 5 and 6, wave forces are computed on a horizontal and a vertical cylinder, respectively.

1.2 Objectives of the study

- The first objective of the present work is to test and validate irregular wave generation and propagation in the numerical model REEF3D, by varying the various hydrodynamic and numerical parameters like the grid size, dx, the peak time period, T_p, the number of linear wave components, N, the length of simulation duration, t and to study their effect on the results.

- The second objective is to study the irregular wave propagation over a submerged bar and then to compare the numerical results with the experimental results for JONSWAP spectra for different cases.

- The last objective of the present work is to study the wave forces on a horizontal and a vertical cylinder due to irregular waves for different KC numbers and to validate the calculated numerical force spectrum with the experimental force spectrum results.

Chapter 2

Numerical Model

2.1 Governing Equations

2.1.1 Navier-Stokes Equations

The Navier-Stokes equations are the governing equations of Computational Fluid Dynamics (CFD). These are based on the basic equations of the fluid mechanics like the mass and the momentum conservation. The Navier-Stokes equations are defined with the assumption of an incompressible fluid. The mass conservation equation under this assumption is given by the continuity equation:

$$\frac{\partial U_i}{\partial x_i} = 0 \tag{2.1}$$

The momentum conservation together with the continuity equation leads to the Navier-Stokes equations which provides a description of the flow (Batchelor, 1967):

$$\frac{\partial U_i}{\partial t} + U_j \frac{\partial U_i}{\partial x_j} = -\frac{1}{\rho}\frac{\partial P}{\partial x_i} + \frac{\partial}{\partial x_j}\left[\nu\left(\frac{\partial U_i}{\partial x_j} + \frac{\partial U_j}{\partial x_i}\right)\right] + g \tag{2.2}$$

where, U is the velocity averaged over time t, ρ is the fluid density, p is the pressure, ν is the kinematic viscosity, i and j denote the indices in x and y direction, respectively and g is the acceleration due to gravity.
Equation 2.2 has the following terms:

- The left hand side of the equation has a transient term given by a time derivative.
- The left hand side of the equation has a set of convection terms involving first order derivatives of the velocity components in the three coordinate directions.
- The right hand side of the equation has a diffusive term that involves a second derivative in all space dimensions of the per-unit-mass quantity in the balance equation. It is associated with the processes that tends to smooth out gradients in the flow.

- The right hand side of the equation contains terms, such as source and sink terms.

2.2 Numerical Methodology

2.2.1 Discretization Methods

There are many analytical techniques available for deriving solutions of partial differential equations. Most differential equations that model physical processes cannot be solved directly. This is due to non-linearity of coefficients, time-dependence of the coefficients or the higher-order of the equations. To solve these equations, approximation methods are used. These methods are used in such a way that most of the global/continuous information of the original problem and more importantly, the inherent structure, is retained.
The different discretization schemes address the task of replacing the partial differential equation system with algebraic ones. This is done using the finite difference method, the finite element method or the finite volume method.

- Finite Volume Method: The finite volume method was first used by Harlow and Evans (1957) and it makes use of the conservation laws in integral form. It subdivides the domain into cells and evaluates the field equations in integral form on these cells. The concepts and implementation are simple for different dimensions and different types of cells. For the finite volume method the domain is first subdivided into non-overlapping control volumes of a cell. In each control volume an integral conservation law is imposed (Barth and Ohlberger (2004)).

- Finite Element Method: The finite element method is based on the projection of a given domain onto a consistent finite cell complex. Finite element method (FEM) was first used by Courant (1943). It is also used in the solid mechanics of rigid bodies, e.g., by Johnson (1987). A good approximation is obtained by a residual formulation where the residum is the difference of the unknown exact solution and the calculated approximate solution. This residuum is weighted over the simulation domain and integrated with the requirement that the integral vanishes with a set of linearly independent weighting functions.

- Finite Difference Method: The finite difference discretization scheme is one of the simplest forms of discretization given by Richardson (1910). A classical finite difference approach approximates the differential operators constituting the field equation locally. Therefore, a structured grid is required. For each of the points of the structured grid the differential operators appearing in the main problem specification are rendered in a discrete expression. The order of the differential operator of the original problem formulation directly dictates the number of nodes to be involved. The present study uses the finite difference method, in a conservative way, giving the same conservation properties as the finite volume

method. Also, this method is more straight forward to apply for higher order schemes. This way, finite difference method overcomes the drawbacks of the above mentioned methods. The derivatives in the partial differential equation are approximated by linear combinations of function values at the grid points. The domain is partitioned in space and in time and approximations of the solution are computed at the space or time points. The finite difference method optimizes the approximation for the differential operator in the central node of the considered patch.

Grids can be of two types: staggered grid and collocated grid. In a collocated grid arrangement, all of the variables are stored in the same positions, while in a staggered grid the scalar variables (pressure, density, total enthalpy etc.) are stored in the cell centers of the control volumes, whereas the velocity or momentum variables are located at the cell faces. A staggered storage is mainly used on structured grids for compressible or incompressible flow simulations. Using a staggered grid arrangement is a simple way to avoid odd-even decoupling between the pressure and velocity and thus, leads to a tight pressure-velocity coupling. Odd-even decoupling is a discretization error that can occur on collocated grids and which leads to checkerboard patterns in the solutions. Morinishi et al. (1998) analyzed the conservation properties of several finite-difference schemes for both staggered and collocated grid arrangements. By restricting the analysis to Cartesian uniform meshes, it was shown that staggered-mesh methods can be made fully-conservative, whereas collocated-mesh methods will always contain an energy conservation error. The following properties of the numerical solution should be satisfied for applicability to a particular problem:

- Stability: Stability of a numerical solution ensures that the error caused by a small perturbation in the numerical solution remains bounded. A stable method should not diverge with the time.

- Convergence: The finite-difference solution approaches the true solution to the partial differential equation as the increments $\Delta x, \Delta t$ go to zero. A solution is convergent if for any solution to the partial differential equation $u(t,x)$ and solutions to the finite difference scheme, v_{in}, such that $v_{i0} \to u_0(x)$ as $i\Delta x \to x$, then $v_{i0} \to u(t,x)$ as $(n\Delta t, i\Delta x) \to (t,x)$ as $\Delta x, \Delta t \to 0$.

- Consistency: A finite difference scheme or operator is consistent if the operator reduces to the original differential equation as the increments in the independent variables vanish. Given a partial differential equation $Pu = f$ and a finite difference scheme, $P(\Delta t, \Delta x)v = f$, we say that the finite difference scheme is consistent with the partial differential equation if for any smooth function $\phi(x,t)$:

$$P\phi - P_{\Delta t,\Delta x}\phi \to 0, when \Delta x, \Delta t \to 0 \tag{2.3}$$

2.2.2 Convection Discretization

As, discussed before, the Navier-Stokes equation consists of the convective terms. These terms are discretized first. The number of points used in the approximation schemes defines the order of accuracy and the nature of the scheme. The geometrical representation of these numerical points is called a stencil. A higher order of accuracy is obtained from a wider stencil. There are different types of the convection discretization schemes available:

- First Order Upwind (FOU) Scheme: This scheme given by Courant et al. (1952) is based on the solution-sensitive finite difference stencil to numerically simulate the flow information in the direction of the flow propagation. With such schemes shock waves can be captured without oscillations. Thus, a successful artificial dissipation model for a central-difference scheme should imitate an upwind scheme in the neighbourhood of shocks. It is desirable to develop numerical schemes that preserve monotonicity. Since the waveform propagates in one direction, it is appropriate to use an upwind one-sided finite difference for the spatial derivative. Stencil can be seen in the Figure 2.1. An example of FOU scheme is:

$$\frac{\partial U}{\partial x_j} = \frac{(U_i - U_{i-1})}{\Delta x_j}$$

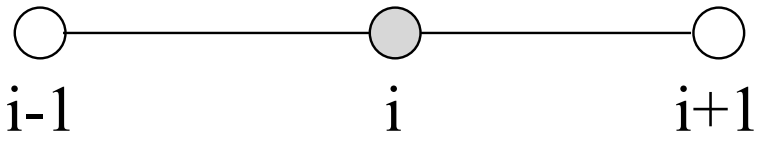

Figure 2.1: Stencil for the FOU scheme

  Δx_j represents spatial discretization in the direction perpendicular to velocity. This scheme is first order accurate in space and time. It also produces large numerical diffusion in case of large gradients. Thus, this scheme does not give good results when the flow direction is skewed relative to the grid lines.

- Central Difference Scheme (CDS): This method uses the points downstream and upstream of the point at which the values are calculated. It can be written as:

$$\frac{\partial U}{\partial x} = \frac{U_{i+1} - U_{i-1}}{2\Delta x}$$

  Δx represents spatial discretization. The truncation error of this scheme is of second order, thus this scheme is a second-order accurate scheme. This scheme is simper to program and needs less computational time per time step, and it is less dissipative as compared to FOU scheme. But, this scheme is unconditionally unstable for the damped systems and in case of large gradients making it impractical for the use in CFD codes..

- High-Resolution Schemes: These schemes uses flux limiters to avoid spurious oscillations in the results (Van Leer, 1979). This is used in higher-order spatial discretizations to overcome wiggles which might be introduced due to shocks or discontinuities in the solution domain. Flux limiters limit the spatial derivatives to their realistic values. They are used in the high resolution schemes and used in the case of sharp wave fronts or discontinuities. Flux limiter together with appropriate high resolution scheme leads to Total Variation Diminishing (TVD) properties. The major drawback of this scheme is that it does not work for the waves.

  For the present study which is focused on the irregular waves, none of the above techniques are able to give good numerical solutions. Thus, Weighted Essentially Non-Oscillatory (WENO) Scheme explained below is used in the present study. WENO scheme gives good results for discretizing the convective terms of the Navier-Stokes equation for the present kind of study.

- Weighted Essentially Non-Oscillatory (WENO) Scheme: The Weighted Essentially Non-Oscillatory (WENO) scheme is an extension of the Essentially Non-Oscillatory (ENO) Scheme. The first ENO scheme is given by Harten et al. (1987). The ENO scheme is an adaptive stencil scheme to obtain a non-mesh size dependent parameter, uniformly high order accurate yet essentially non-oscillatory interpolation for piecewise smooth functions. Later, Liu et al. (1994) introduced a scheme of choosing multiple stencils and assigning the weight factors, accordingly using a convex combination of all candidate stencils instead of just one as in the original ENO. ENO and WENO schemes for Hamilton-Jacobi type equations were designed and applied in Osher and F. (1996), Osher and Sethian (1988a) and Osher and Shu (1991). The third and fifth-order finite difference WENO schemes in a multi space dimensions were constructed by Jiang and Peng (2000), with a general framework for the design of the smoothness indicators and the nonlinear weights. A key idea in the WENO schemes is a linear combination of the lower order fluxes or the reconstruction to obtain a higher order approximation. Here, a nonlinear adaptive procedure is used to automatically choose the locally smoothest stencil, hence avoiding crossing the discontinuities in the interpolation procedure as far as possible. An example of the implementation of this scheme in the Hamilton-Jacobi form to the level set function, ϕ_x in x-direction is presented as:

$$\phi_x = \begin{cases} \phi_x^- & if\ U_1 > 0 \\ \phi_x^+ & if\ U_1 < 0 \\ 0 & if\ U_1 = 0 \end{cases} \tag{2.4}$$

  The WENO approximation for a given level set function might be a combination of three possible approximations:

$$\phi_x^{\pm} = \omega_1^{\pm}\phi_x^{1\pm} + \omega_2^{\pm}\phi_x^{2\pm} + \omega_3^{\pm}\phi_x^{3\pm} \tag{2.5}$$

The three ENO stencils defined for ϕ are

$$\begin{aligned}\phi_x^{1\pm} &= \frac{q_1^{\pm}}{3} - \frac{7q_2^{\pm}}{6} + \frac{11q_3^{\pm}}{6} \\ \phi_x^{2\pm} &= -\frac{q_2^{\pm}}{6} + \frac{5q_3^{\pm}}{6} + \frac{q_4^{\pm}}{3} \\ \phi_x^{3\pm} &= \frac{q_3^{\pm}}{3} + \frac{5q_4^{\pm}}{6} - \frac{q_5^{\pm}}{6}\end{aligned} \tag{2.6}$$

with,

$$\begin{aligned}q_1^- &= \frac{\phi_{i-2} - \phi_{i-3}}{\Delta x},\ q_2^- = \frac{\phi_{i-1} - \phi_{i-2}}{\Delta x},\ q_3^- = \frac{\phi_i - \phi_{i-1}}{\Delta x}, \\ q_4^- &= \frac{\phi_{i+1} - \phi_i}{\Delta x},\ q_5^- = \frac{\phi_{i+2} - \phi_{i+1}}{\Delta x}\end{aligned} \tag{2.7}$$

and

$$\begin{aligned}q_1^+ &= \frac{\phi_{i+3} - \phi_{i+2}}{\Delta x},\ q_2^+ = \frac{\phi_{i+2} - \phi_{i+1}}{\Delta x},\ q_3^+ = \frac{\phi_{i+1} - \phi_i}{\Delta x}, \\ q_4^+ &= \frac{\phi_i - \phi_{i-1}}{\Delta x},\ q_5^+ = \frac{\phi_{i-1} - \phi_{i-2}}{\Delta x}\end{aligned} \tag{2.8}$$

the weights are written as:

$$\omega_1^{\pm} = \frac{\alpha_1^{\pm}}{\alpha_1^{\pm} + \alpha_2^{\pm} + \alpha_3^{\pm}},\quad \omega_2^{\pm} = \frac{\alpha_2^{\pm}}{\alpha_1^{\pm} + \alpha_2^{\pm} + \alpha_3^{\pm}},\quad \omega_3^{\pm} = \frac{\alpha_3^{\pm}}{\alpha_1^{\pm} + \alpha_2^{\pm} + \alpha_3^{\pm}}, \tag{2.9}$$

and

$$\alpha_1^{\pm} = \frac{1}{10}\frac{1}{\left(\widetilde{\epsilon} + IS_1^{\pm}\right)^2},\quad \alpha_2^{\pm} = \frac{6}{10}\frac{1}{\left(\widetilde{\epsilon} + IS_2^{\pm}\right)^2},\quad \alpha_3^{\pm} = \frac{3}{10}\frac{1}{\left(\widetilde{\epsilon} + IS_3^{\pm}\right)^2} \tag{2.10}$$

with the regularization parameter $\widetilde{\epsilon} = 10^{-6}$ in order to avoid division by zero and the following smoothness indicators:

$$\begin{aligned}IS_1^{\pm} &= \frac{13}{12}\left(q_1 - 2q_2 + q_3\right)^2 + \frac{1}{4}\left(q_1 - 4q_2 + 3q_3\right)^2, \\ IS_2^{\pm} &= \frac{13}{12}\left(q_2 - 2q_3 + q_4\right)^2 + \frac{1}{4}\left(q_2 - q_4\right)^2, \\ IS_3^{\pm} &= \frac{13}{12}\left(q_3 - 2q_4 + q_5\right)^2 + \frac{1}{4}\left(3q_3 - 4q_4 + q_5\right)^2\end{aligned} \tag{2.11}$$

The WENO scheme is successfully used to simulate shock turbulence interactions by Adams and Shariff (1996), Shu and Oscher (1989), Shu et al. (1992); to the direct simulation of compressible turbulence by Shu et al. (1992), Walsteijn (1994), Ladeinde et al. (1995); to relativistic hydrodynamics equations by Erlebacher et al. (1997); to shock vortex interactions and other gas dynamics problems by Erlebacher et al. (1997), Jiang and Shu (1996); to incompressible flow problems by Weinan and Shu (1994) etc.

2.3 Time Discretization

In wave hydrodynamics, the flow properties change over small time scales, making a good time discretization scheme necessary. The time discretization is done through integration over time on the general discretized equation. The time integral of a given variable is equal to a weighted average between current and future values. It can be implicit and explicit. When a direct computation of the dependent variables can be made in terms of known quantities, the computation is said to be explicit. When the dependent variables are defined by coupled sets of equations, and either a matrix or an iterative technique is needed to obtain the solution, the numerical method is said to be implicit. Implicit schemes are stable over a wider range of time steps as compared to explicit schemes. REEF3D has the Adam-Bashforth, the third and the fourth order TVD Runge-Kutta schemes included in the code for the purpose of higher accuracy, as flow characteristics change rapidly over the time. The present study uses the third order TVD Runge-Kutta scheme.

- Third Order Total Variance Diminishing (TVD) Runge Kutta Scheme: This is an explicit 3^{rd} order scheme which rules out the spurious oscillations by suppressing the local extrema (Harten et al., 1987). An example of a such implementation is the third order TVD Runge Kutta scheme over a time step Δt (Shu and Oscher, 1988):

$$\begin{aligned} \phi^{(1)} &= \phi^n + \Delta t L\left(\phi^n\right) \\ \phi^{(2)} &= \frac{3}{4}\phi^n + \frac{1}{4}\phi^{(1)} + \frac{1}{4}\Delta t L\left(\phi^{(1)}\right) \\ \phi^{n+1} &= \frac{1}{3}\phi^n + \frac{2}{3}\phi^{(2)} + \frac{2}{3}\Delta t L\left(\phi^{(2)}\right) \end{aligned} \tag{2.12}$$

2.4 Adaptive Time Stepping

In order to obtain a good numerical solution, the numerical scheme should be stable. To ensure stability, the movement of the fluid is restricted to a one computational cell per time step. This is also called the Courant Condition (Courant et al., 1967):

$$\frac{U\Delta t}{\Delta x} \leq C \tag{2.13}$$

where, 'C' is a dimensionless constant depending on the scheme of discretization. While using temporal discretization schemes, limitation of size of time step is to be kept in mind. A larger time step might cause instability, a too small time step might cause inappropriate weighing on computations. In such situations, the most efficient way of obtaining good numerical solution is adaptive time stepping. The adaptive time stepping scheme (Griebel et al., 1998) uses the maximum values of the velocity, the viscosity, the volume forces and the surface forces for computing the time step

size:

$$\delta t \leq 2 \left(\left(\frac{|U|_{max}}{\delta x} + V \right) + \sqrt{\left(\frac{|U|_{max}}{\delta x} + V \right)^2 + \frac{4\,|S_{max}|}{\delta x}} \right)^{-1} \tag{2.14}$$

with

$$V = max\,(\nu + \nu_t) \cdot \left(\frac{2}{(\delta x)^2} + \frac{2}{(\delta y)^2} + \frac{2}{(\delta z)^2} \right) \tag{2.15}$$

where, 'V' is the maximum viscosity and 'S_{max}' is the source term contribution from the surface and the volume forces.

2.5 Solution of the Navier Stokes Equation

There are certain challenges in solving the Navier Stokes equations. The momentum conservation terms also contain a contribution from the pressure. It may be regarded as a source term (Peric and Ferziger, 2001). The pressure can not be determined directly. The involvement of non-linear terms makes the solution computationally expensive and implicit methods need to be used. The numerical model REEF3D offers different pressure solvers. They are projection method, projection method with pressure correction, Semi Implicit Method for Pressure Linked Equations (SIMPLE), SIMPLEC and PISO. The major difference between the various Projection Methods and the various SIMPLE techniques is that, former works well with explicit time advancement schemes, while latter works well with implicit time stepping schemes. The present study uses the Projection Method for solving the pressure.

- Projection Method

  The solution for the pressure in the Navier Stokes equations is obtained from the projection method given by Chorin (1968). The advantage of using this method is that it decouples the velocity and pressure field. An intermediate value of the velocity U_i^* is obtained by first neglecting the pressure gradient. An intermediate velocity is calculated using transient equation:

$$\frac{\partial (U^* - U_i^n)}{\partial t} + U_j^n \frac{\partial U_i^n}{\partial x_j} = \frac{\partial}{\partial x_j} \left[\nu(\phi^n) \left(\frac{\partial U_i^n}{\partial x_j} + \frac{\partial U_j^n}{\partial x_i} \right) \right] + g_i \tag{2.16}$$

  The calculated intermediate velocity does not fulfil the continuity requirements.

$$\frac{\partial (U_i^{n+1} - U_i^*)}{\partial t} + \frac{1}{\rho(\phi^n)} \frac{\partial P^{n+1}}{\partial x_i} = 0 \tag{2.17}$$

  The pressure term, P^{n+1}, is unknown in above equation. This unknown is calculated by using a divergence operator such that divergence of U_i^{n+1} is zero is applied. The Poisson pressure equation is written as:

$$\frac{\partial}{\partial x_i} \left(\frac{1}{\rho(\phi^n)} \frac{\partial P}{\partial x_i} \right) = -\frac{1}{\Delta t} \frac{\partial U_i^*}{\partial x_i} \tag{2.18}$$

Using the new value of the pressure and enforcing the continuity equation, the divergence-free value of the velocity for the next time step is determined.

2.6 Iterative Solver

To solve the above mentioned Poisson's equation (2.31) , different types of techniques are available. Direct methods are for example Gaussian elimination and iterative methods. But, it should be kept in mind that direct methods are computationally too expensive, thus iterative techniques are more efficient in such cases. There are various iterative techniques available like the Jacobi method, the Gauss-Seidel method, the Successive Over- Relaxation method, the Conjugate Gradients method, the Bi-Conjugate Gradient method, and the Multigrid method.

The Conjugate Gradient Method given by Hestenes and Stiefel (1952) is an iterative method for solving sparse systems of linear equations. In this technique, minimization of a function is done with respect to many directions simultaneously while searching in one direction at a time. It can be extended to non-quadratic unconstrained minimization. This works for a particular system of equations, where the matrix is symmetric and positive definite. But for non-symmetric equations like convection-diffusion equations, this method can not be applied.
The Bi Conjugated Gradient (BiCG) method was developed by Fletcher (1976). Unlike the Conjugated Gradient Method, this method can be used for non-symmetric equations. It does not require the matrix to be self-adjoint, but instead the conjugated transpose matrix is used. Thus, this method first converts non-symmetric systems into symmetric systems. It is twice as expensive as the Conjugated Gradient Method, but the convergence rate is about the same. The present study utilises the Bi Conjugate Gradient Stabilized (BiCGstab) method, which is a modified approach of BiCG. It is given by Van der Vorst (1992), it converges faster and produces more stable solutions. The present study utilises this approach for solving Poisson equation.

2.7 Turbulence Modelling

Wave-structure interaction gives rise to the turbulence in the flow. Turbulence is rotational and three dimensional. Turbulent flows are highly unsteady. Turbulent flows are always dissipative, generally more dissipative than laminar flows. Much of the energy is lost in viscous dissipation in the eddies of the smallest scales. The energy present in the turbulent motions is supplied by the mean flow. The length and time scales on which turbulent fluctuations play a role are far larger than the molecular scale. Turbulence will appear in flows where the energy can be transferred from the mean motion to the turbulent fluctuations. A turbulent fluctuation will induce a turbulent shear stress in the presence of a velocity gradient providing the conditions for energy transfer. The turbulence might produce the vortices in the flow

downstream of the structure. This phenomena effects the wave-structure interaction. In order to represent turbulence, the Navier-Stokes equations should be solved and all the details of the flow down to the smallest length scales should be represented on the numerical grid. Direct Numerical Simulation (DNS) can only be used as a research tool to study the details of low Reynolds number flows in simple geometries. For flows with a higher Reynolds number, several million grid points are needed in DNS which is practically not feasible.
An alternative approach in finding a solution is to average in space and in time. The large scale motion shows a strong anisotropy and contains the greater part of the turbulent kinetic energy. Once the large structures are broken up into the smaller scales via the energy cascade, they become more isotropic and lose their energy in self-similar processes that are not much affected by the large scale geometry. To be able to resolve the large-scale part of the energy spectrum on the numerical grid, the remaining isotropic small scale turbulence is less of a problem to model. The small scale motion is filtered out of the equations by filtering them over the volume of one or several grid-cells. The resulting filtered equation applies only to the large scale eddies and such modelling is called Large Eddy Simulation (LES). But, for real life flows, it is still computationally too expensive.
Another approach is the Reynolds-Average Navier-Stokes (RANS) equation. The small scales of turbulence are modelled with a subgrid scale model. For example. the smagorinsky model Peric and Ferziger (2001). This approach is less expensive because of the averaging and is suitable for the numerical modelling of the large scale processes. RANS equation after ensemble averaging is given by:

$$\frac{\partial U_i}{\partial t} + U_j \frac{\partial U_i}{\partial x_j} = -\frac{1}{\rho}\frac{\partial P}{\partial x_i} + \frac{\partial}{\partial x_j}\left[(\nu + \nu_t)\left(\frac{\partial U_i}{\partial x_j} + \frac{\partial U_j}{\partial x_i}\right)\right] + g_i \tag{2.19}$$

where U is the time averaged velocity, ρ is the density of the fluid, P is the pressure, ν is the kinematic viscosity, ν_t is the eddy viscosity and g the acceleration due to gravity.
The eddy viscosity, ν_t is calculated using $k-\omega$ model as explained below in next section. The present study uses the Wilcox's $k-\omega$ model (Wilcox, 1994) along with Reynolds Averaged Navier Stokes (RANS) equation. REEF3D also has provision for $k-\epsilon$ model (Launder and Sharma, 1974), EARSM (Wallin and Johansson, 2000), SST (Menter, 1993) and LES model.

- $k-\omega$ Model

  The $k-\omega$ model is a two-equation model based on the energy transport equations. One of the variables transported is the turbulent kinetic energy, k and the other is the turbulent dissipation, ω. Then the eddy viscosity, ν_t is calculated using the turbulent kinetic energy k and the turbulent dissipation ω (equation 2.16). The transport equations for k and ω are given as :

$$\frac{\partial k}{\partial t} + U_j \frac{\partial k}{\partial x_j} = \frac{\partial}{\partial x_j}\left[\left(\nu + \frac{\nu_t}{\sigma_k}\right)\frac{\partial k}{\partial x_j}\right] + P_k - \beta_k k\omega \tag{2.20}$$

$$\frac{\partial \omega}{\partial t} + U_j \frac{\partial \omega}{\partial x_j} = \frac{\partial}{\partial x_j}\left[\left(\nu + \frac{\nu_t}{\sigma_\omega}\right)\frac{\partial \omega}{\partial x_j}\right] + \frac{\omega}{k}\alpha P_k - \beta\omega^2 \tag{2.21}$$

$$\nu_t = min(\frac{k}{\omega}, \sqrt{\frac{2}{3}}\frac{k}{|S|}) \tag{2.22}$$

where, P_k is the production rate and the closure coefficients $\sigma_k = 2$, $\sigma_\omega = 2$, $\alpha = 5/9$, $\beta_k = 9/100$, $\beta = 3/40$. $|S|$ is the mean strain rate, which can be large in the case of oscillatory flow motion. The eddy viscosity ν_t is limited using equation 2.34 to avoid overproduction of turbulence in strained flow outside the boundary layer. Increased turbulent dissipation takes place in the vicinity of the free surface due to reduced turbulent length scales. Damping of the turbulent fluctuations also occurs normal to the surface leading to redistribution of intensity parallel to the interface. Due to a high value of $|S|$ near the air-water interface, standard RANS turbulence closure will give inaccurate results. Thus, additional turbulence damping is required. The specific turbulent dissipation at the free surface is given as:

$$\omega_s = \frac{c_\mu^{-\frac{1}{4}}}{\kappa} k^{\frac{1}{2}} \cdot \left(\frac{1}{y'} + \frac{1}{y^*}\right) \tag{2.23}$$

where, $c_\mu = 0.07$ and $\kappa = 0.4$. y' is the virtual origin of the turbulent length scale and has a value 0.07 times the water depth found empirically by Hossain and Rodi (1980). y^* is the distance from the nearest wall for a smooth transition to wall boundary value of ω. The specific turbulent dissipation is activated around the interface by multiplying it with the Dirac delta function $\delta(\phi)$:

$$\delta(\phi) = \begin{cases} \frac{1}{2\epsilon}\left(1 + \cos\left(\frac{\pi\phi}{\epsilon}\right)\right) & if \ \ |\phi| < \epsilon \\ 0 & else \end{cases} \tag{2.24}$$

2.8 Modelling of the Free Surface

In marine civil engineering, the cases involving ocean wave propagation are usually multiphase flows because they involve more than one phase, i.e., air and water. The free surface of water is modelled using a two-phase flow approach. There are various methods available as given below:

- Marker and Cell (MAC) Method: This approach is used to discretize functions for fluid flow with a free surface. It was developed by Harlow and Welch (1965). The MAC method is a finite difference solution technique for investigating the dynamics of an incompressible viscous fluid. It employs the primitive variables for the pressure and the velocity. It uses the Lagrangian virtual particles, whose coordinates are stored and which move from from a cell to the next according to the latest computed velocity field. The drawback of this method, is that for 3D problems, simulations become computationally too expensive.

- Volume of Fluids (VOF) Method: This method belongs is an Eulerian approach. It is characterised by a mesh stationary. It was published by Hirt and Nichols (1981). It is a scalar function, defined as the integral of a fluid's characteristic function in the control volume, namely the volume of a computational grid cell. The volume fraction of each fluid is tracked through every cell in the computational grid, while all fluids share a single set of momentum equations. With this method, the free-surface is not defined sharply, instead it is distributed over a the height of a cell. To avoid smearing of the free-surface, the transport equation have to be solved without excessive diffusion. Thus, the success of a VOF method depends heavily on the scheme used for the advection of the fraction function. Whereas a first order upwind scheme smears the interface, a downwind scheme of the same order will cause a false distribution problem which will cause erratic behaviour in cases, where the flow is not oriented along the grid lines. Another drawback of this scheme is that the free surface tends to get smeared over two to three cells due to the numerical diffusion and a local refinement is needed to represent the free surface accurately.

- Level Set Method (LSM): The level set method tracks the motion of an interface by embedding the interface as the zero level set of a signed distance function. The motion of the interface is matched with the zero level set. In this setting, curvatures and normals may be easily evaluated, topological changes occur in a natural manner, and the technique extends trivially to three dimensions. In the present study, the Level Set Method given by Osher and Sethian (1988b) is used to model the free surface. It is defined such that $\phi(\vec{x}, t) = 0$ at the interface. Away from the interface, the closest distance of the point from the interface defines its value and the sign represents the phase. The function can be written as:

$$\phi(\vec{x}, t) \begin{cases} > 0 & if\ \vec{x}\ is\ in\ phase\ 1 \\ = 0 & if\ \vec{x}\ is\ at\ the\ interface \\ < 0 & if\ \vec{x}\ is\ in\ phase\ 2 \end{cases} \tag{2.25}$$

  The movement of the level set function is given by an equation with a convective term.

$$\frac{\partial \phi}{\partial t} + \vec{u}\nabla\phi = 0 \tag{2.26}$$

  Numerical instability might rise because of a jump across the interface. Smoothening is carried out in that thickness of 2ϵ by a Heaviside function $H(\phi)$.

$$\begin{aligned} \rho(\phi) &= \rho_1 H(\phi) + \rho_2(1 - H(\phi)) \\ \nu(\phi) &= \nu_1 H(\phi) + \nu_2(1 - H(\phi)) \end{aligned} \tag{2.27}$$

where,

$$H(\phi) = \begin{cases} 0 & if\ \phi < -\epsilon \\ \frac{1}{2}\left(1 + \frac{\phi}{\epsilon} + \frac{1}{\pi} sin\left(\frac{\pi\phi}{\epsilon}\right)\right) & if\ |\phi| \leq \epsilon \\ 1 & if\ \phi > \epsilon \end{cases} \tag{2.28}$$

ρ_1 and ρ_2 represent the densities of the two fluids. Generally, the thickness of the smoothed out interface is taken as $\epsilon = 2.1$ on both sides of the interface. In the second step, simple averaging of the density at the two neighbouring cell centres is typically done to calculate the density at the cell faces (Croce et al., 2010). The two-step technique can lead to small scale oscillations of the free surface, while for other types of flows like open-channel flows this phenomenon is not observed. To overcome this drawback, a modified single step approach is used for computing density at the cell face with smoothed Heaviside function:

$$\rho_{i+\frac{1}{2}} = \rho_1 H\left(\phi_{i+\frac{1}{2}}\right) + \rho_2\left(1 - H\left(\phi_{i+\frac{1}{2}}\right)\right), \tag{2.29}$$

The level set function at the cell face is calculated through averaging:

$$\phi_{i+\frac{1}{2}} = \frac{1}{2}\left(\phi_i + \phi_{i+1}\right) \tag{2.30}$$

2.8.1 Reinitialization

As the simulation progresses, the interface moves and the signed distance property of level set function might not be maintained. In further time steps, it has to be updated without changing the zero level set location. This approach is called reintialization. This is done after every time step in the present study. Reinitialization can be done in two different ways: the partial differential equation (PDE) approach and the Fast Marching Method (FMM). The present study uses PDE approach. This approach is developed by Sussman et al. (1994).

$$\frac{\partial\phi}{\partial\tau} + S(\phi)\left(\left|\frac{\partial\phi}{\partial x_j}\right| - 1\right) = 0 \tag{2.31}$$

where S(ϕ) is the smooth signed function by Peng et al. (1999)

$$S(\phi) = \frac{\phi}{\sqrt{\phi^2 + \left|\frac{\partial\phi}{\partial x_j}\right|^2 (\Delta x)^2}} \tag{2.32}$$

Equation 2.43 is solved until the steady state is reached.

2.9 Immersed Boundary

The numerical model REEF3D uses a Cartesian grid in order to use higher order discretization schemes. But in the case of complex geometries, this approach is inflexible

and it cannot represent the complex geometries in a defined domain. To overcome this drawback, a ghost cell immersed boundary method (GCIBM) is used. (Berthelsen and Faltinsen, 2008). In this approach, the values for the fictitious ghost cells are computed across the boundary in the direction of the coordinate axis, as shown in Figure 2.2.

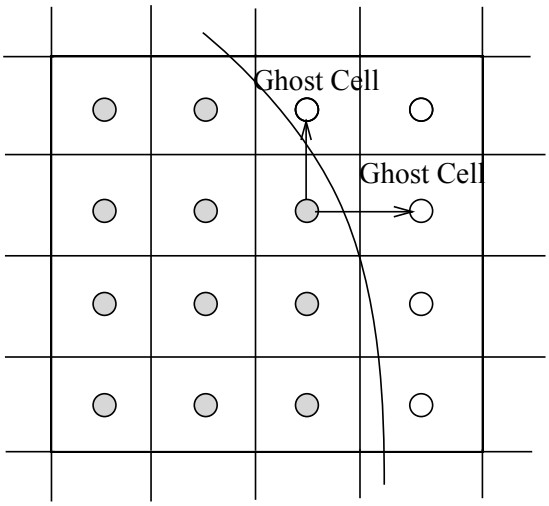

Figure 2.2: Ghost Cell Immersed Boundary

In this way, boundary conditions are enforced implicitly. The original local directional approach was a 2D application, but the present model employs an extended 3D approach. The local directional GCIBM is employed instead of the original GCIBM, because the original GCIBM can be a problem at sharp corners as given by Tseng and Ferziger (2003) and Mittal et al. (2008).

2.10 Parallelization

Parallelization means that computations are carried out using multiple processors simultaneously. The main benefit of parallelization is the faster execution of the numerical model. The easiest way to parallelize a code is to use a compiler that automatically detects the parallelism of the program and generates the parallel version employing open MP. There are several ways to parallelize a program this way containing input/output operations but one of the most important challenges is to parallelize loops because there the most CPU time is spent. In REEF3D, parallelization is done by decomposing the domain into smaller parts, which communicate with each other through ghost cells. This is easier to code as the numerical model already uses the ghost cell approach. The Message Passing Interface (MPI) is used for the exchange of value of ghost cell, as shown in the Figure 2.3. MPI is structured in a way that it can be used on both shared memory and distributed memory architectures.

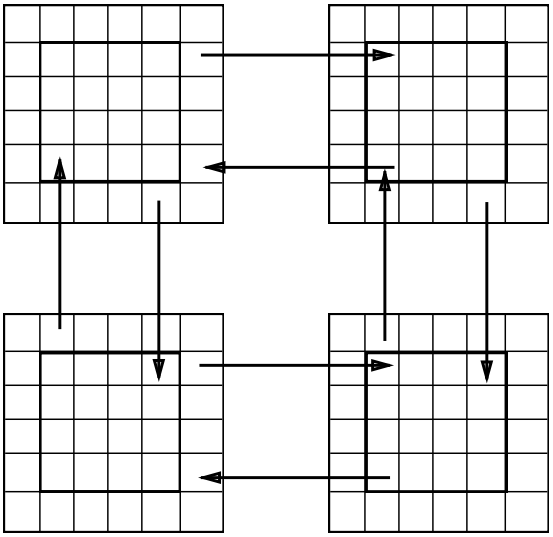

Figure 2.3: Exchange of data between inter-processor ghost points

Chapter 3

Numerical Wave Tank

For a CFD based study of the wave propagation and the hydrodynamics, a numerical wave tank is used to simulate the waves. Numerical wave tank in the CFD study has the same employability as the wave flume in the experiments. There has been a significant development in past few years in the application field of the numerical wave tank because of the increasing computational power of the computers. There are various methods available, some of them are:

- RANS with VOF approach: The CFD open-source software OpenFOAM uses this approach (Afshar, 2010). Spatial discretization is carried out using finite volume approach. The free surface is calculated with a Volume-of-Fluid approach based on convection of the fraction function and interface compression. The governing equations are solved on a collocated unstructured grid with a second-order accuracy for the spatial and temporal discretization. Later, a wave generation toolbox was developed for OpenFOAM with a new method for wave generation and absorption in the wave tank (Jacobsen et al., 2011).

- RANS with the LSM method: In the present study, the RANS equations in combination with the LSM is used. It uses domain discretization method for implementation of wave tank and level set method for capturing the free surface. High-order temporal and spatial discretization can be used for the level set function, which avoid unphysical damping of the propagating water waves. Staggered grid is used to solve the governing equations in order to ensure a tight velcoity-pressure coupling. Kamath (2012) and Afzal (2013) have used this approach before.

- Combination of the Potential Theory and RANS: The combination of both the methods is a possible research area as reported by Clauss et al. (2005). It has been reported that the use of potential theory with the method of finite elements results in a fast and accurate solution, though RANS equations are preferred for the simulation of wave-structure interactions.

3.1 Relaxation Method

Typical inlet boundaries for free surface flows are of Dirichlet type, but because of a moving free surface and changing flow directions, Dirichlet type wave generation does not give good numerical waves. Thus, the relaxation method is used as the wave generation and the dissipation boundary in the wave (Larsen and Dancy, 1983). Relaxation Zone is used for the wave generation with the typical size of one wavelength. The values for the velocities and the free surface are ramped up from the computational values obtained from wave theory (Eq. 3.1). The generated waves are free from any disturbances occurring at the interfaces. Also, the reflected waves which travel back towards the inlet are absorbed with this method. A numerical beach is needed at the end of a wave flume in order to dissipate waves and avoid reflections. In the relaxation method, a gradual shift is made from the analytical to the computational solution.

$$\begin{aligned} u(\widetilde{x})_{relaxed} &= \Gamma(\widetilde{x})u_{analytical} + (1-\Gamma(\widetilde{x}))u_{computational} \\ w(\widetilde{x})_{relaxed} &= \Gamma(\widetilde{x})w_{analytical} + (1-\Gamma(\widetilde{x}))w_{computational} \\ p(\widetilde{x})_{relaxed} &= \Gamma(\widetilde{x})p_{analytical} + (1-\Gamma(\widetilde{x}))p_{computational} \\ \phi(\widetilde{x})_{relaxed} &= \Gamma(\widetilde{x})\phi_{analytical} + (1-\Gamma(\widetilde{x}))\phi_{computational} \end{aligned} \tag{3.1}$$

This way, the function $\Gamma(\widetilde{x})$ changes gradually depending on the zone and thus transforming the values from the analytical to the computational ones. The initially computational values of the velocity and the free surface are transitioned from the analytical values, calculated from the linear wave theory. In the beach zone, the transformation of the values again takes place from the computational to the analytical values such that they become zero at the beach.

A rule of thumb as mentioned by Engsig-Karup (2006) is to extend the relaxation zone over 1-2 times the wavelength of the wave being simulated. The present study uses the relaxation functions being given by Jacobsen et al. (2012) for the wave generation and the absorption, given by:

$$\Gamma(\widetilde{x}) = 1 - \frac{e^{(\widetilde{x}^{3.5})} - 1}{e - 1} \; for \; \widetilde{x} \in [0; 1] \tag{3.2}$$

$\widetilde{x}$ is scaled to the length of the relaxation zone. In this method, the numerical wave tank consists of two relaxation zones: at the inlet and the outlet, as shown in the Figure 3.1. The Figure 3.1 also illustrates the shapes of the relaxation functions in their respective zones. The wave generation zone for this study has the length of one wavelength, the numerical beach extends over two wavelengths.

3.2 Wave Theories

Water waves are caused by the external forcing such as the wind, the gravity, the cyclone etc. The other field parameters like the water depth, the bottom slope also plays

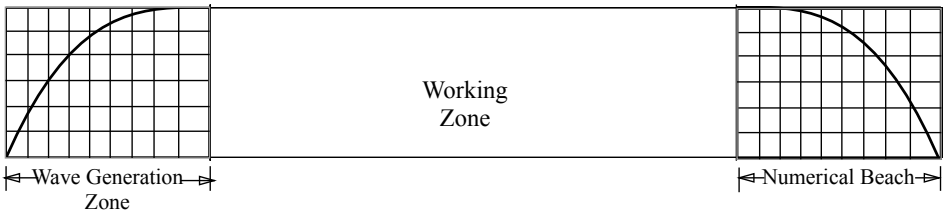

Figure 3.1: Shapes of Relaxation Functions in different zones of NWT

a key role in the formation of the waves. Wind waves in the ocean are called ocean surface waves. Wind waves have a certain amount of randomness: subsequent waves differ in the height, the duration, and the shape with a limited predictability. They can be described as a stochastic process, in combination with the physics governing their generation, growth, propagation and decay, as well as governing the interdependence between the flow quantities such as: the water surface movements, the flow velocities and the water pressure. There are various theories available explaining the waves and their propagation.

3.2.1 Linear Wave Theory

Linear wave theory considers the two fundamental equations, the mass and the momentum balance equations. The linear wave theory gives a linearised description of the propagation of gravity waves. The application of the linear wave theory is rather limited due to the small amplitude assumption made in the governing equations. Other assumptions are inviscid, incompressible and irrotational flow. The linear wave theory simplifies the kinematic and the dynamic boundary conditions with the approximations respectively as shown in equation 2.51 and equation 2.52, given as (Arntsen and Krogstad, 2000):

$$\frac{\partial \eta(x,t)}{\partial t} = w(x,0,t) \tag{3.3}$$

$$\frac{\partial \Phi(x,0,t)}{\partial t} + g\eta(x,t) = 0 \tag{3.4}$$

The linear wave theory defines, level set function, ϕ, the horizontal and vertical particle velocities, u and w, respectively given as:

$$\begin{aligned} u(x,z,t)_{analytical} &= \frac{\pi H}{T}\frac{cosh\left[k\left(z+d\right)\right]}{sinh\left(kd\right)}cos\theta \\ w(x,z,t)_{analytical} &= \frac{\pi H}{T}\frac{sinh\left[k\left(z+d\right)\right]}{sinh\left(kd\right)}sin\theta \\ \phi(x,z,t)_{analytical} &= \frac{H}{2}cos\theta - z + d \end{aligned} \tag{3.5}$$

The wave number k and the wave phase θ are defined as follows:

$$\begin{aligned} k &= \frac{2\pi}{L} \\ \theta &= kx - \omega t \end{aligned} \tag{3.6}$$

where, H is the wave height, L the wavelength, T the wave period, ω the angular wave frequency and z the vertical coordinate with the origin at the still water level. In the numerical model, the pressure is not prescribed in the wave generation zone, so as not to over-define the boundary conditions. At the numerical beach, the pressure is always set to the hydrostatic values based on the water depth d, independent of the wave input.

3.3 Irregular Waves

The study of irregular waves is of great practical interest, because of the waves found in the nature. Regular waves are seldomly found in the field. Irregular waves can be viewed as the superposition of a number of regular waves (wave components) with the different frequencies and the amplitudes. Irregular waves can be of two types: long-crested and short-crested. In long-crested waves, all the wave components are in the same direction, they are also called uni-directional irregular waves. In short-crested waves, the wave components are often multi-directional.

Analysis of the irregular waves is different from regular waves, as in an irregular wave train, the wave heights and the wave periods are not uniform. In spite of the random character, the short-term variations can be described in a statistical way by taking the average parameters. It is seen that statistics can be considered stationary in time. In order for the averages to be representative of the given sea state, the record should be short enough to be statistically stationary, while at the same time. the record should be long enough to get the reliable averages. In practice, one recording is done for instance 20 minutes every three hours, then this record is representative for the entire time period of the three hours. There are two ways to characterize a wave record in terms of its short term statistics:

- Based on direct analysis of the time series and considering it as a sequence of individual waves, each with their own wave height and wave period, also called wave-by-wave analysis.
- Through a spectral analysis using the fact that the free surface can be seen as a summation of an infinite number of linear waves with different hydrodynamic parameters like the wave height, the time period, the direction etc.

3.3.1 Direct analysis of the irregular waves

The mean and the standard deviation are important statistical parameters that can be derived from the time series. For a wave-by-wave analysis the mean water level should be subtracted from the record so as to have a purely oscillatory signal about the mean. When the signal is demeaned, individual wave can be defined as waves with wave heights equal to the difference in elevation between the crest and the trough. The wave length and the wave period are the distance and the period respectively, between two subsequent downward or upward zero-crossings.
The significant wave height is denoted as H_s or $H_{1/3}$. The significant wave height is defined as the average height of the highest one third of the waves.

$$H_{1/3} = \frac{1}{N/3} \sum_{j=1}^{N/3} H_j \tag{3.7}$$

where, H_j is the wave height of j-th wave and N is the total number of waves
It is called significant wave height because it approximately corresponds to the visual estimates of observers at sea of a representative wave height. Another used parameter is the root mean square wave height, which is obtained by taking the square root of the mean of the wave heights squared:

$$H_{rms} = \sqrt{\frac{1}{N} \sum_{i=1}^{N} H_i^2} \tag{3.8}$$

It can also be related to the wave energy, as the wave energy is related to the wave height squared. The mean of all the wave periods is called the mean-wave period or zero-crossing wave period. It is given as:

$$T_0 = \frac{1}{N} \sum_{i=1}^{N} T_i \tag{3.9}$$

Similar to the significant wave height, the significant wave period is defined as the average wave period of the highest one-third of the waves. However, it has less physical relevance because it is not related to visual estimates. It is given as:

$$T_{1/3} = \frac{1}{N/3} \sum_{j=1}^{N/3} T_j \tag{3.10}$$

3.3.2 Spectral analysis of the irregular waves

Spectral analysis is an alternative way of the statistical representation of the sea state, it uses the fact that the surface elevation at a location can be unravelled into the various sine waves with different frequencies. Fourier analysis can be carried out

to determine the amplitude and phases (Tucker and Pitt, 2001). From the amplitudes of the various components, the spectrum of the wave energy can be calculated. It can be easily seen that for one harmonic component the variance is equal to $a_n^2/2$. Then, for the sum of the harmonic components, the variance is given by:

$$\sigma^2 = \sum_{n=1}^{N} a_n^2/2 \tag{3.11}$$

The variance density spectrum gives the variance density per unit frequency interval for each frequency and is constant for Δf converges to zero:

$$\lim_{\Delta f \to 0} \frac{a_n^2/2}{\Delta f} = E(f_n) \tag{3.12}$$

The integral of the spectrum gives the total variance:

$$\int_0^\infty E(f)df = \bar{\eta}^2 = \sigma^2 \tag{3.13}$$

Thus, in the spectrum the variance density is the contribution of one component of the total variance. The standard deviation, σ can be estimated from the area under the spectrum. An important parameter defined in the spectral analysis is the peak wave period, T_p which corresponds to the $E(f)_{max}$.

The narrower the spectrum, the more regular the waves are. This means that spectrum has a short range of frequencies, while a broader spectrum indicates more irregularity and a wider range of frequencies. Other characteristic parameters can be expressed in terms of spectral moments:

$$m_n = \int_0^\infty f^n E(f)df \text{ for n = ...,-3,-2,-1,0,1,2,3....} \tag{3.14}$$

m_0 gives the area under the spectrum as evident from the above equation. Thus, standard deviation,σ can be written as:

$$\sigma = \sqrt{m_0} \tag{3.15}$$

The zero-crossing period can be determined from the spectral moments and is given by:

$$T_2 = \sqrt{\frac{m_0}{m_2}} \tag{3.16}$$

3.3.3 Rayleigh Distribution

The Rayleigh distribution relates the parameters determined by the wave-by-wave analysis and the spectral analysis. As, the surface elevation can be considered as

the sum of a large number of components with the random phases, a short term distribution of the wave heights also known as the Rayleigh distribution is defined:

$$p(H) = \frac{H}{4\sigma^2} e^{\frac{H}{8\sigma^2}} \tag{3.17}$$

where, $p(H)$ is the probability density function. It can be seen from the above equation, the probability that an individual wave height H' exceeds a specified wave height, H is given as:

$$p(H' > H) = 1 - p(H' < H) = 1 - \int_0^H P(H) dH = e^{\frac{H}{8\sigma^2}} \tag{3.18}$$

Using the Rayleigh distribution, the significant wave height H_s is given as:

$$H_s = 4\sigma \tag{3.19}$$

The probability of exceedance of the wave heights according to the Rayleigh distribution can be written as:

$$p(H' > H) = e^{-2(\frac{H}{H_s})^2} \tag{3.20}$$

So, it can be stated that the short-term distribution of the wave heights in irregular waves exhibit some characteristic relations which can be used for their analysis and the data processing.

3.4 Irregular Wave Generation

In the numerical model REEF3D, irregular waves are generated using the fundamentals of irregular waves as mentioned in the previous section. First-order irregular waves are obtained by the simple super-positioning of the linear regular waves components. The free surface, η is defined as:

$$\eta = \sum_{i=1}^{N} A_i cos\theta_i \tag{3.21}$$

where, the amplitude of the each component,

$$A_i = \sqrt{2 S_{pm,i} \Delta\omega_i} \tag{3.22}$$

where S_i is the spectral density and θ_i is the phase of the each component

$$\theta_i = k_i x - \omega_i t + \epsilon \tag{3.23}$$

where ϵ is a random number between 0 and 2π and k_i is the wave number of a component given by:

$$k_i = \frac{2\pi}{\lambda_i} \tag{3.24}$$

where λ_i is the wavelength of a component.
Similarly, the horizontal velocity u and the vertical velocity w are defined as the sum of the values for these parameters for the individual components in the irregular wave train.

$$u = \sum_{i=1}^{N} A_i \omega_i \frac{cosh(k_i(z+d))}{sinh(kd)} cos\theta_i \tag{3.25}$$

$$w = \sum_{i=1}^{N} A_i \omega_i \frac{sinh(k_i(z+d))}{sinh(kd)} sin\theta_i \tag{3.26}$$

There are different kinds of spectra available in the literature for the analysis of irregular waves. REEF3D employs the two most widely used spectra, the Pierson-Moskowitz (PM) spectrum and the JONSWAP spectrum. The Pierson-Moskowitz (PM) spectrum is used to describe the fully developed sea state for the irregular waves. This spectrum is defined for the unidirectional seas in the North Atlantic Ocean for fully developed local wind with an unlimited fetch, while the JONSWAP spectrum is used to describe a partially developed sea state. The measured spectrum in the sea can be approximated by the various semi-empirical forms, which correspond to the locally generated waves, and the swell waves can be included as an additional contribution to the low frequencies. The required significant wave height H_s, the peak angular frequency ω_p and the number of components N are given as input values to the PM spectrum. The spectral density for each component is calculated as:

$$S_{pm,i}(\omega) = \frac{5}{16} * H_s^2 * \omega_p^4 * \omega_i^{-5} * exp((\frac{-5}{4}) * (\frac{\omega_i}{\omega_p})^{-4}) \tag{3.27}$$

where ω_p is the peak frequency of the spectrum and w_i covers the range of frequencies in the spectrum.

The JONSWAP spectrum is given as:

$$S_{js,i}(\omega) = \frac{5}{16} * H_s^2 * \omega_p^4 * \omega_i^{-5} * exp((\frac{-5}{4}) * (\frac{\omega_i}{\omega_p})^{-4}) * exp(\frac{-(\omega-\omega_p)^2}{2 * \sigma^2 * {\omega_p}^2}) \tag{3.28}$$

The frequency spectrum, $S_{pm}(\omega)$ and $S_{js}(\omega)$ gives the distribution of the wave energy as a function of angular frequency ω.
$\sigma = 0.07$, when $\omega < \omega_p$
$\sigma = 0.09$, when $\omega > \omega_p$
The frequency interval, dw is given as:

$$dw = \frac{w_s - w_e}{N} \tag{3.29}$$

where, w_s and w_e are the lower and the upper limits of the angular frequency range.

3.5 Conversion of free surface elevation to spectrum

All the data obtained in the ocean with the help of wave buoys, experimental data and even the numerical model give a measure of wave heights with a given time series. For the spectral analysis of the obtained irregular waves time series, this data is first converted into a spectrum. This is done by using the Fourier Transformation. There are various kinds of Fourier Transformations available in literature (Tucker and Pitt, 2001)

- Finite Fourier Transformation refers to the Fourier transformation of a continuous finite length of the record.
- Infinite Fourier Transformation deals with the integration notionally taken from $-\infty$ to ∞, but it is relevant with cases of a limited duration like transients.
- Discrete Fourier Transformation (DFT) is the finite Fourier transformation adapted for the use of discretely sampled data, and is used to analyse the wave data.
- Fast Fourier Transformation (FFT) is an algorithm for carrying out DFT. The present study utilises the FFT for the analysis.
- Direct Fourier Transformation is used to specify that the Fourier transformation is performed via time series, unlike Fourier transforming the autocorrelation function, which used to be the standard procedure until FFT was invented.

3.5.1 Fast Fourier Transformation

The Fourier theorem states that a continuous variable, $\tau(t)$ measured over a finite duration T, then in interval $t = -T/2$ to $T/2$, it may be represented as the sum of number of the sinusoidal components, each with an integral number of waves in the time T:

$$\tau(t) = \frac{a_0}{2} + \sum_{n=1}^{\infty}(a_n cos(2\pi nt/T) + (b_n sin(2\pi nt/T)) \tag{3.30}$$

where, n is an integer. In its digital form, it can be thought of transforming a set of M numbers into another set of M numbers which carry the identical information. The Fourier theorem further states that:

$$a_n = \frac{2}{T}\int_{-T/2}^{T/2} \tau(t) cos(2\pi nt/T) dt \tag{3.31}$$

$$b_n = \frac{2}{T}\int_{-T/2}^{T/2} \tau(t) sin(2\pi nt/T) dt \tag{3.32}$$

The set of values of a_n and b_n is referred as the Fourier transform of $\tau(t)$. The standard procedures involves the calculation of all a_n and b_n for a wave record using the above equations. If the variable $\tau(t)$ is sampled at regular intervals Δt, then the value of n in the above equations becomes $\frac{T}{\Delta t}$. The values of a_n and b_n obtained are generally different from those, when computed by the transformation of a continuous variable. But, the difference is insignificant, if any components of $\tau(t)$ with the frequencies above $\frac{1}{2\Delta t}$, also called Nyquist frequency have negligible amplitudes.

In terms of complex number, $\tau(t)$ can be written as:

$$\tau(t) = \sum_{-\infty}^{\infty} A_n e^{i\omega_n t} \tag{3.33}$$

where,

$$\omega_n = \frac{2\pi n t}{T} \tag{3.34}$$

and,

$$A_0 = \frac{1}{2a_0} \tag{3.35}$$

$$A_n = \frac{1}{2}(a_n - ib_n) \tag{3.36}$$

$$A_{-n} = \frac{1}{2}(a_n + ib_n) \tag{3.37}$$

A_{-n} is also represented as the complex conjugate A_n^* of A_n. Here, the amplitude of the nth complex component is $|A_n|$, while the amplitude of the nth real component is $\sqrt{a_n^2 + b_n^2} = 2|A_n| = 2\sqrt{A_n A_n^*}$. The spectral density $S(f)$ is obtained by summing the variances of all the Fourier components within the chosen spectral resolution, Δf :

$$S(f)\Delta f = 2\sum_{\Delta f} A_n A_n^* \tag{3.38}$$

where, the sum is taken over the components in the frequency interval Δf with n positive only.

Sea actually consists of a continuous spectrum of the waves. Thus, for the component wavelength, whose frequency is not exactly the same as harmonic of T, most of the energy goes to the nearest harmonics, but a proportion also goes to more distant ones. This leaked energy can be significant in some cases. For example, to analyse the records in 400 s sub-sections, the leakage is often serious, thus windowing is required to avoid the leakage. When data is analysed in the lengths of 1000s or more, the leakage is usually insignificant. The present study uses a Matlab code to carry out the FFT for the spectra analysis. A Matlab predefined function *pwelch* is used for the FFT of the free surface elevation data to spectrum. The value of the windowing is defined in each case depending on the length of the data.

Chapter 4

Validation for irregular waves in the numerical wave tank

In this chapter, the numerical model is tested and validated for the generation and the propagation of irregular waves. Then, the case of irregular wave propagation over a bar is simulated. The numerical results are compared to the experimental data.

4.1 Setup of the Numerical Wave Tank

Simulations are carried out in a 2D numerical wave tank, 42 m long and 1 m high with a water depth d of 0.5 m and a significant wave height, $H_s = 0.02$ m. The length of the wave generation zone is 5 m and length of the numerical beach is 10 m. Wave gauges are placed in the numerical wave tank for measuring the free surface elevations at $x = 5$ m, 10 m, 15 m, 20 m and 25 m, respectively. The simulations are run for the different grid sizes, the different peak wave periods, a different number of wave components and the different lengths of simulation time to validate the numerical model. This is done to test the numerical accuracy and convergence of the model. The empty wave tank can be seen in the Figure 4.1

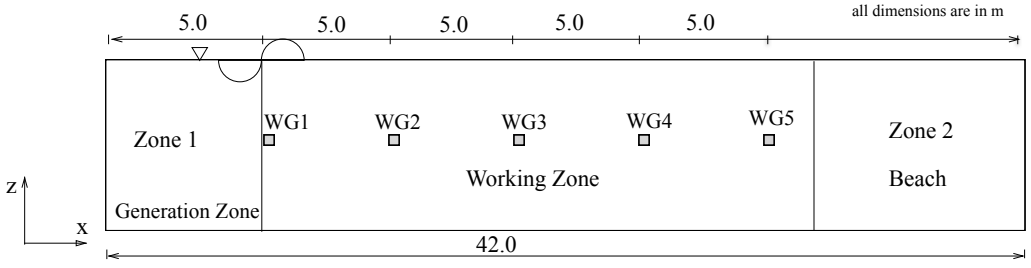

Figure 4.1: Setup of the Numerical Wave Tank

4.1.1 Study with the different grid sizes

Simulations are carried out with grid sizes of $dx = 0.05$ m, 0.025 m and 0.01 m to study the effect of the grid size on the generated wave spectrum at different locations in the wave tank. The wave parameters chosen are: significant wave height H_s=0.02 m, peak time period T_p =1.18 s, the number of waves $N = 25$. The numerical parameter, the length of the simulation t is chosen to be 500 s. The numerical results from REEF3D are compared with the theoretical PM spectrum. The Figure 4.2 shows the results with a grid size, $dx = 0.05$ m. It illustrates that the numerical results for the wave gauge at $x = 5$ m, match reasonably well with the theory. But, the numerical results do not show a good agreement with the theoretical wave spectrum for the wave gauges located at the farther locations int the NWT. For the wave gauges located at $x =$ 15 m, 20 m and 25 m, the generated wave spectrum has more energy in the higher frequency range, the possible reason is the numerical damping. The reason is that the wave gauge at $x = 5$ m shows the incident spectrum and is located in the wave generation zone, so the waves generated at this location have not yet propagated.

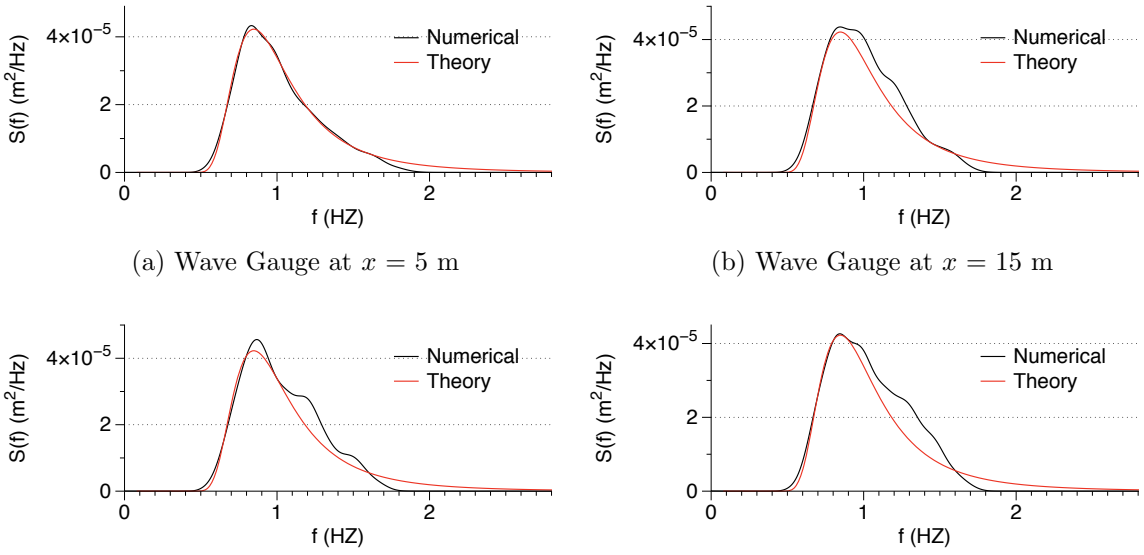

(a) Wave Gauge at $x = 5$ m

(b) Wave Gauge at $x = 15$ m

(c) Wave Gauge at $x = 20$ m

(d) Wave Gauge at $x = 25$ m

Figure 4.2: $T_p = 1.18$ s, $N = 25$, $H_s = 0.02$ m, $dx = 0.05$ m

The wavelength corresponding to the peak frequency, $f_p = 0.85$ Hz is 1.99 m for all the wave gauge locations because the location of the peak of spectrum is not affected by the wave gauge location. However, the value of the peak slightly changes for every wave gauge location. The frequency range on both sides of the f_p corresponding to $S_p/3$ is 0.55 Hz to 1.28 Hz for the wave gauge at location, $x = 5$ m. This frequency range becomes 0.55 Hz to 1.31 Hz for the wave gauge at location, $x = 15$ m. For, the the wave gauge at location, $x = 20$ m , the value of the S_p is also higher, thus frequency range corresponding to $S_p/3$ is 0.58 Hz to 1.38 Hz. And, at the wave gauge

at x= 25 m, the frequency range is 0.55 Hz to 1.38 Hz. This clearly shows that spectrum gets wider as the wave propagates through the NWT. The match between the numerical and the theoretical spectrum in the wave generation zone, at $x = 5$ m proves that the numerical model generates irregular waves of a good quality even for the coarser grids. The number of the cells available per wave length is 40 in this case.

The Figure 4.3 shows the results for the grid size, $dx = 0.025$ m. A good agreement between the numerical and the theoretical results for the incident wave spectrum at the wave gauge located at $x = 5$ m shows a good wave generation by the numerical model. As, the wave propagates, it is clearly seen that more wave energy is distributed to the higher frequency range = 1.2 Hz to 2.3 Hz as compared to the theoretical spectrum. The frequency range corresponding to $S_p/3$ is 0.55 Hz to 1.38 Hz for the wave gauge at location, $x = 15$ m. The value of the peak is also slightly higher than the theoretical value for this wave gauge location. For the wave gauges located at $x =$ 20 m and $x = 25$ m, the frequency range is 0.55 Hz to 1.37 Hz and 0.55 Hz to 1.42 Hz respectively. The values of the frequency range corresponding to $S_p/3$ clearly show that the spectrum gets wider as the wave propagates. However, the match between both the spectra is not acceptable for the farther locations of the wave gauges in the NWT. The number of cells available per wave length is 80 in this case.

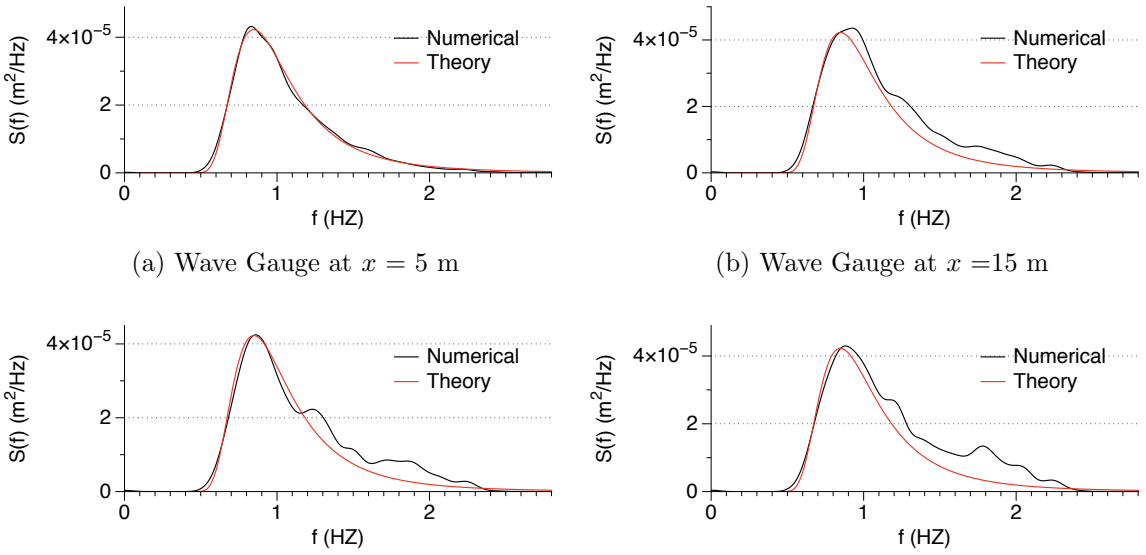

(a) Wave Gauge at $x = 5$ m

(b) Wave Gauge at x =15 m

(c) Wave Gauge at $x = 20$ m

(d) Wave Gauge at $x = 25$ m

Figure 4.3: T_p=1.18 s, $N = 25$, H_s =0.02 m, $dx = 0.025$ m

The Figure 4.4 shows the results for the fine grid, dx =0.01. The numerical results match well with the theoretical spectra for all the wave gauges. The numerical results give a high quality spectrum for the wave gauges located in the working zone of the numerical tank. The frequency range corresponding to $S_p/3$ is 0.55 Hz to 1.28 Hz for the incident wave gauge at location, $x = 5$ m and at location, $x = 15$ m . The value of

the peak is maintained and is agreeable with the theoretical spectrum. For the wave gauges located at $x = 20$ m and $x = 25$ m, the frequency range is the same = 0.55 Hz to 1.28 Hz. The values of the frequency range corresponding to $S_p/3$ for the wave gauges located at the farther locations in the NWT is very close to the wave gauges located in the vicinity of the wave generation zone. It is clearly observed that the numerical results show a good agreement with the theoretical spectrum. The number of cells available per wavelength in this case is 199.

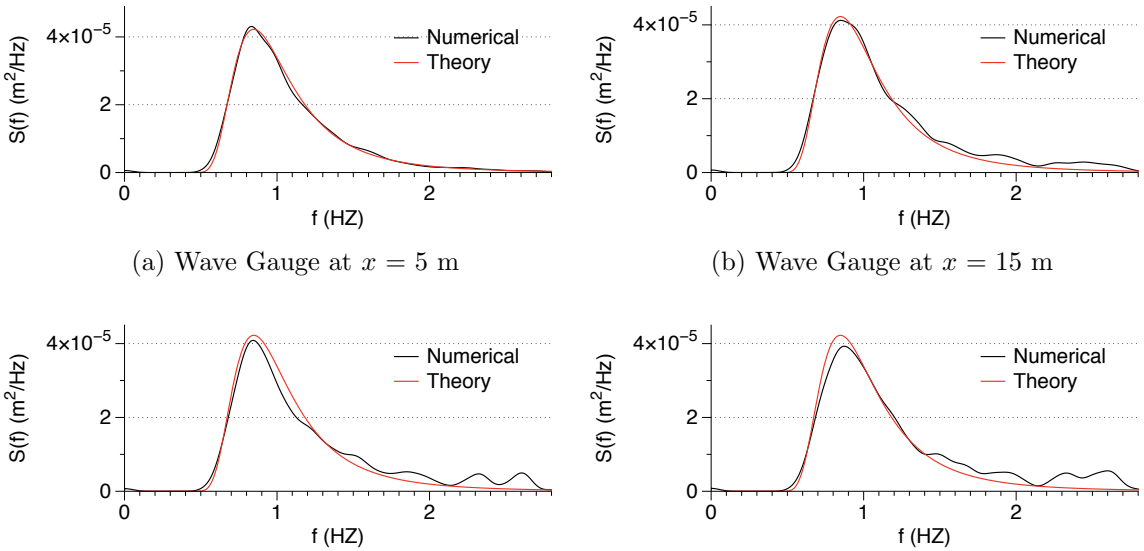

(a) Wave Gauge at $x = 5$ m

(b) Wave Gauge at $x = 15$ m

(c) Wave Gauge at $x = 20$m

(d) Wave Gauge at $x = 25$ m

Figure 4.4: $T_p = 1.18$ s, $N = 25$, H_s= 0.02 m, $dx = 0.01$ m

The Figures shown above depict that for the coarse grid results, at $dx = 0.05$ m and 0.025 m, as the wave propagates, the numerical spectrum deviates from the theoretical spectrum. This deviation increases, in a way that it is least for the wave gauge located in the wave generation zone and maximum for the wave gauge located at the end of the working zone of the numerical wave tank. However, it should be noted that the peak of the spectrum is still maintained in each of the case. For the fine grid case, the sufficient number of grid points per wavelength are available to give the good results for all the wave gauge locations. Thus, a grid size $dx = 0.01$ m is chosen for the further calculations.

4.1.2 Effect of number of waves

In this subsection of the chapter, the effect of number of waves, N on the irregular wave generation is tested. Other parameters such as the grid size $dx = 0.01$ m, the significant wave height $H_s = 0.02$ m, the peak time period $T_p = 1.18$ s, the length of simulation time = 500 s are kept constant. Simulations are carried out by varying

the number of linear wave components $N = 25$ and 100 as shown in the Figures 4.5 and 4.6 respectively.

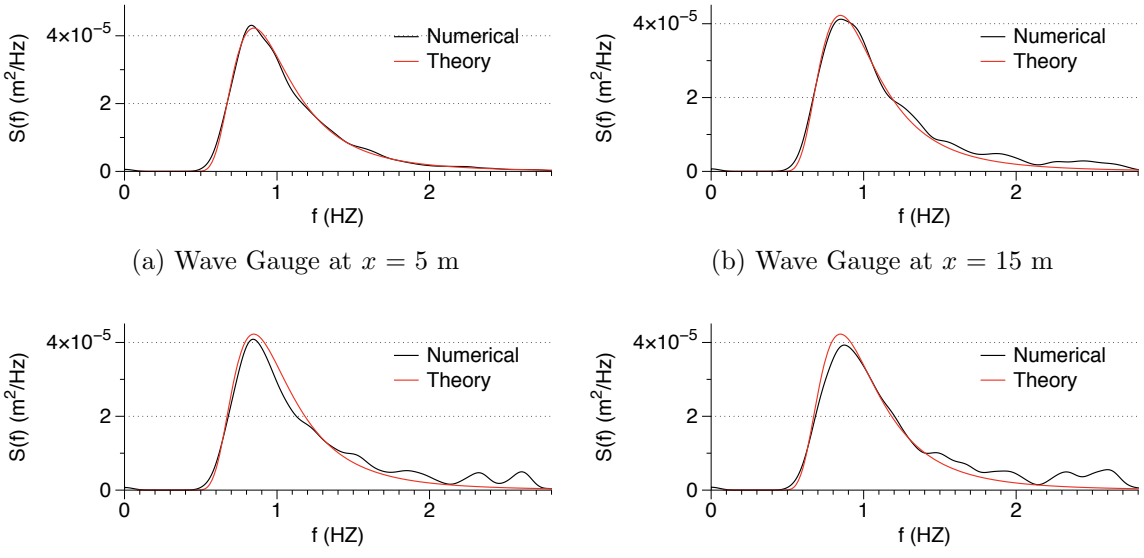

(a) Wave Gauge at $x = 5$ m

(b) Wave Gauge at $x = 15$ m

(c) Wave Gauge at $x = 20$ m

(d) Wave Gauge at $x = 25$ m

Figure 4.5: $T_p = 1.18$ s, $dx = 0.01$ m, $H_s = 0.02$ m, $N = 25$

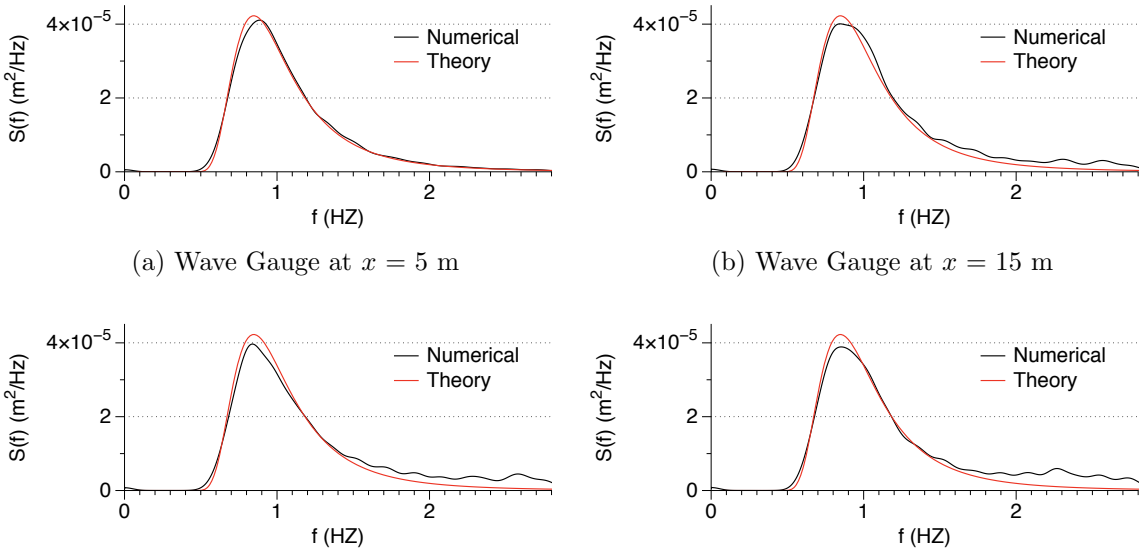

(a) Wave Gauge at $x = 5$ m

(b) Wave Gauge at $x = 15$ m

(c) Wave Gauge at $x = 20$ m

(d) Wave Gauge at $x = 25$ m

Figure 4.6: $T_p = 1.18$ s, $dx = 0.01$ m, $H_s = 0.02$ m, $N = 100$

As mentioned before, the irregular waves are generated as a superimposition of linear wave components, thus the generated waves are short-crested. The Figure 4.5 for N

= 25, shows a reasonable agreement with a slight amount of the spurious energy in the higher frequency range, from 1.5 Hz to 2.5 Hz. The Figure 4.6 for $N = 100$ shows that a slight amount of spurious energy in the higher frequency range is still present, though a bit lesser than for $N = 25$. Thus, it can be inferred that on increasing the number of wave components, the generated spectra shows a better agreement with the theoretical spectrum but the improvement in the numerical results is not significant. It is also noted that the energy contained in the spectrum for both the cases is same, and the peak of the spectrum is about the same. Thus, it can be concluded that the number of wave components N does not play a significant role in the simulations.

4.1.3 Generation of different peak periods

In this section, the numerical model is tested for different values of the peak wave period. Other parameters such as grid size $dx = 0.01$ m, significant wave height $H_s = 0.02$ m, number of waves $N= 25$, length of the simulation time = 500 s are kept constant. The simulations are run for peak periods $T_p = 2.50$ s, 2.00 s, 1.18 s and 0.80 s. The free surface elevation for the wave generation zone with the time series for the wave gauge at $x = 5$ m for $T_p = 2.50$ s, 2.00 s, 1.18 s and 0.80 s is seen in the Figure 4.7.

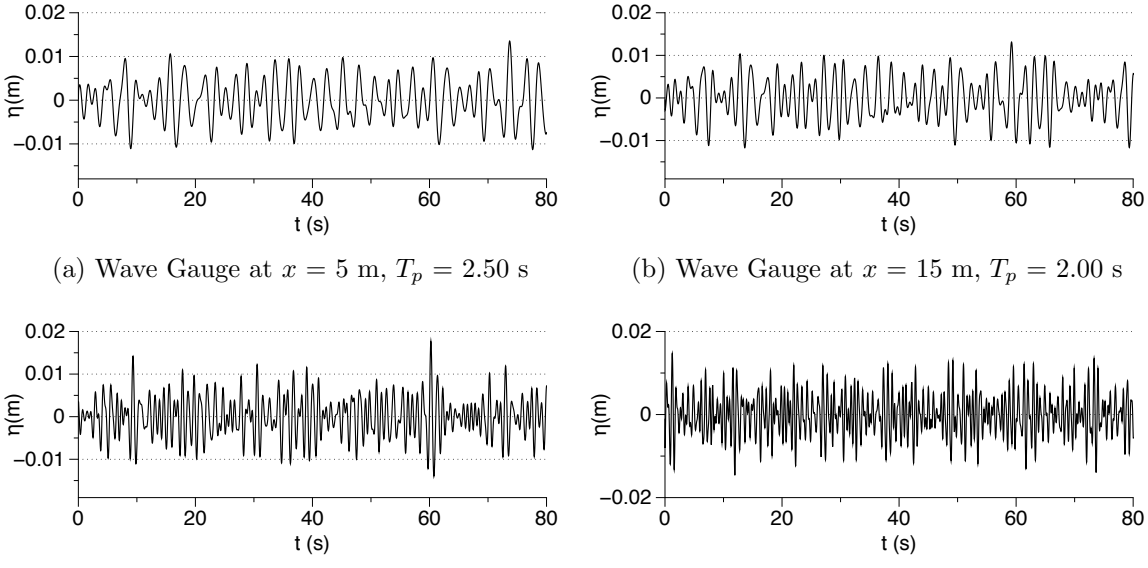

(a) Wave Gauge at $x = 5$ m, $T_p = 2.50$ s

(b) Wave Gauge at $x = 15$ m, $T_p = 2.00$ s

(c) Wave Gauge at $x = 20$ m, $T_p = 1.18$ s

(d) Wave Gauge at $x = 25$ m, $T_p = 0.80$ s

Figure 4.7: $dx = 0.01$ m, $H_s = 0.02$ m, $N = 25$

It is observed from the Figure 4.7 that the spreading of waves becomes less as T_p decreases. This is proven by the fact that as expected for a higher value of the peak wave period, the surface elevation is dominated by the longer waves, while for a lower value of the peak period, the surface elevation is dominated by the shorter waves.

When the value of T_p decreases, more irregularity and peaks are also observed. The Figures 4.8, 4.9 and 4.10 show the spectrum for the different peak periods. It is observed from the Figures that the results with a higher peak period have a relatively narrower spectrum and the peak also has a higher value. As the peak wave period becomes lower, the spectrum becomes broader and the value of the peak becomes less. This may be attributed to the fact that the total energy, which is given by the area under the curve, remains same.
It is also seen that for the higher peak periods, T_p = 2.50 s, 2.00 s and 1.18 s, the numerical results are in a good agreement with the theoretical results. However, the numerical results do not show a good agreement with the theoretical spectrum in Figure 4.11 for T_p = 0.80 s. The numerical results show multiple peaks and do not form the shape of spectrum as per shown by the theoretical spectrum. This is because the waves are relatively short in this case and they need a higher grid resolution for a good representation. This means that for the case with T_p = 0.80 s, the number of grid points available per wave length are not sufficient. It can also be observed from the Figures that the numerical results for the higher peak wave periods do not differ significantly. Further testing is continued with a peak wave period T_p =1.18 s.

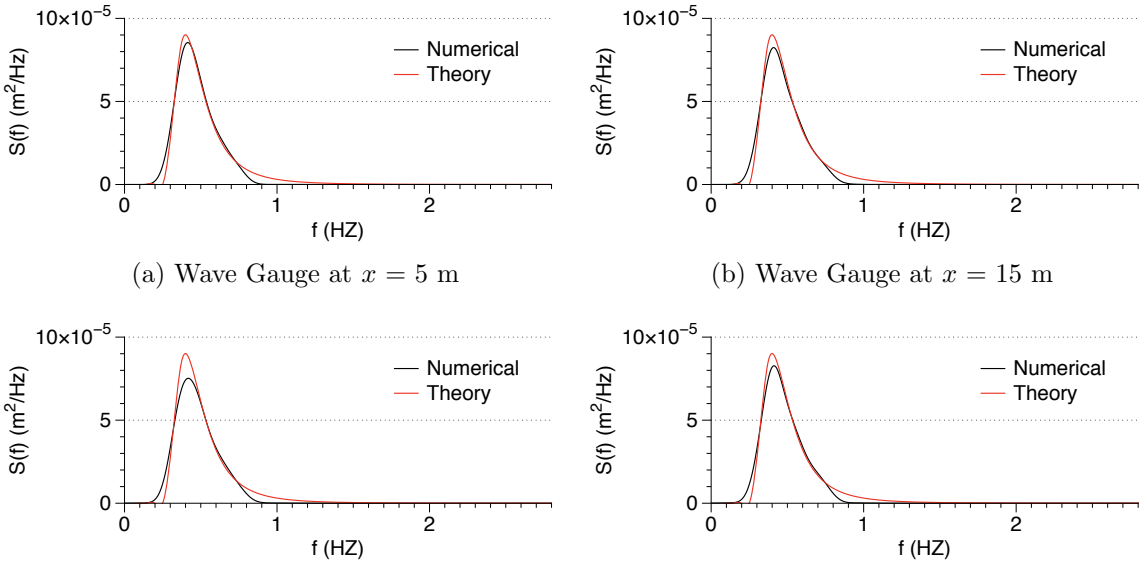

(a) Wave Gauge at x = 5 m

(b) Wave Gauge at x = 15 m

(c) Wave Gauge at x = 20 m

(d) Wave Gauge at x = 25 m

Figure 4.8: N = 25, dx = 0.01 m, H_s = 0.02 m, T_p = 2.5 s

Figures 4.12 and 4.13 show a scaled up free surface elevation with horizontal velocity contours for generated irregular waves of T_p = 2.5 s and T_p = 1.18 s. It is seen from Figure 4.12 that the longer waves dominate the free surface elevation for a higher value of T_p = 2.5 s, whereas Figure 4.13 for a lower value of T_p = 1.18 s shows that the free surface elevation is dominated by shorter waves. This is because for T_p= 2.5 s the wave spectrum is dominated by longer wave periods and thus longer wavelengths appear in the numerical wave tank. For a lower value of T_p = 1.18 s, the

spectrum consists of shorter wave periods and hence the free surface in the wave tank is composed of the correspondingly shorter wavelengths, giving it the appearance of a short-crested wave field.

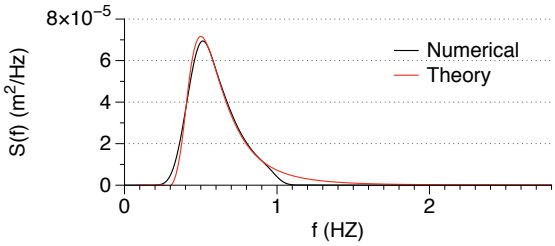

(a) Wave Gauge at $x = 5$ m

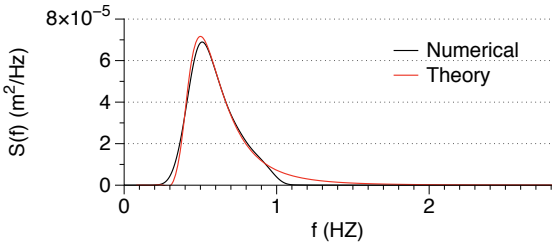

(b) Wave Gauge at $x = 15$ m

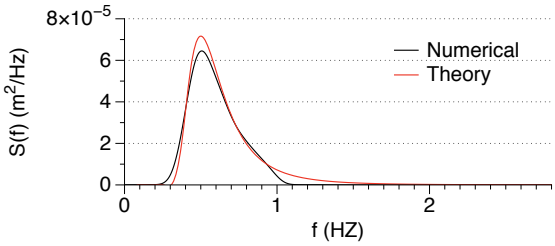

(c) Wave Gauge at $x = 20$ m

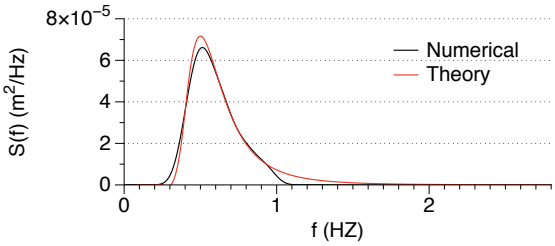

(d) Wave Gauge at $x = 25$ m

Figure 4.9: $N = 25$, $dx = 0.01$ m, $H_s = 0.02$ m, $T_p = 2.0$ s

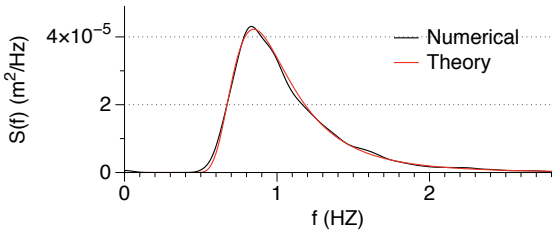

(a) Wave Gauge at $x = 5$ m

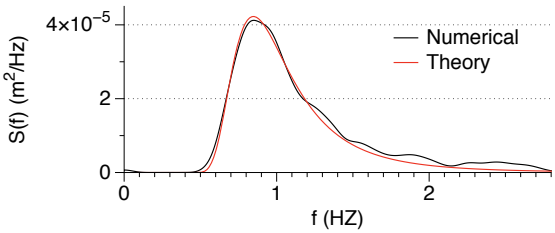

(b) Wave Gauge at $x = 15$ m

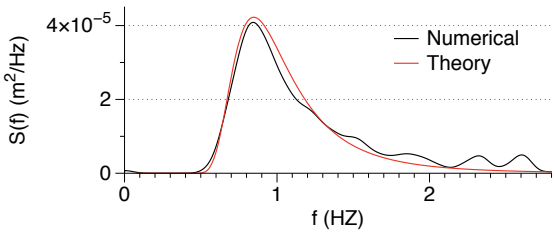

(c) Wave Gauge at $x = 20$ m

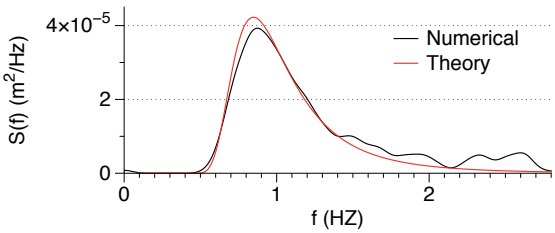

(d) Wave Gauge at $x = 25$ m

Figure 4.10: $N = 25$, $dx = 0.01$ m, $H_s = 0.02$ m, $T_p = 1.18$ s

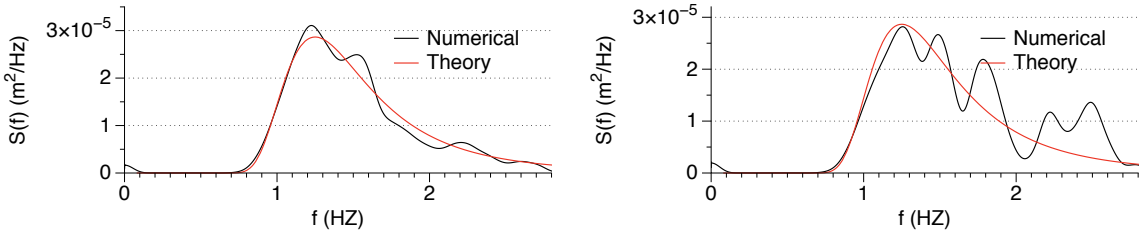

(a) Wave Gauge at $x = 5$ m

(b) Wave Gauge at $x = 15$ m

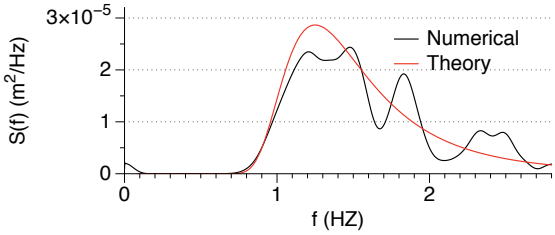

(c) Wave Gauge at $x = 20$ m

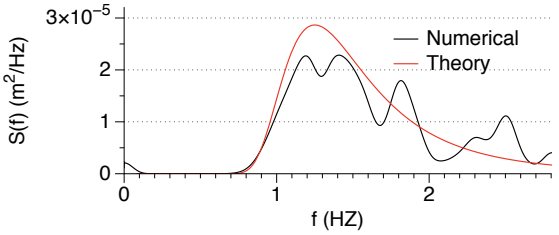

(d) Wave Gauge at $x = 25$ m

Figure 4.11: $N = 25$, $dx = 0.01$ m, $H_s = 0.02$ m, $T_p = 0.8$ s

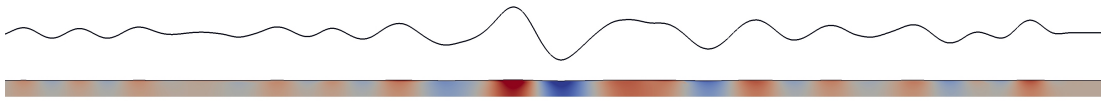

Figure 4.12: Scaled up free surface elevation with horizontal velocity contours in NWT for $N = 25$, $dx = 0.01$ m, $H_s = 0.02$ m, $T_p = 2.5$ s

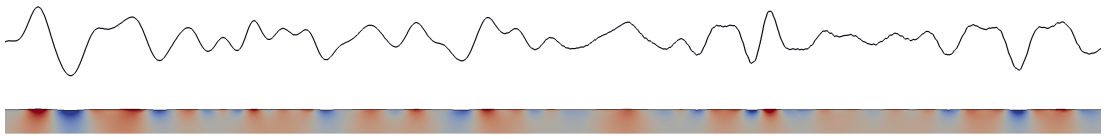

Figure 4.13: Scaled up free surface elevation with horizontal velocity contours in NWT for $N = 25$, $dx = 0.01$ m, $H_s = 0.02$ m, $T_p = 1.18$ s

4.1.4 Effect of length of simulation time

This section of paper studies the effect of the length of simulation time on the numerical results. The other parameters such as the grid size $dx = 0.01$ m, the significant wave height $H_s = 0.02$ m, the number of waves N= 25 and the peak wave period = 1.18 s are kept constant. The simulations are run for a duration of of 60 s, 120 s, 240 s, 500 s, 1000 s and 3600 s. It is observed that the results with the lower durations

do not agree well with the theoretical results. It is seen from the Figure 4.14 that the higher frequencies are under represented as the wave propagates through the wave tank. This is because with a shorter duration of the simulation there are not a significant number of waves being evolved. It takes some time for the waves to evolve fully and propagate. Also, the spurious peaks can be clearly observed in the spectrum as the wave propagates.

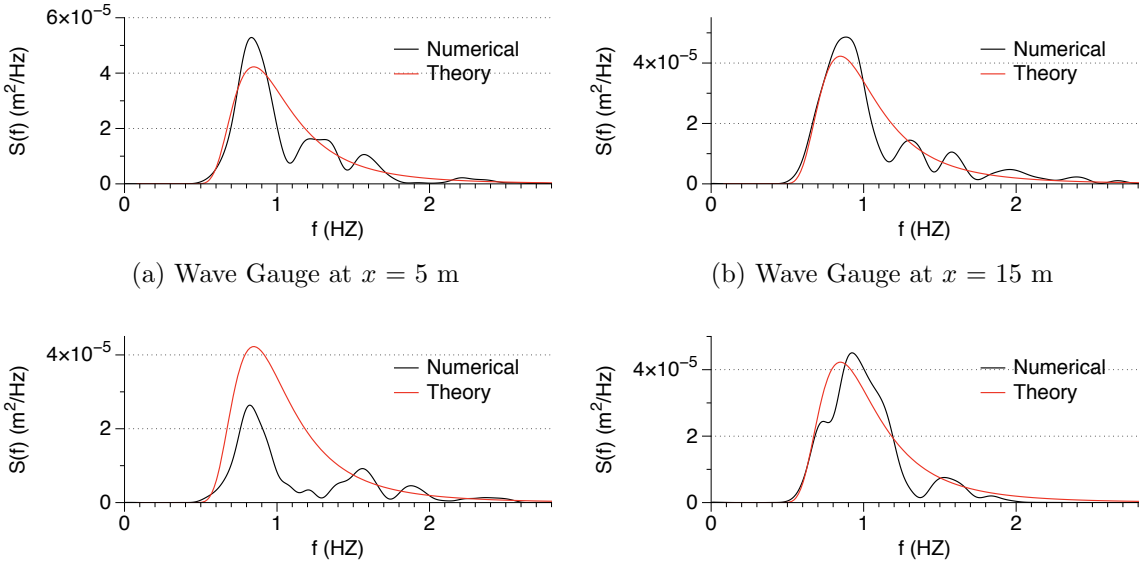

(a) Wave Gauge at $x = 5$ m

(b) Wave Gauge at $x = 15$ m

(c) Wave Gauge at $x = 20$ m

(d) Wave Gauge at $x = 25$ m

Figure 4.14: $N = 25$, $T_p = 1.18$ s, $dx = 0.01$ m, $H_s = 0.02$ m, Simulation time = 60 s

Figure 4.15 shows the results for the simulation duration = 120 s. It is clearly observed that for the incident spectrum for the wave gauge at $x = 5$ m, results are significantly better than the previous case. This depicts that with a higher duration of the numerical simulation, the incident wave spectrum is in a better agreement with the theory. Also for the wave gauge at $x = 15$ m, which is the first wave gauge in the working zone of the numerical tank, the numerical spectrum still under represents the higher frequency range waves from 1.1 Hz to 2.0 Hz. Some spurious peaks are also observed for the wave gauges at the farther locations in the NWT. The Figure 4.16 shows that for a simulation duration = 240 s, the results for the wave gauge at $x = 5$ m and 15 m are a good match with the theoretical results. But, for the wave gauges at $x = 20$ m, for the frequency range of 1.15 Hz to 1.45 Hz and for the wave gauge at $x = 25$ m, for the frequency range of 0.60 Hz to 1.00 Hz, the numerical spectrum does not agree well with the theory.
Figure 4.17 shows the results for a duration time of simulation = 500 s. It is clearly observed that the incident wave spectrum for the wave gauge at $x = 5$ m, matches perfectly with the theoretical wave spectrum. For the wave gauge locations in the wave tank, the results agree well with the theoretical predicted results for all of them. There are no spurious peaks observed and the wave propagate undamped through

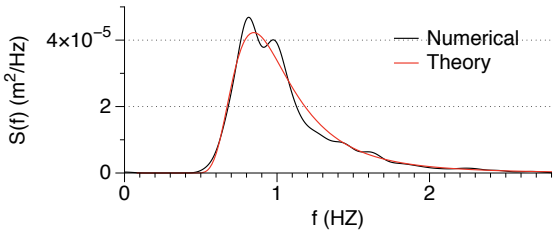

(a) Wave Gauge at $x = 5$ m

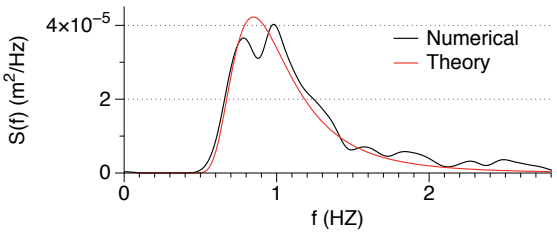

(b) Wave Gauge at $x = 15$ m

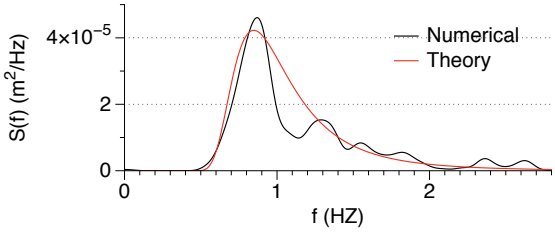

(c) Wave Gauge at $x = 20$ m

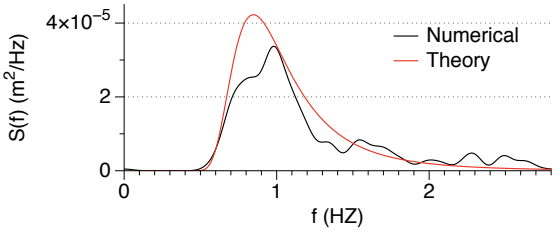

(d) Wave Gauge at $x = 25$ m

Figure 4.15: $N = 25$, $T_p = 1.18$ s, $dx = 0.01$ m, $H_s = 0.02$ m, Simulation time = 120 s

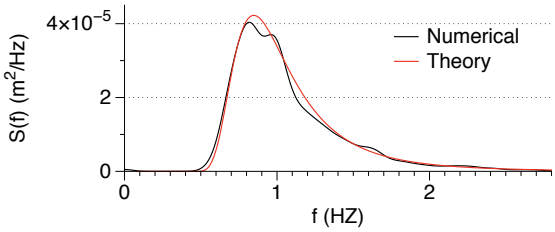

(a) Wave Gauge at $x = 5$ m

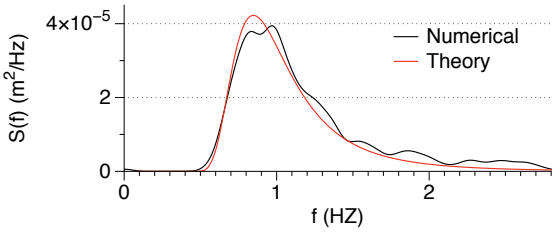

(b) Wave Gauge at $x = 15$ m

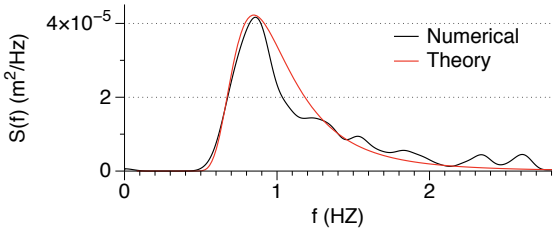

(c) Wave Gauge at $x = 20$ m

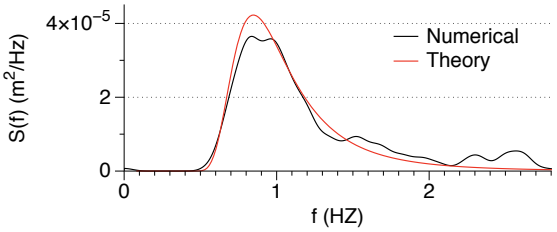

(d) Wave Gauge at $x = 25$ m

Figure 4.16: $N = 25$, $T_p = 1.18$ s, $dx = 0.01$ m, $H_s = 0.02$ m, Simulation time = 240 s

the wave tank and the waves in all frequencies are represented properly. The Figures 4.18 and 4.19 show the results for a duration of 1000 s and 3600 s, the quality of results is improved but the improvement is not significant.

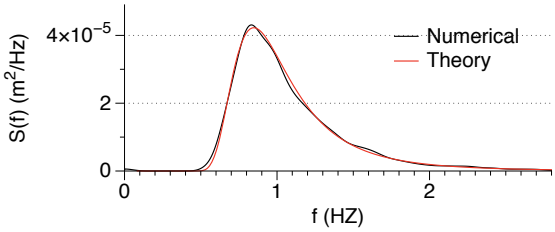

(a) Wave Gauge at $x = 5$ m

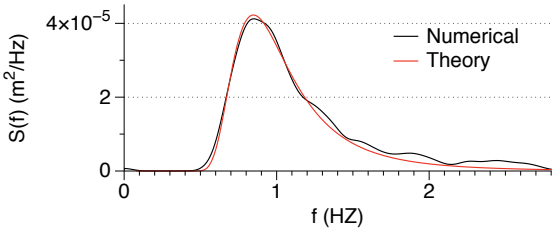

(b) Wave Gauge at $x = 15$ m

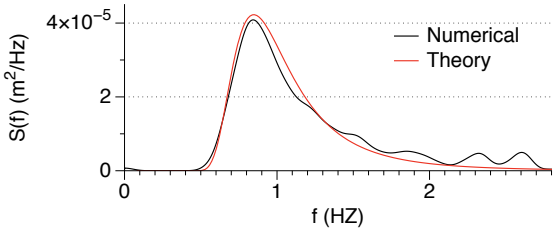

(c) Wave Gauge at $x = 20$ m

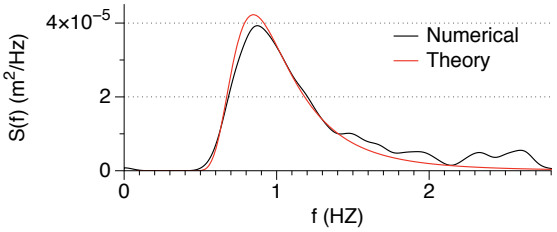

(d) Wave Gauge at $x = 25$ m

Figure 4.17: $N = 25$, $T_p = 1.18$ s, $dx = 0.01$ m, $H_s = 0.02$ m, Simulation time = 500 s

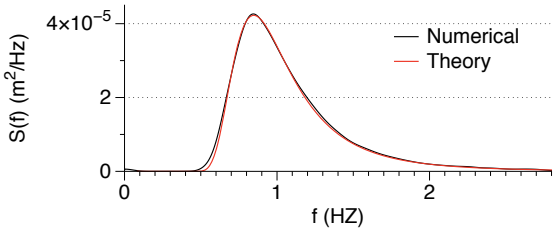

(a) Wave Gauge at $x = 5$ m

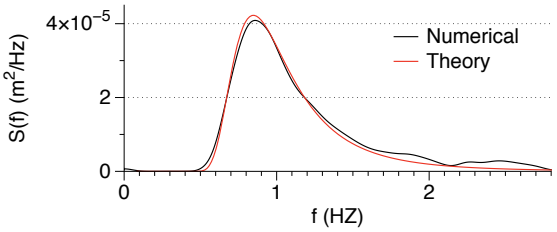

(b) Wave Gauge at $x = 15$ m

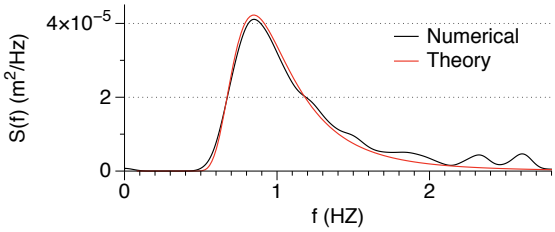

(c) Wave Gauge at $x = 20$ m

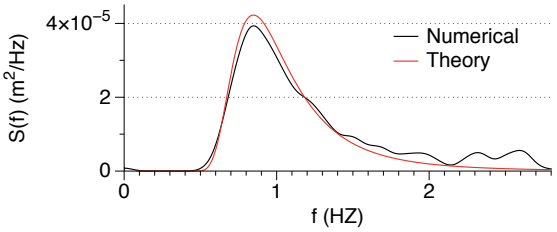

(d) Wave Gauge at $x = 25$ m

Figure 4.18: $N = 25$, $T_p = 1.18$ s, $dx = 0.01$ m, $H_s = 0.02$ m, Simulation time = 1000 s

The comparison between the Figures shows that for a lesser simulation duration = 60 s, 120 s and 240 s, the numerical spectrum does not represent the waves in a higher frequency range well for the wave gauges located at the farther locations

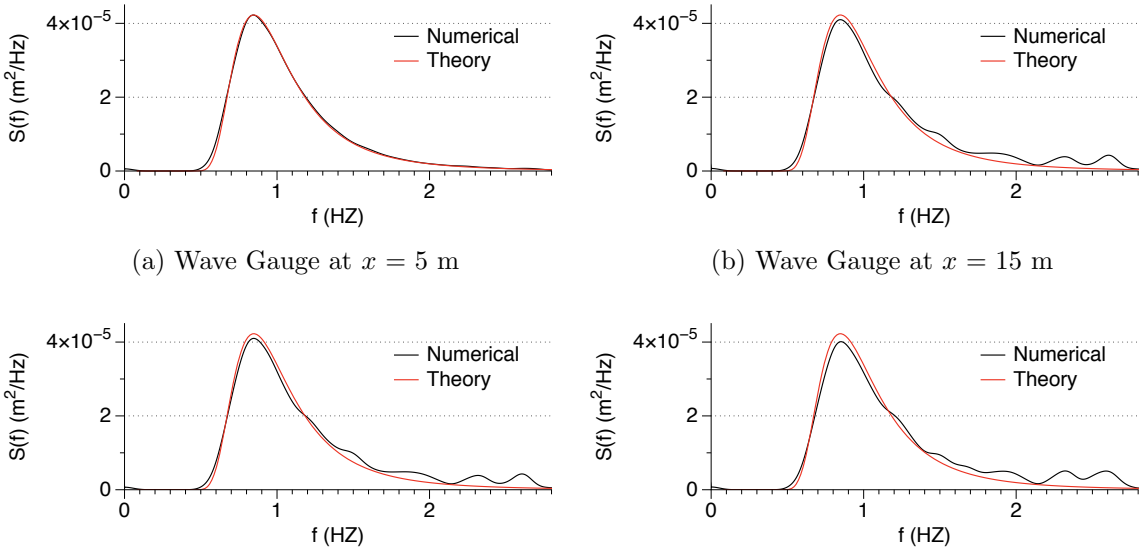

(a) Wave Gauge at $x = 5$ m

(b) Wave Gauge at $x = 15$ m

(c) Wave Gauge at $x = 20$ m

(d) Wave Gauge at $x = 25$ m

Figure 4.19: $N = 25$, $T_p = 1.18$ s, $dx = 0.01$ m, $H_s = 0.02$ m, Simulation time = 3600 s

in the NWT. On comparing the Figures 4.14, 4.15 and 4.16 it is clearly observed that the wave spectra for the farther wave gauge locations shows spurious peaks and under representation of the higher frequency waves which start disappearing when the simulation duration increases. Figure 4.17 shows that for a simulation duration = 500 s, spurious peaks and under representation disappears to an acceptable extent. However, results for the simulation with the duration = 3600 s are the best, but it should be kept in mind that this is computationally expensive. Here it is more of a trade-off between accuracy and computational time. So, a simulation of duration = 500 s is considered to be sufficient to obtain a good representation.

4.2 Irregular wave propagation over a submerged bar

This section of the chapter is an application of the study in the previous section. After the verification of the irregular wave generation, this section deals with the study of irregular wave hydrodynamics when they interact with a submerged bar. To study their behaviour, the results from the numerical model are compared with the experiments by Beji and Battjes (1993).

4.2.1 Experimental Setup

In the experimental setup by Beji and Battjes (1993), the length of the wave flume is 37.70 m, the width is 0.8 m and the height is 0.75 m. The still water level over the horizontal bottom is set to 0.4 m. A piston type wave maker is used for generating irregular waves. A submerged trapezoidal bar with a weather side slope of 1:20 and 2 m horizontal crest followed by a 1:10 lee side slope is constructed at a distance of 6 m from the wave board. A beach with a weather side slope of 1:25 is used and its function is to act as wave absorber. Eight wave gauges are installed along the length of the flume in the experimental setup to measure the surface elevation. The JONSWAP spectrum is used for the irregular wave generation.

4.2.2 Numerical Setup

A 2D numerical wave tank is used to simulate the experiment described above and the numerical results are compared with the experimental data. The relaxation method as mentioned in chapter 3 is used to generate and to absorb the waves in the numerical wave tank. Similar to the experiments, irregular waves are used in the numerical model and the JONSWAP spectra is used for the analysis. The numerical setup is illustrated in the Figure 4.20.

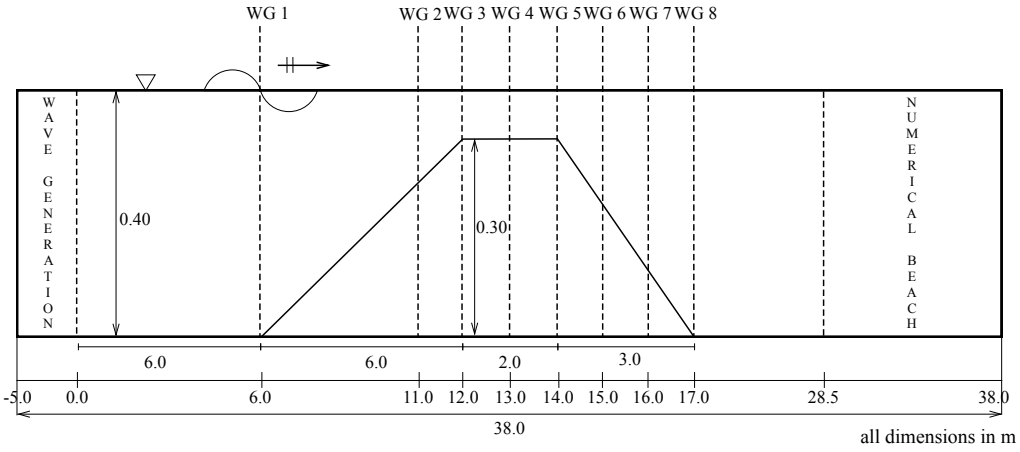

Figure 4.20: Numerical setup with the wave gauge positions for a submerged bar in the numerical wave tank

Two cases are tested, case 1 with a significant wave height $H_s = 0.022$ m and case 2 is with a significant wave height $H_s = 0.05$ m. Peak period $T_p = 2.5$ s is used in both the cases. Numerical results are compared with the experimental results for case 1 for testing. A grid size dx=0.01 m, simulation duration t= 500 s, peak time period T_p= 2.5 s are used for simulations for both cases.

4.2.3 Case 1: Non-breaking Irregular Waves

This subsection deals with the study of case 1. Here, a significant wave height, H_s = 0.022 m is used, the rest all parameters being kept same.

The Figure 4.21 show the results for the different waves gauges. The Figure 4.21a illustrates that for the first wave gauge before the bar, the incident wave spectrum is narrow and the wave energy is concentrated in the lower frequencies between = 0 Hz to 1.3 Hz. For the second wave gauge shown in the Figure 4.21b, the shoaling is expected due to the decrease of the water depth, which results in an increase of wave energy. Also, it is observed that the wave spectrum becomes slightly wider as compared to the incident wave spectrum and the frequency range for the wave energy distribution becomes 0 Hz to 1.9 Hz. Figures 4.21c and 4.21d show the wave spectrum for the wave gauges located over the horizontal crest. It is observed that the wave spectrum tends to become wider and the wave energy spreads over a wider range of the frequency between 0 Hz to 2.8 Hz. However, the major portion of the wave energy is still concentrated in the lower frequency range from 0 Hz to 1 Hz. The peak value of the spectrum is reduced, as the total energy should remain the same. And, the Figure 4.21e shows the result for the wave gauge located on the downslope of bar. It is observed that now energy is more concentrated in the higher frequencies from 0.8 Hz to 1.6 Hz unlike the incident wave spectrum. This is evident from the fact that area under curve for the higher frequencies is significantly more than the area under curve for the lower frequencies. Some secondary peaks can also be observed for this location of the wave gauge for both the experimental and numerical results.
However, it is clearly seen that the numerical results for all the wave gauges are in good agreement with the experimental results. The numerical model is able to simulate all the hydrodynamic phenomena as in the experiment.

4.2.4 Case 2: Breaking Irregular Waves

In this subsection the significant wave height, H_s = 0.05 m is chosen and the rest of the numerical and hydrodynamic parameters are kept the same. The numerical results for case 2 for the different wave gauges are shown in the Figure 4.22 below.
Wave breaking is observed in case 2, as seen from the Figure 4.23. The Figure 4.22a shows the incident wave spectrum for the wave gauge at x = 6 m, the wave energy is limited to lower frequency range from 0 Hz to 1.3 Hz. The Figure 4.22b shows the wave spectrum for the wave gauge at x = 11 m, which is located on the weather side slope of the bar. It is seen that wave energy spreads over a wider frequency range between 0 Hz to 2.8 Hz and some secondary peaks are observed. The Figure 4.22c and Figure 4.22d show that the amount of energy being distributed to the higher frequencies, between 0.8 Hz to 2.8 Hz increases gradually. A significant difference between the values of the peaks can be seen in the Figure 4.22d and Figure 4.22e. Due to the breaking some energy is dissipated, while the spectrum is also significantly wider as

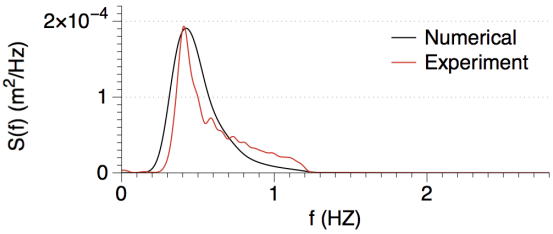

(a) Wave Gauge at $x = 6$ m

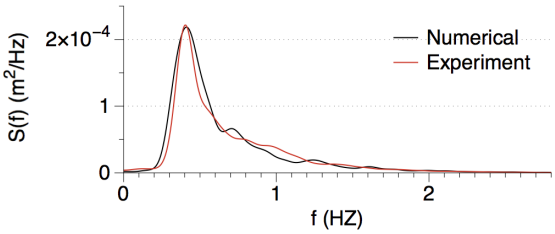

(b) Wave Gauge at $x = 11$ m

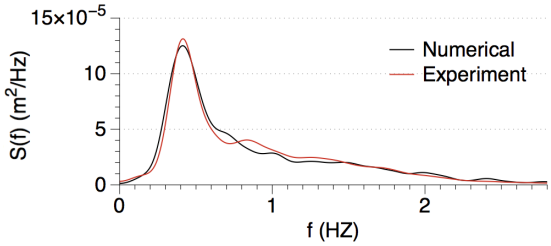

(c) Wave Gauge at $x = 12$ m

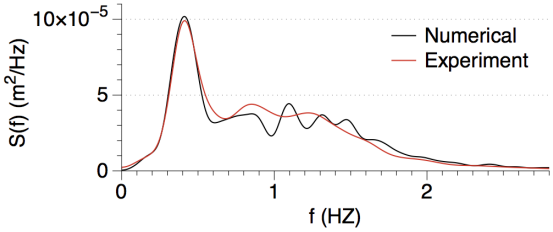

(d) Wave Gauge at $x = 13$ m

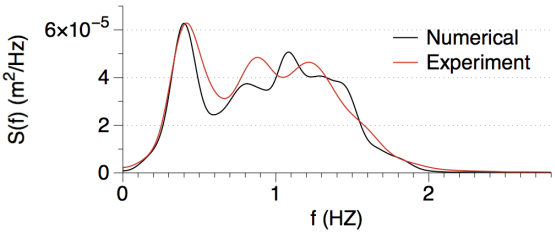

(e) Wave Gauge at $x = 16$ m

Figure 4.21: $T_p = 2.5$ s, $dx = 0.01$ m, $H_s = 0.022$ m, Simulation time = 500 s

compared to the incident spectrum with a more amount of energy being distributed to the higher frequencies between 1 Hz to 2.3 Hz.

Since, the wave energy is directly related to the wave height, the peak of the spectrum is higher in the case 2 as compared to the case 1. For the incident wave spectrum, all the wave energy is limited to the lower frequencies similar to case 1. As the waves propagate over the bar, the spectrum becomes wider and energy gets distributed to a wider range of frequencies similar to case 1. It should be noted that in this case some small secondary peaks are observed unlike case 1 for the wave gauge at the crest of the bar.

Figure 4.23 show the wave propagation over the bar. Figure 4.23a shows the wave over the weather side slope of the bar. Incident waves generated in the wave generation zone propagate over the weather side slope, where their wave heights tend to increase due to a decreasing water depth, this phenomena is called as the shoaling. Figure 4.23b shows the wave over the crest of the bar, where the waves have already shoaled

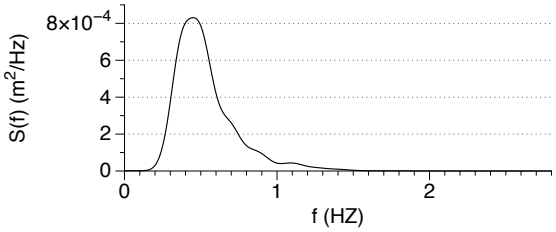

(a) Wave Gauge at $x = 6$ m

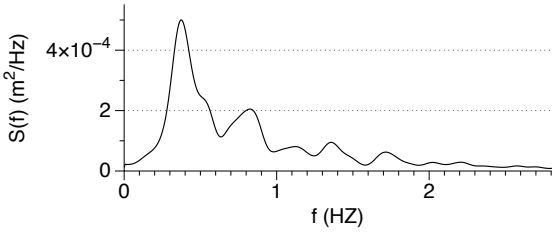

(b) Wave Gauge at $x = 11$ m

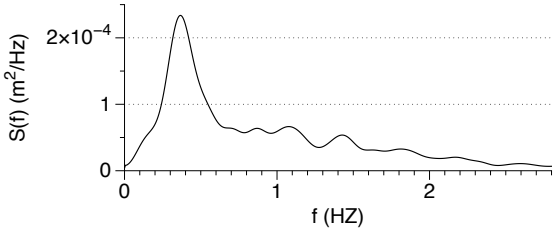

(c) Wave Gauge at $x = 12$ m

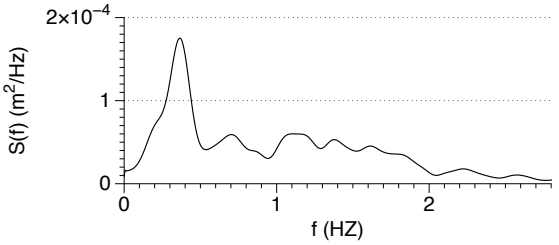

(d) Wave Gauge at $x = 13$ m

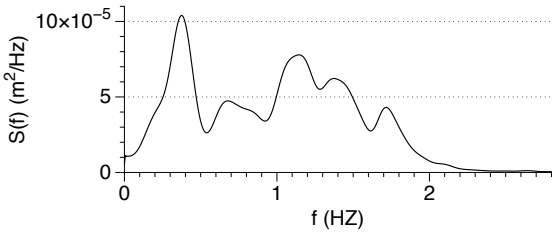

(e) Wave Gauge at $x = 16$ m

Figure 4.22: $T_p = 2.5$ s, $dx = 0.01$ m, $H_s = 0.05$ m, Simulation time = 500 s

and they tend to have a breaker tongue on this part. The wave crest becomes unstable and starts breaking when the particle velocity exceeds the velocity of the wave crest. The breaking condition corresponds to an angle of 120 degrees (Bosboom and M.J.F., 2011). The breaker point, the point where the wave height suddenly decreases because the largest wave in the wave field starts breaking is achieved here. It is clearly depicted in the Figure 4.23b. The Figure 4.23c shows that the wave breaking has already taken place and energy is already been dissipated. Figure 4.23d shows the dissipated wave after the breaking.

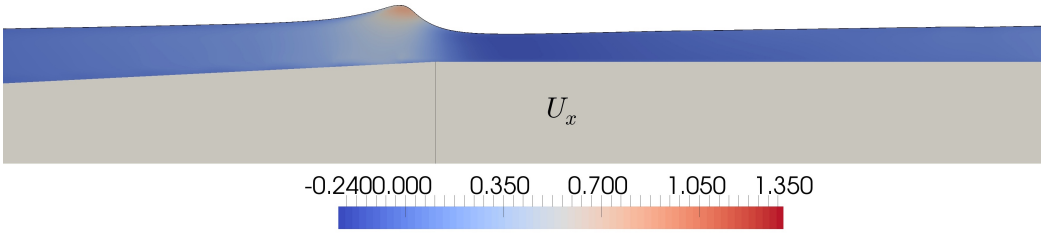

(a) Wave over the upslope of bar tending to shoal

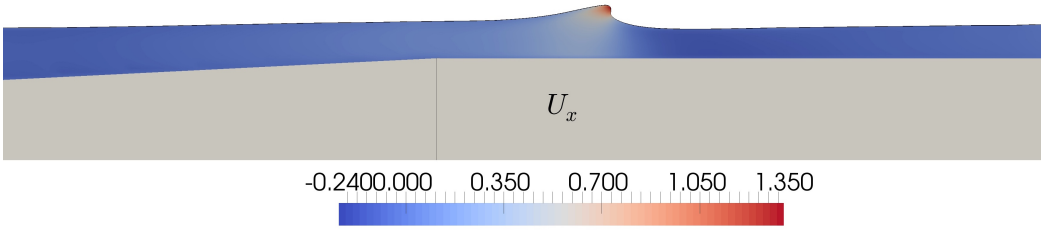

(b) Wave over the flat crest of bar with a breaker tongue

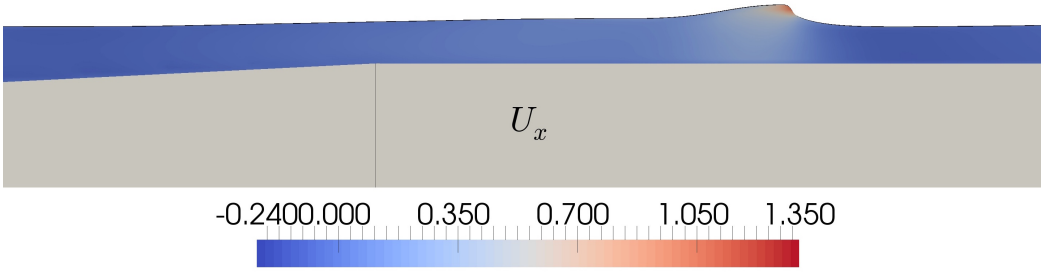

(c) Wave over the flat crest of bar just after breaking

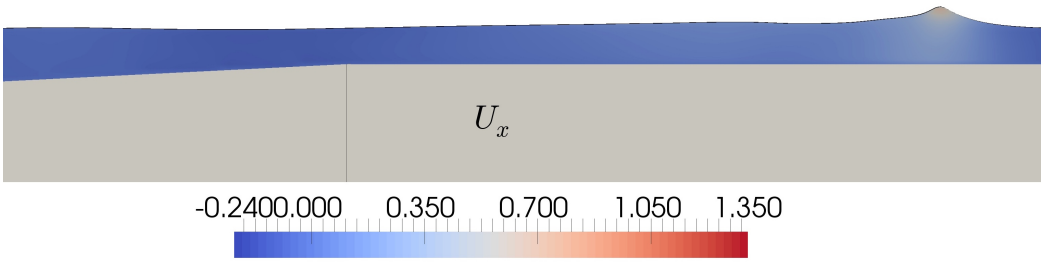

(d) Wave propagation after energy dissipation has taken place during breaking

Figure 4.23: $T_p = 2.5$ s, $dx = 0.01$ m, $H_s = 0.05$ m, Simulation time = 500 s

Chapter 5

Wave forces on a horizontal cylinder

5.1 Different kinds of the wave forces on the structures

This chapter deals with the behaviour of irregular wave forces on a submerged horizontal cylinder. The wave forces experienced by the structure depends on the various parameters like the type of the structure, the type of the waves, the type of flow, etc. Then, there are various dimensionless parameters which determine the type of flow like the Reynolds number, the Strouhal number and the Keulegan-Carpenter number. In this study, the last parameter is the most important one.
The Keulegan-Carpenter number (KC), gives an indication of the flow type when the flow is oscillatory depending on the amplitude of flow velocity U_m, the time period $T$and the diameter D, as shown below:

$$KC = \frac{U_m T}{D} \tag{5.1}$$

The other parameter is the Strouhal Number S_0. This is taken into account when phenomena like the flow separation and the vortex formation are occuring. It takes into account the shedding frequency f_0, the diameter D and the flow velocity U.

$$S_0 = \frac{f_0 D}{U} \tag{5.2}$$

When the structure is in an undisturbed wave field, the force exerted by the fluid on the structure is computed by the integration of the pressure around it. This force is called the Froude-Krylov Force f_{FK}. This is defined for the fluid density ρ, the cylinder diameter D and the flow acceleration $\dot{u}$

$$f_{FK} = \rho \left(\frac{\pi D^2}{4} \right) \dot{u} \tag{5.3}$$

Another force exerted on the cylinder in the wave field is called the form drag force, this force is an analogy to the frictional force. A structure perpendicular to the flow experiences the frictional force often termed as the form drag force f_d, expressed in terms of per unit length usually as:

$$f_d = \frac{1}{2}\rho C_d D u|u| \tag{5.4}$$

where, C_d is the drag coefficient, D is the cylinder diameter and u is the flow velocity

5.1.1 Morison Formula

In the cases involving the flow separation, the vortex shedding, forces on the cylinder becomes even more complex. Apart from the flow field it also depends on the flow history of the flow. In these conditions the Morison equation is used to calculate the force f. The Morison Equation is given as:

$$f = \frac{1}{4}C_m \pi D^2 \rho \dot{u} + \frac{1}{2}C_d \rho D u|u| \tag{5.5}$$

where, C_m is the inertia coefficient and $\dot{u}$ is the flow acceleration. The forces mentioned in the above equation gives the force per unit length.

5.2 Force Calculation in REEF3D

In REEF3D (Alagan et al., 2015), the forces are calculated by integrating the pressure around the cylinder. With the help of the numerical model, the surface is accurately determined and then pressure is calculated around it. The surface normal vectors are produced first, and the sum is then integrated over the surface for calculating the force. It can be expressed as:

$$F = \int_{\Gamma} (-\mathbf{n}p + \mathbf{n}.\tau) d\Gamma \tag{5.6}$$

where, p represents pressure vector and τ is the stress tensor

5.3 Numerical wave tank setup

The numerical force calculated from REEF3D and the experimental force results are compared to test and to validate REEF3D for the wave forces on a horizontal cylinder. The numerical simulations are carried out with the same parameters as done in the experiment by Chaplin and Subbiah (1997). A fully submerged horizontal circular cylinder of diameter = 0.21 m fully is considered. The depth of numerical wave tank is 5 m. The cylinder is located 1.75 m under the still water level. The total length of the numerical wave tank is 190 m. The length of the wave generation zone is 38 m

and the beach is 76 m long. The experimental test is done for a cylinder of diameter = 0.21 m.
The numerical wave tank is tested and validated for the diameter of 0.21 m by comparing the numerical force spectrum with the experimental force spectrum. Tests are done with irregular waves with a significant wave height $H_s = 1.5$ m and a peak time period $T_p = 5.9$ s. The corresponding KC number is 11.12. A grid size $dx = 0.05$ m is chosen for the numerical simulations. The simulation duration is chosen to be 500 s. The numerical wave tank setup is shown in the Figure 5.1 below:

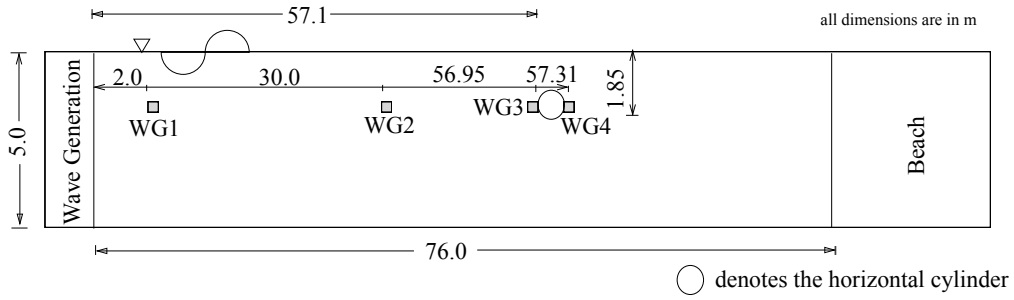

Figure 5.1: The Numerical Wave Tank setup of a horizontal cylinder

5.4 Validation with regular waves

Simulations are also carried out for the regular waves. The numerical wave forces are compared with the experimental wave forces (Chaplin and Subbiah, 1997). The regular wave tests are done with the waves of wave height, $H = 1.08$ m and time period, $T = 3.5$ s. The other parameters are kept same as the case with irregular waves and they are: cylinder diameter, $D = 0.21$ m, grid size, $dx = 0.05$ m. The simulations are run for a duration = 500 s. The free surface elevations for the wave gauges WG3 and WG4, which are located just before and after the cylinder respectively, are compared in order to study the behaviour of the regular waves during their interaction with a structure. Figure 5.2 shows the comparison for both:

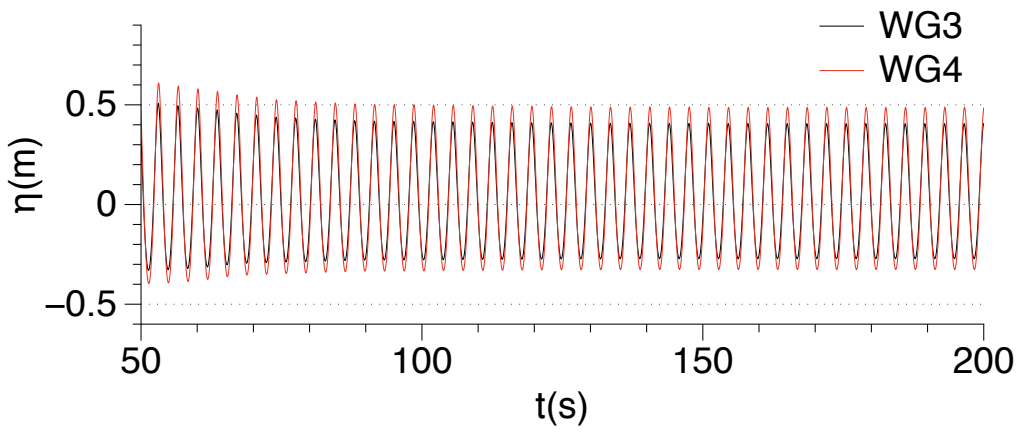

Figure 5.2: Free surface elevation before and after the cylinder for the regular waves at WG3 and WG4 respectively, for $D = 0.21$ m, $dx = 0.05$ m, $H = 1.08$ m, $T = 3.5$ s, Simulation time = 500 s

It is observed from the Figure 5.2 that the regularity and the shape of the waves is maintained before and after the interaction. However, the WG4 shows slightly higher peaks as compared to WG3. This might be due to the possible shoaling. Figure 5.3 presents the wave spectra for the regular waves before and after the wave-cylinder interaction. Bell's shaped curve is observed for the regular wave spectrum unlike the irregular waves. The spectrum for WG3 shows a peak value = 0.42 m^2/Hz at the frequency = 0.29 Hz, while the spectrum for WG4 shows a peak value = 0.46 m^2/Hz at the frequency = 0.29 Hz. Both spectra are smooth and symmetric. However, it should be noted that the wave spectrum for WG4 is slightly narrower as compared to WG3. After the hydrodynamic study for the wave-cylinder interaction, a wave force study is also performed in order to understand the behaviour of the wave forces on a horizontal submerged cylinder.

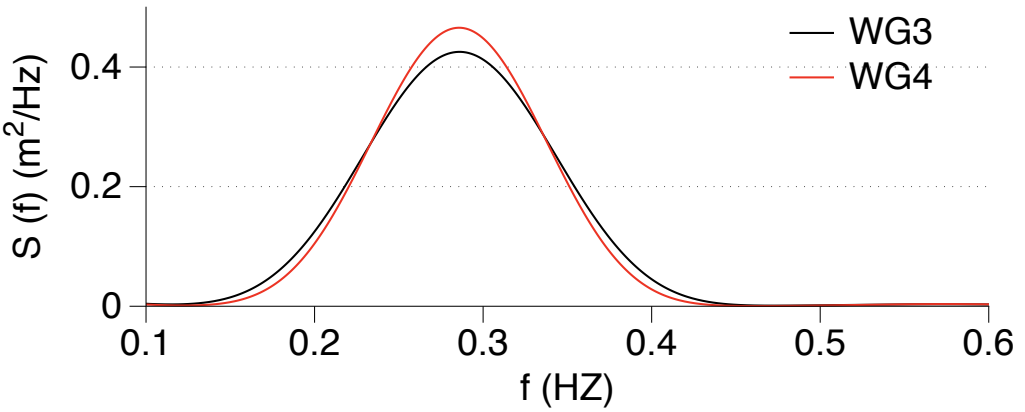

Figure 5.3: Wave spectra before and after the cylinder at WG3 and WG4 respectively, for $D = 0.21$ m, $dx = 0.05$ m, $H = 1.08$ m, $T = 3.5$ s, Simulation time = 500 s

The Figure 5.4 shows the comparison between numerical and experimental wave forces:

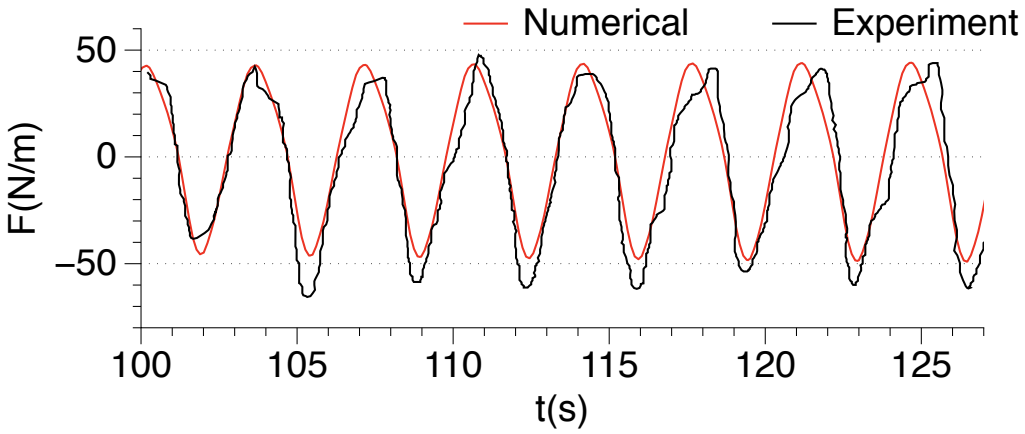

Figure 5.4: Comparison between experimental and numerical results for regular waves with $D = 0.5$ m, $dx = 0.05$ m, $H = 1.08$ m, $T = 3.5$ s

It can be observed from the Figure 5.4 that the numerical and the experimental results are in a good agreement. However, the negative force peaks for the experimental results have a slightly higher absolute value than the numerical results. The numerical results show a uniform force pattern with the time, which is confirmed by the experimental results. The average value for the numerical force for the positive half is 43 N/m, while this value for the experimental force is 41.4 N/m. Thus, the two values are very close. However, in the negative half of the wave force plot, numerical peaks have an average absolute value of 48 N/m, while for experimental results this value is 58 N/m. The wave force behaviour is exactly simulated by the numerical model as shown by the experimental observations. Thus, REEF3D can be used as a good tool to simulate the wave forces for a horizontal cylinder.

5.5 Irregular Waves

5.5.1 Validation with the experiment and grid convergence tests

The JONSWAP spectrum is used for the wave generation. The numerical model and the experiment measure the force with time series. For the spectral analysis, the force-time series measurements are converted into force spectrum, the spectral analysis is done using the technique explained in chapter 3 by employing FFT. The numerical model is validated for the force results by comparing the numerical results with the experimental results for a cylinder diameter,$D = 0.21$ m. The numerical simulations are done for the three different grid sizes, $dx = 0.25$ m, 0.10 m and 0.05

m. The Figure 5.5 shows the comparison of the numerical results for the different grid sizes with the experimental results.

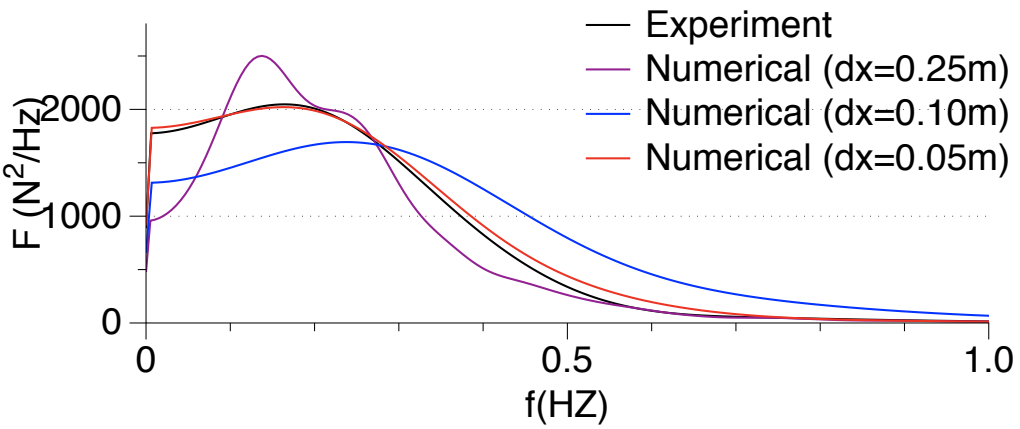

Figure 5.5: Grid convergence in comparison with experimental results for $D = 0.21$ m, $T_p = 5.9$ s, $H_s = 1.5$ m, KC number = 11.12, Simulation time = 500 s

It is illustrated from the Figure 5.5 that the numerical results with a grid size $dx = 0.05$ m are in a good agreement with the experimental results. The results with a grid size $dx = 0.25$ m show the peak value at the frequency $f_p = 0.14$ Hz. The frequency range corresponding to $F_p/3$ is 0 Hz to 0.38 Hz. The results with a grid size, $dx = 0.10$ m show that the peak of the spectrum is at frequency $f_p = 0.24$ Hz. The spectrum is wider, proven by the frequency range corresponding to $F_p/3$ which is 0 Hz to 0.65 Hz. The results with grid size $dx = 0.05$ m show that the peak of the numerical force spectrum matches well with the experimental peak of the spectrum at $f_p = 0.18$ Hz. At the higher frequencies, a similar behaviour is shown by both spectra. Thus, it can be clearly inferred from the Figure 5.5 that the results with a coarser grid sizes do not give a good results. The peak shown by the numerical results for coarser grid sizes $dx = 0.1$ m and $dx = 0.25$ m do not match with the experimental peaks. Also, the shape of the spectrum for grid size $dx = 0.25$ m is different than the shape of the experimental spectrum. The results with grid size $dx = 0.05$ m are in a very good agreement with experimental wave force results.

The free surface elevation with time is shown in the Figure 5.6 for the wave gauges WG3 and WG4, which are located before and after the cylinder, respectively. It is clearly observed that the free surface elevation has slightly higher peaks for the WG4 located just after the cylinder. It can also be seen that the spread of the waves and shape of the waves remains unchanged after their interaction with the cylinder.

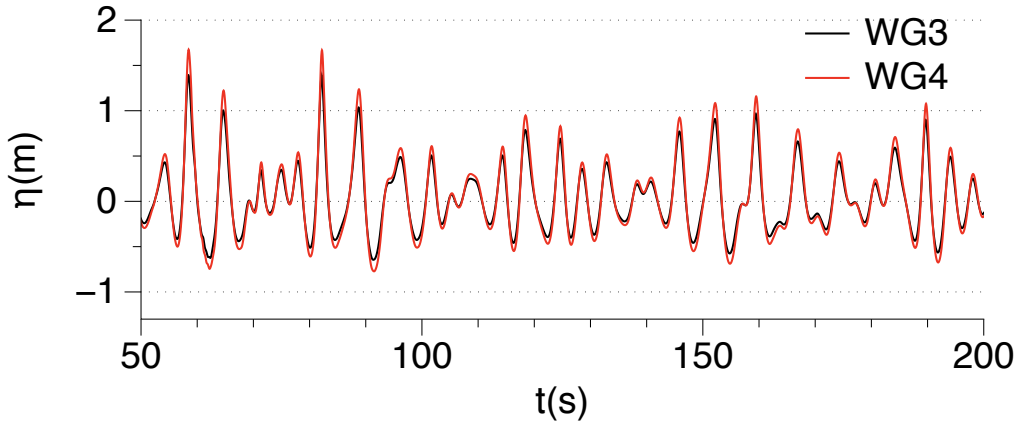

Figure 5.6: Free surface elevation before and after the cylinder at WG3 and WG4 respectively, for $D = 0.21$ m, $dx = 0.05$ m, $H_s = 1.5$ m, $T_p = 5.9$ s, KC number = 11.12, Simulation time = 500 s

Figure 5.7 presents the wave spectra just before and after the wave-cylinder interaction.

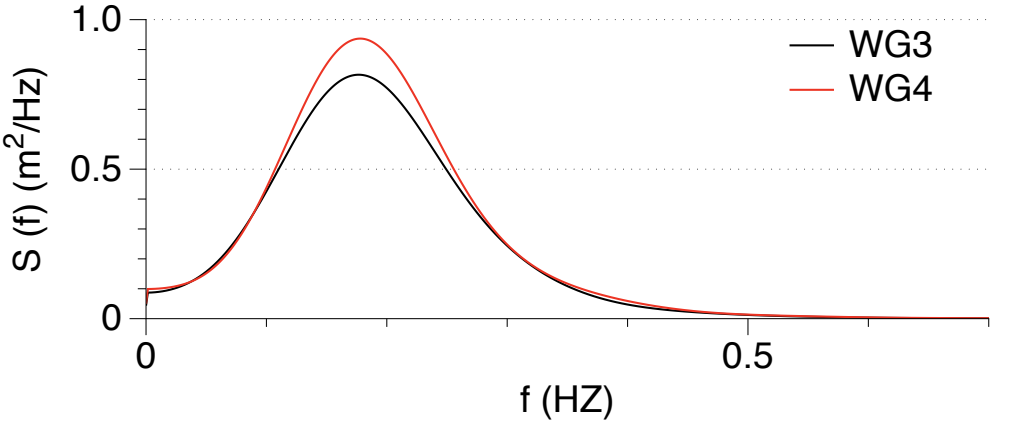

Figure 5.7: Wave spectra before and after the cylinder at WG3 and WG4 respectively, for $D = 0.21$ m, $dx = 0.05$ m, $H_s = 1.5$ m, $T_p = 5.9$ s, KC number = 11.12, Simulation time = 500 s

It is inferred from Figure 5.7 that the wave spectrum for the WG3, which is located just before the cylinder, shows a peak value of 0.81 m^2/Hz at the frequency $f_p = 0.17$ Hz. WG3. It is located just after the cylinder and shows a peak value of 0.93 m^2/Hz at the frequency $f_p = 0.17$ Hz. The spectrum peak for the WG4 has a higher value than the spectrum peak for WG3. The locations of the peaks remains unchanged, spectra in the both cases show a peak value at 0.17 Hz. Also, the shape and spread of the wave spectra remain the same. This illustrates that no distortion of the wave spectrum takes place in this case as it propagates over the cylinder. For both cases,

the wave energy is limited between the frequency range from 0 Hz to 0.5 Hz. This also further states the fact that the spread of the waves remains the same before and after their interaction with the cylinder. This might be due to the fact that since the cylinder is submerged, slight shoaling of the waves takes place due to the overtopping.

5.5.2 Testing with different KC numbers

As inferred from above section that the numerical model gives a good match with the experimental wave force results for the irregular waves for a horizontal submerged cylinder. Numerical simulations are done for KC numbers = 5.02 and 15.02. The peak wave period, T_p is varied to 3.2 s and 7.5 s, respectively in order to vary the KC number, keeping the diameter of cylinder, D and significant wave height H_s constant. The force spectrum for all the KC numbers is compared in the Figure 5.8 for the cylinder diameter $D = 0.21$ m.

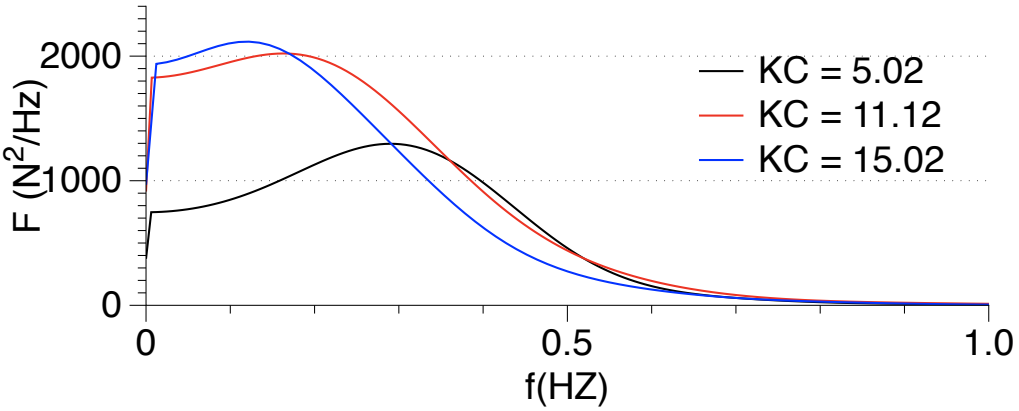

Figure 5.8: Numerical results with the different KC numbers, $D = 0.21$ m, $dx = 0.05$ m, $H_s = 1.5$ m, Simulation time = 500 s

It is observed that the value of the peak of the force spectrum is higher with a higher KC number. It signifies that waves with a higher value of peak time period, T_p exert more force on a submerged horizontal cylinder. The force spectrum for the longer waves with $T_p = 7.5$ s with a KC number = 15.02 has the peak value, F_p at frequency $f_p = 0.13$ Hz. The shape of the spectrum is not symmetric. The frequency range corresponding to $F_p/3$ is 0 Hz to 0.41 Hz. It can be observed that the spectrum attains its peak sharply and then it decays gradually as compared to the beginning. Thus, it can be inferred that for the lower frequency range between the frequency range of 0 Hz to 0.1 Hz, the force spectrum rises sharply and for the higher frequency range between 0.1 Hz to 0.8 Hz the spectrum decays gradually. Also, it is more concentrated towards the higher frequency range. The force spectrum for the waves with a peak time period, $T_p = 5.9$ s, with a KC number = 11.12, has a peak value at frequency, $f_p = 0.18$ Hz. The frequency range corresponding to $F_p/3$ is 0 Hz to 0.44

Hz. It is observed that the force spectrum rises sharply in the lower frequency range from 0 Hz to 0.14 Hz and then decays smoothly in the higher frequency range from 0.14 Hz to 0.8 Hz with a more concentration of values towards the higher frequency side. The spectrum for the waves with peak time period, T_p = 3.2 s with a KC number = 5.02 peaks at the frequency f_p = 0.31 Hz. The initial rise of the spectrum in the frequency range 0 Hz to 0.07 Hz is sharp, while the spectrum rises smoothly in the range from 0.07 Hz to 0.31 Hz and then decays in the range of 0.31 Hz to 0.8 Hz. The comparison between the three spectra shows that the shape of the spectrum is maintained in all the cases. The spectrum with a lower value of KC number is relatively wider and more percentage of the force spectrum values are concentrated to the higher frequency side as compared to the spectrum with the higher KC numbers.

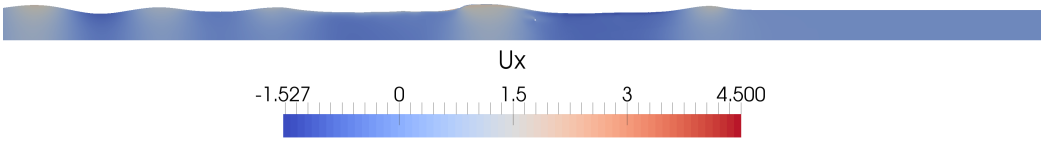

(a) Numerical wave tank coloured with velocity for the irregular waves with a horizontal submerged cylinder for the time step = 650 s

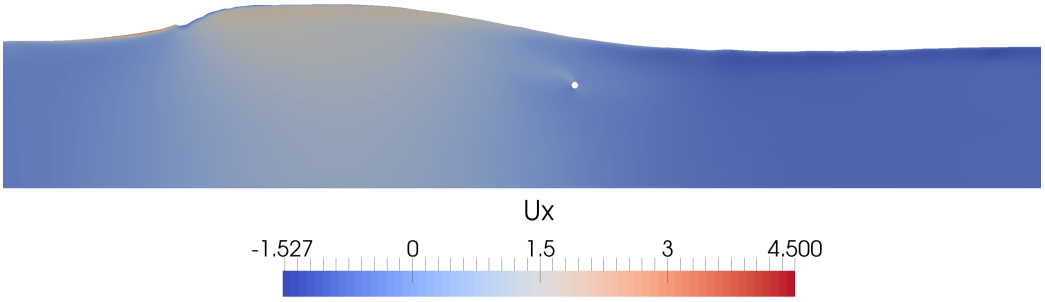

(b) Zoomed view of the numerical wave tank around cylinder for the time step = 650 s

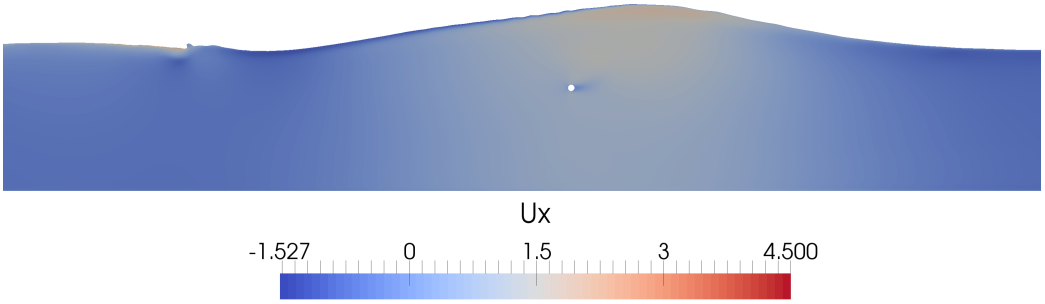

(c) Zoomed view of the numerical wave tank around cylinder for the time step = 682 s

Figure 5.9: T_p = 5.9 s, dx = 0.05 m, H_s = 1.5 m, Simulation time = 500 s

The Figure 5.9 illustrates the interaction of waves with the horizontal cylinder for the waves with peak time period, T_p = 5.9 s, with a KC number = 11.12. Figure

5.9a shows the numerical wave tank coloured with velocity. The irregular free surface of the numerical wave tank is shown. The horizontal submerged cylinder can also be seen in the Figure. Since the diameter of the cylinder is very small as compared to the size of wave tank, a zoomed view of hydrodynamics around cylinder is shown in the Figure 5.9b. It is observed in the Figure 5.9c that just after the interaction with the cylinder, the wave height has increased due to the overtopping. This is also in agreement with Figure 5.7 where the wave spectrum observed for WG4 which is located just after the cylinder shows a higher peak than WG3 which is located just before the cylinder. Also, some little flow contraction can be observed around the cylinder.

Figure 5.10a demonstrates the wave interaction with the horizontal cylinder for the waves with peak time period $T_p = 3.2$ s, with a KC number = 5.02. It is evinced from the free surface of the numerical wave tank that it is dominated by the shorter waves. The horizontal submerged cylinder can also be observed in the wave tank. A zoomed view around the cylinder can be seen in the Figure 5.10b for the same time step to study the hydrodynamics around the cylinder. The Figure 5.10c shows that waves are shoaled a bit while overtopping over the cylinder. Thus, the wave spectrum just after the wave gauge has a higher peak than just before the cylinder.
It is observed from the Figures 5.9 and 5.10 that the waves tend to shoal while overtopping over the cylinder. A similar behaviour is observed for the peak periods. However, it should be noted that the free surface for, $T_p = 5.9$ s is dominated by the longer waves while the free surface for $T_p = 3.2$ s is dominated by the shorter waves. A little amount of flow contraction round the cylinder is also observed in the both cases.

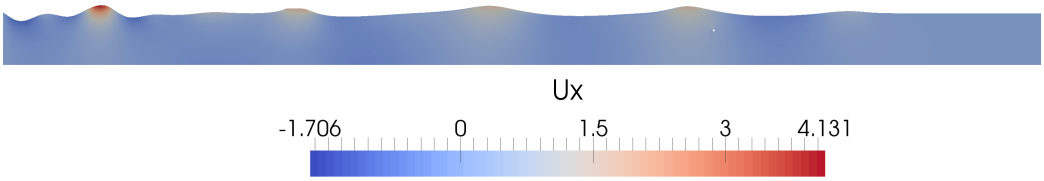

(a) Numerical wave tank coloured with velocity for the irregular waves with a horizontal submerged cylinder for the time step = 650 s

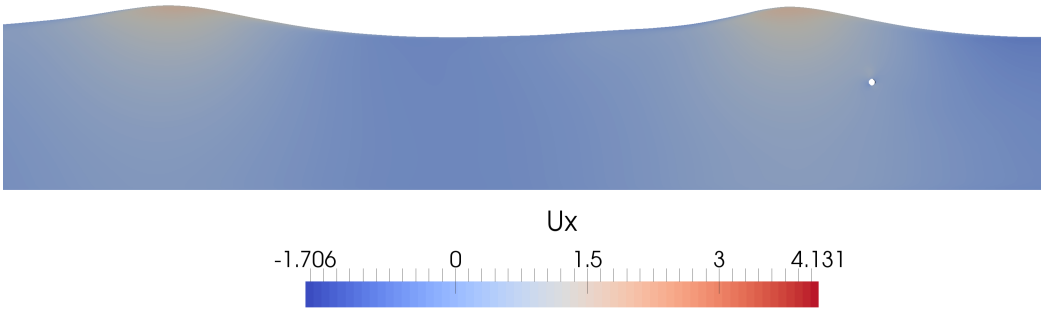

(b) Zoomed view of the numerical wave tank around cylinder for the time step = 650 s

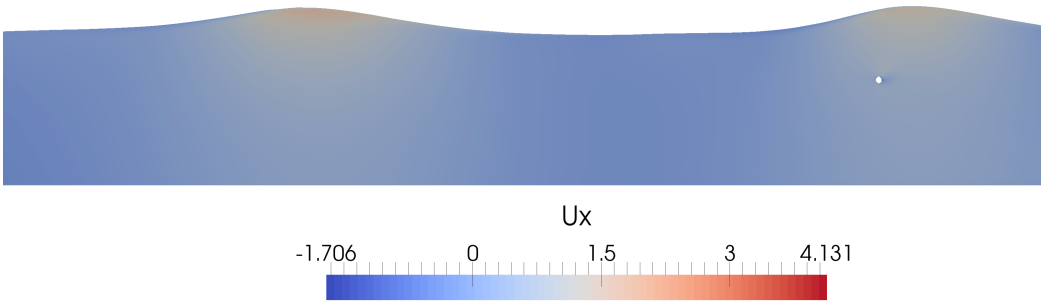

(c) Zoomed view of the numerical wave tank around cylinder for the time step = 682 s

Figure 5.10: $T_p = 3.2$ s, $dx = 0.05$ m, $H_s = 1.5$ m, Simulation time = 500 s

Chapter 6

Wave forces on a vertical cylinder

The study of wave forces on a vertical cylinder is important because of its applications in the offshore and the wind energy sector. Offshore structures, for example, an oil rig with a vertical plies platform and a wind turbine with the vertical pile foundation experience the irregular wave forces on the piles standing under the influence of waves. This chapter of the present work, deals with the calculation of the irregular wave forces on a single vertical cylinder using the numerical model REEF3D. The numerical wave force results for a vertical cylinder are first validated for the regular waves by comparing them with the Morison's formula and later irregular wave forces are computed for the same setup.

6.1 Numerical Wave Tank Setup

A vertical circular cylinder of diameter $D = 0.5$ m is placed in a 3D numerical wave tank. The cylinder is placed at the centre of the wave tank. The total length of the numerical wave tank is 18 m. The width and depth of the numerical wave tank is 5 m and 1 m respectively. The wave generation zone is 2.5 m long and the length of the beach is 5 m. The setup of the numerical wave tank is illustrated in the Figure 6.1. Four wave gauges are placed along the length of the numerical wave tank at $x =$ 3 m, 9.72 m, 10.26 m and 11.98 m, to study the hydrodynamics around the vertical cylinder under the irregular waves. The numerical simulations are done for the waves with the significant wave height $H_s = 0.03$ m. Tests are done with irregular waves with three different peak periods $T_p = 1.0$ s, 1.2 s and 1.4 s. For the case with $T_p =$ 1.2 s, simulations are carried out for three different grid size, $dx = 0.1$m, 0.05 m and 0.025 m. The simulation duration is chosen to be 500 s in each case.

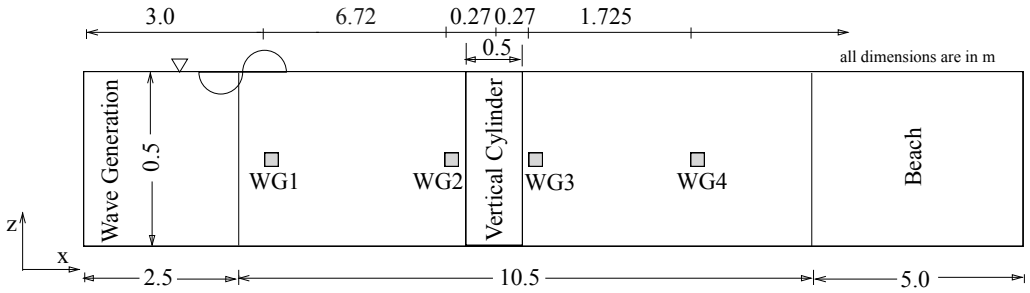

Figure 6.1: Numerical Wave Tank Setup for Vertical Cylinder

6.2 Validation with the regular waves

The numerical simulations are also done for the regular waves to validate the numerical model. The numerical force results are compared with theoretical force calculated using the Morison's formula. The Morison's formula computes the maximum and minimum value of force as 141.12 N/m and -141.12 N/m respectively. Figure 6.2 shown below demonstrates a good agreement between the theory and the numerical results. The force-time series results calculated using numerical model lie well within the force envelope calculated by the Morison's formula.

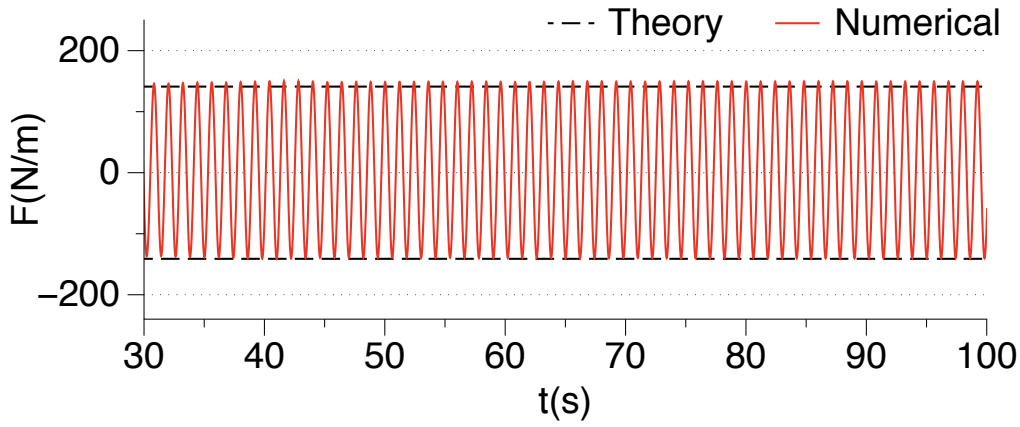

Figure 6.2: Comparison of numerical force with Morison's force for a vertical cylinder of $D = 0.5$ m for T=1.2s, $dx = 0.025$ m, $H = 0.03$ m

6.3 Irregular waves: grid convergence study

In this section of the chapter, a grid convergence study is performed. Simulations are run for the different grid sizes, $dx = 0.05$ m, 0.1 m and 0.25 m. The other parameters, the significant wave height $H_s = 0.03$ m, the peak time period $T_p = 1.2$ s, the cylinder diameter $D = 0.5$ m are kept constant. The simulations are run for a duration of

500 s. The Figure 6.3 shows the results for a force spectrum for the different grid sizes. It is observed from the Figure that the results with a grid size, $dx = 0.25$ m has two peaks, first peak has value, $F_{p1} = 1152\ N^2/Hz$ at the frequency, $f_{p1} = 0.73$ Hz. Second peak has the higher value, $F_{p2} = 1315\ N^2/Hz$ at the frequency, $f_{p2} = 0.81$ Hz. The frequency range corresponding to the higher $F_{p2}/3$ on both sides of the spectrum is 0.66 Hz to 0.88 Hz. Results with a grid size, $dx = 0.1$ m has the first peak with a value, $F_{p1} = 1410\ N^2/Hz$ at the frequency, $f_{p1} = 0.73$ Hz. Second peak has the higher value, $F_{p2} = 1756\ N^2/Hz$ at the frequency, $f_{p2} = 0.83$ Hz. The frequency range corresponding to the higher $F_{p2}/3$ on both sides of the spectrum is 0.62 Hz to 0.89 Hz. The force spectrum plot for a grid size, $dx = 0.05$ m shows the first peak with value, $F_{p1} = 1297\ N^2/Hz$ at the frequency, $f_{p1} = 0.73$ Hz. Second peak,F_{p2} has a higher value of 1782 N^2/Hz at the frequency, $f_{p2} = 0.83$ Hz. The frequency range corresponding to $F_{p2}/3$ is 0.60 Hz to 0.91 Hz. The spectrum plot is very smooth for this grid size.

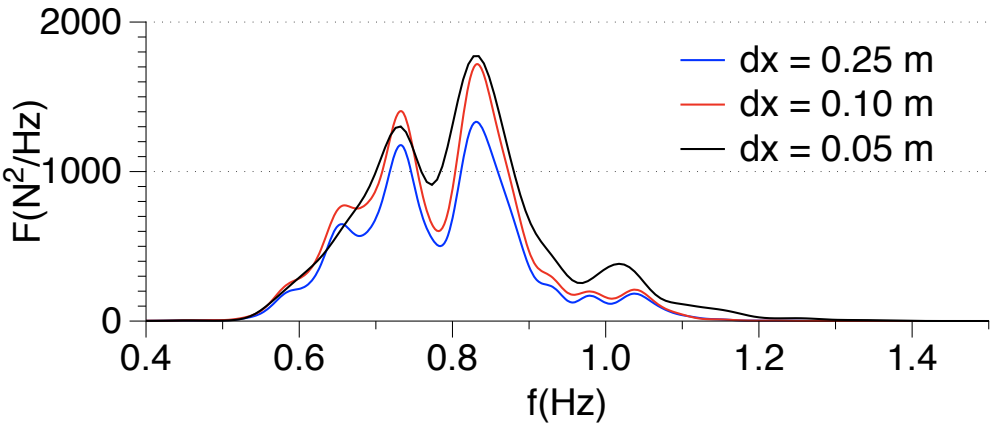

Figure 6.3: Grid Convergence Study for a Vertical Submerged Cylinder with $D = 0.5$ m, $T_p = 1.2$ s, $H_s = 0.03$ m

It can be inferred from the Figure 6.3 that coarser grid sizes do not have sufficient number of cells per wavelength to give good results, thus they show the wiggles and a lower value of peak. For the grid size, $dx = 0.05$ m, the number of cells per wavelength is between 50 to 70. The spectrum with finer grid is relatively broader as compared to the coarse grid spectra. Also, for this grid size, the spectrum plot is very smooth. It should be noted that, the spectra for all the grid sizes show two peaks. Their most of the spectrum values are concentrated around the two peak values. However, the decay of spectrum after the peak frequency is slightly more steeper than the rise of spectrum before the peak frequency.

The Figure 6.4 demonstrates the irregular wave propagation around the vertical cylinder. Figure 6.4a shows the wave propagation at time step = 500 s, free surface is coloured by the velocity contours.
It is clearly observed that the free surface of the wave tank consists of the waves with

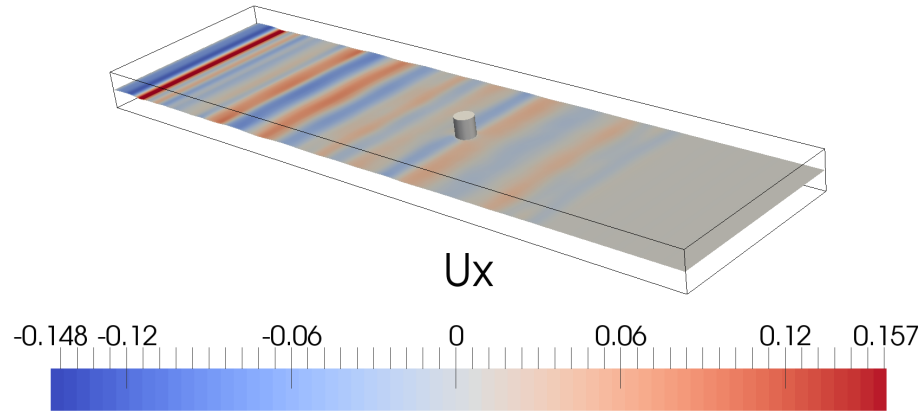

(a) Numerical wave tank with free surface coloured with velocity contours for the irregular waves with a vertical cylinder for the time step = 500 s

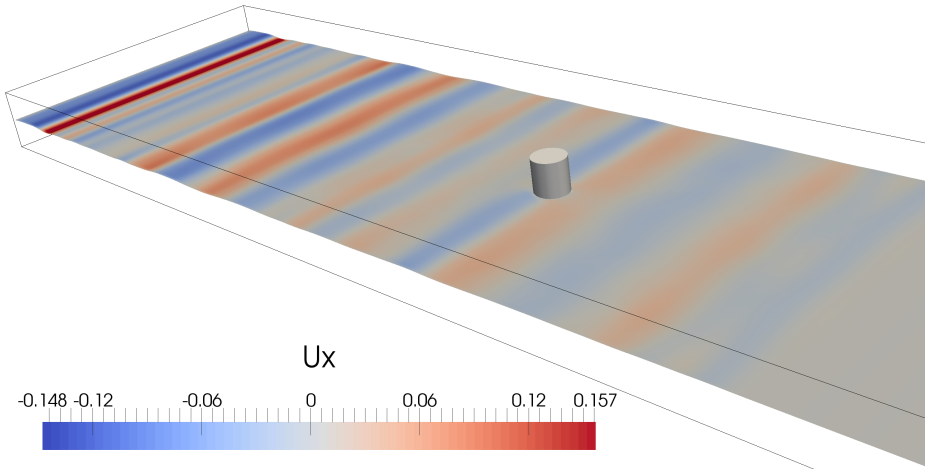

(b) Zoomed view of the numerical wave tank around vertical cylinder with free surface coloured with velocity contours for the irregular waves for the time step = 500 s

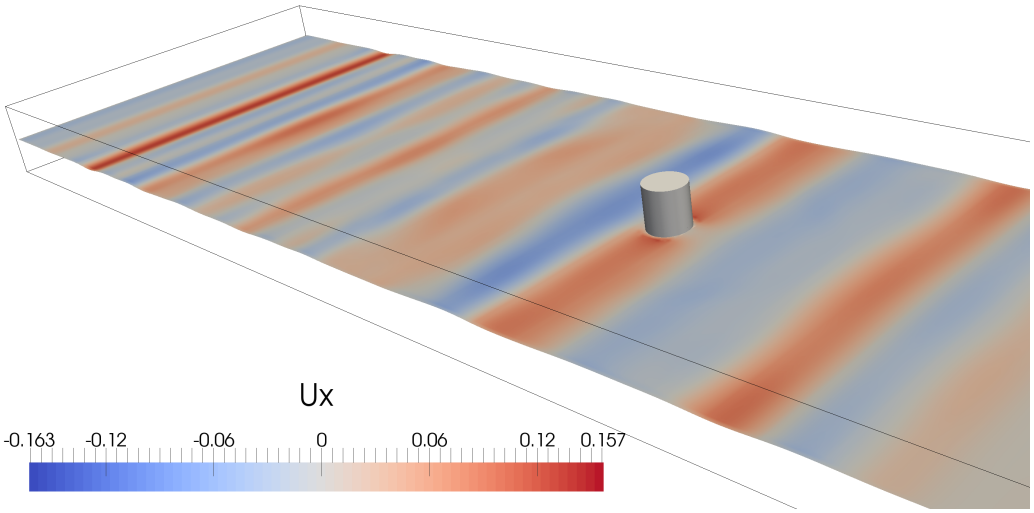

(a) Zoomed view of the numerical wave tank around vertical cylinder with free surface coloured with velocity contours for the irregular waves for the time step = 870 s

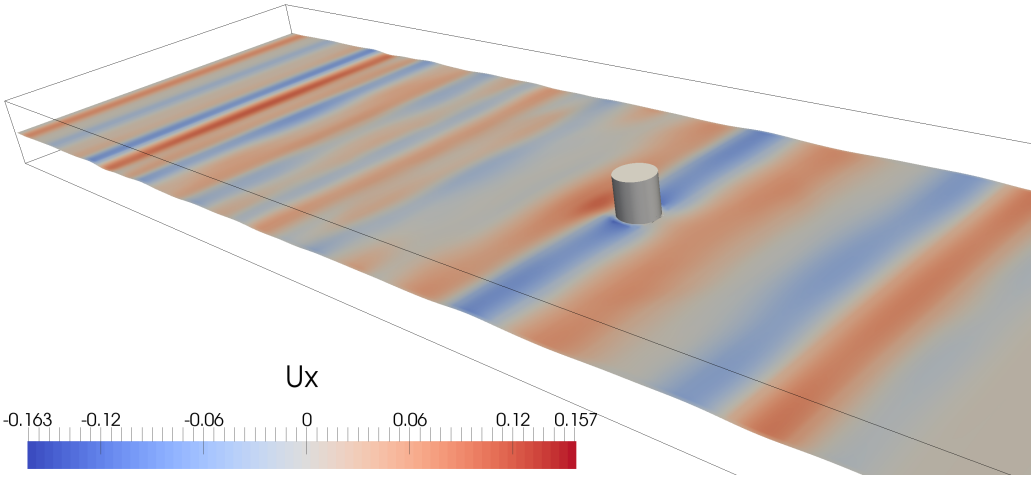

(b) Zoomed view of the numerical wave tank around vertical cylinder with free surface coloured with velocity contours for the irregular waves for the time step = 880 s

Figure 6.4: $D = 0.5$ m, $T_p = 1.2$ s, $dx = 0.05$ m, $H_s = 0.03$ m, Simulation time = 500 s

different velocities. This is due to the fact the irregular waves are superposition of regular waves of different time periods and wave heights. It can also be noted that at the end of the wave tank, the numerical beach absorbs all the waves. Thus, no velocity is observed towards the end of the wave tank. To understand the hydrodynamics around the cylinder, Figure 6.4b shows a zoomed view of the section around the cylinder for the same time step. The Figure 6.4c illustrates the hydrodynamics around cylinder for the time step = 870 s. The waves with positive velocity interacts with the cylinder and during this interaction slight concentration of the velocity takes place around the cylinder. This is also true for the Figure 6.4d which shows the time step = 880 s, when the waves with negative velocity interacts with the cylinder. Also, it can be observed in the Figure 6.4d that for the next wave with positive velocity, a concentration of the velocity occurs close to the cylinder before interacting with it. This is due to the flow contraction which happens around the cylinder when the waves pass around it. Also, an increase in turbulence takes place around the cylinder, which contributes to the increase in velocity around the cylinder as well.

6.4 Different Peak Periods

This section deals with study of the wave forces for a vertical cylinder under irregular waves with different peak periods. The simulations are performed for the peak wave periods, T_p = 1.0 s, 1.2 s and 1.4 s. The other parameters, significant wave height, H_s = 0.03 m, grid size, dx = 0.05 m, cylinder diameter, D = 0.5 m are kept constant. The Figure 6.5 shown below presents the wave force spectra for different peak wave periods. The wave force spectrum for a peak wave period, T_p = 1.4 s shows the peak value, F_p 2860 N^2/m at the frequency, f_p = 0.72 Hz. The frequency range corresponding to $F_p/3$ is 0.67 Hz to 0.78 Hz. Wave force spectrum plot for T_p = 1.2 s shows two peaks. The first peak, F_{p1} is lower and has value of 1297 N^2/Hz at the frequency, f_{p1} = 0.73 Hz. Second peak,F_{p2} has a higher value of 1782 N^2/Hz at the frequency, f_{p2} = 0.83 Hz. The frequency range corresponding to $F_{p2}/3$ is 0.60 Hz to 0.91 Hz. The waves with a peak period, T_p = 1.0 s are relatively shorter. The wave force spectrum for this period shows a peak value, F_p of 1670 N^2/m at the frequency, f_p = 1.00 Hz. The frequency range corresponding to $F_p/3$ is 0.89 Hz to 1.11 Hz.

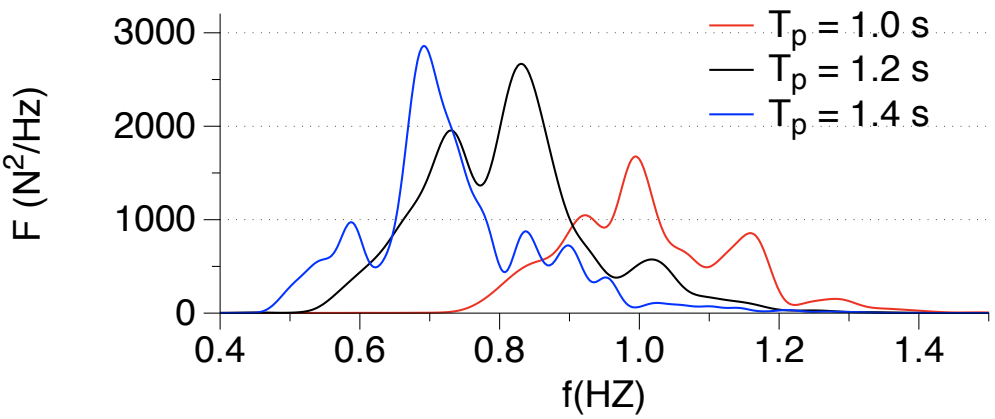

Figure 6.5: Study with different peak wave periods, T_p for a vertical cylinder with D = 0.5 m, dx = 0.025 m, H_s = 0.03 m

The above figure clearly illustrates that the waves with a lower value of peak period, T_p have a lower value of the peak in the force spectrum. This means that shorter waves exert less force on the vertical submerged cylinder as compared to the longer waves. The force spectrum for the waves with lower T_p = 1.0 s is relatively wider. It should also be noted that waves with T_p = 1.0 s and 1.4 s show a single prominent peak for the force spectrum, while waves with T_p = 1.2 s show two peaks. One peak with a lower value and the second peak with a higher value.

6.5 Comparison between irregular wave force and regular wave force

A comparison for the force spectrum is made between the regular and the irregular waves for the different cases with the different peak wave periods. In the current study, the numerical simulations are done for the two regular wave cases for a cylinder with diameter D = 0.5 m. Case 1 is with a wave height H = 0.03 m and a time period T = 1.2 s. The force spectrum for this case is compared with the force spectrum of irregular wave case with a significant wave height H_s = 0.03 m and a peak wave period T_p = 1.2 s. The Figure 6.6 shown below compares the wave spectrum for case 1 before and after the interaction with a vertical cylinder.

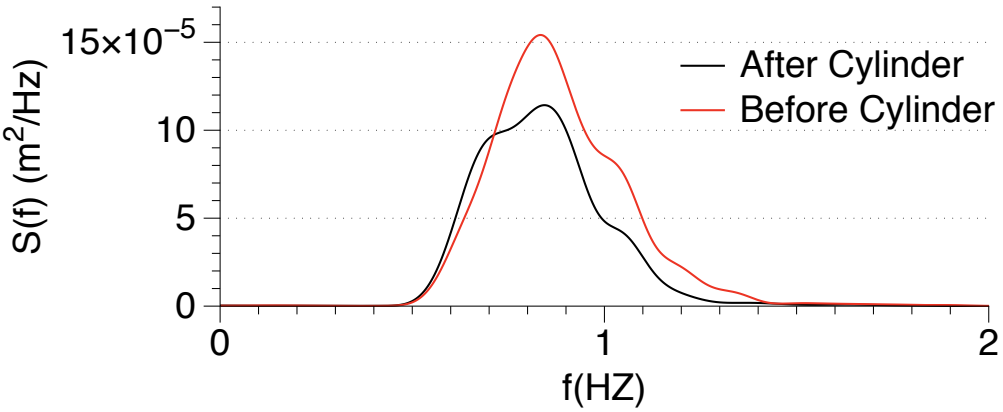

Figure 6.6: Comparison of wave spectra before and after the interaction with vertical cylinder of $D = 0.5$ m for T=1.2s, $dx = 0.025$ m, $H = 0.03$ m

It is observed that before the wave interaction with a vertical cylinder, the wave spectrum is single peaked at 0.83 Hz and the wave spectrum is spread between the frequency range of 0.42 Hz to 1.43 Hz. But after the interaction with cylinder, the peak value of the wave spectrum is reduced and also it shows a secondary peak at 0.69 Hz before the peak frequency. Also, the wave spectrum is relatively narrower limited to the frequency range between 0.42 Hz to 1.32 Hz. This is due to the fact that dissipation of wave energy has occurred during the interaction.
Case 2 is with a wave height $H = 0.03$ m and time period $T = 1.0$ s. The force spectrum for this case is compared with the force spectrum of the irregular wave case with a significant wave height $H_s = 0.03$ m and a peak wave period $T_p = 1.0$ s. A grid size $dx = 0.05$ m is chosen for the both cases. Simulations are run for a duration of 500 s. The Figure 6.7 shown below shows a comparison between the regular wave forces and the irregular wave forces for the both cases.

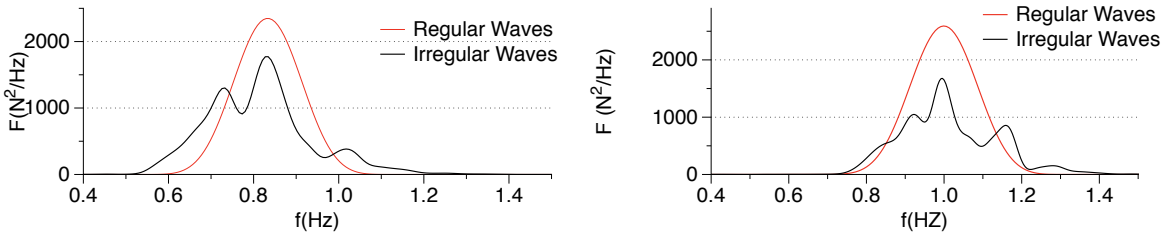

(a) Irregular Waves with $T_p = 1.2$ s, $H_s = 0.03$ m and Regular Waves with $T = 1.2$ s, $H = 0.03$ m

(b) Irregular Waves with $T_p = 1.0$ s and Regular Waves with $T = 1.0$ s

Figure 6.7: Comparison between Regular and Irregular Wave Force Spectra with $D = 0.5$ m, $dx = 0.05$ m

The Figure 6.7 shows that the regular waves exert more force as compared to the irregular waves. It is seen in Figure 6.7a that for the case with the values of T_p and

$T = 1.2$ s, the regular wave force spectrum has a single peak at frequency $f_p = 0.83$ Hz and the peak has value of 2350 N^2/Hz. The shape of the spectrum is symmetric and similar to the Bell's curve. On the other hand, the irregular wave force has two peaks. The first peak with value $F_{p1} = 1297$ N^2/Hz at the frequency $f_{p1} = 0.73$ Hz and the second peak F_{p2} has a higher value of 1782 N^2/Hz at the frequency $f_{p2} = 0.83$ Hz. The irregular wave force spectrum is asymmetric. It should be noted that the second peak frequency f_{p2} for the irregular wave case matches with the peak frequency f_p of the regular wave case. The Figure 6.7b demonstrates that for the case with the values of T_p and $T = 1.0$ s, the force spectrum with the regular waves show a higher peak value as compared to the force spectrum under the irregular waves. The force spectrum with regular waves is very smooth and shows a peak value $F_p = 2570$ N^2/Hz at $f_p = 1.0$ Hz. This spectrum is very smooth and free from any kind of the secondary peaks. The irregular wave force spectrum on the other hand, shows a lower peak value $F_p = 1670$ N^2/m at the frequency $f_p = 1.0$ Hz. The spectrum for the irregular wave force is slightly wider as compared to the regular wave spectrum.

The Figure 6.7 clearly shows that for both the cases, the regular wave force spectrum has a higher peak value. This might be due to fact that under the irregular waves, the significant wave height H_s as mentioned in chapter 3, represents the highest of one-third of the wave heights. So, remaining two-third components of the spectrum have a wave height lower than the $H_s = 0.03$ m, thus in turn have a lower energy. While, for the regular wave spectrum, all the waves are uniform with same wave height $H = 0.03$ m. All the waves in the regular wave spectrum have the same energy and tend to exert a higher force. Thus, the regular wave force spectrum shows a higher peak as compared to the irregular wave force spectrum.

Chapter 7

Conclusions and outlook

7.1 Conclusions

In this study, the irregular wave generation using the numerical model REEF3D is tested and validated. The testing for the empty wave tank is done in order to test the irregular wave generation and the propagation. The influence of the different numerical and hydrodynamic parameters on the results is studied. The parameters varied are the grid size, the peak wave period, the number of linear wave components and the length of simulation duration. Grid convergence test shows that for a coarser grids $dx = 0.05$ m and $dx = 0.025$ m, the numerical wave spectrum does not show a good match with the theory. The results with a grid size $dx = 0.01$ m show a very good agreement with the theoretically predicted spectrum. Thus, the grid size of $dx = 0.01$ m is chosen for the further testing.

Effects on the results by changing the number of linear wave components are also studied. Tests are performed for the linear wave component, $N = 25$ and 100. But, effects by changing the value of N do not seem to be significant. For the further testing, a value of $N = 25$ is chosen. Testing is also done for the different peak periods $T_p = 2.50$ s, 2.00 s, 1.18 s and 0.80 s. It is observed that for a higher value of the peak period, the wave spectrum is relatively narrow and all the energy is limited to the lower frequencies. As the peak wave period becomes less, the wave energy tends to spread over a wider range of the frequencies, and value of the spectrum peak is also reduced because of the widening of the spectrum. The numerical results show a good match for the higher peak wave periods but for a peak wave period $T_p = 0.80$ s, the results do not match with theory. This is due to the fact that the waves are shorter in this case and the grid points per wavelength are not sufficient for a good simulation. Thus, a higher grid resolution is required for this peak wave period.
Tests with a different length of simulation time show that the length of simulation affects the results as well. Tests with a shorter duration show that the waves need some time to evolve fully and to give good results. The tests with the simulation duration = 60 s, 120 s and 240 s show that the waves with higher frequencies are under

represented for the wave gauges located at the farther locations in the working zone of the flume. Simulation duration = 500 s gives good results for all the wave gauges. Testing is also done for the simulation duration of 1000s and 3600 s, but the results show that the improvement is not very significant and they are computational very expensive. So, for a good optimization between the accuracy and the computational time, a simulation duration of 500 s is chosen.
In the next section, the irregular wave propagation over a submerged bar is simulated. The numerical results are compared with the experimental observations. Simulations are performed for the two cases. One non-breaking wave case with a significant wave height, $H_s = 0.022$ m and second breaking wave case with a significant wave height, $H_s = 0.05$ m. Simulations with case 1 shows that the numerical model predicts accurately the hydrodynamical phenomena as observed in the experiment. The incident wave spectrum for the wave gauge located before the bar, shows that the spectrum is narrow with a single peak and most of the energy is restricted to a lower frequency range. Shoaling is expected as the wave propagates over the upslope due to decreasing water depth, this is clearly shown in the results by both experimental and numerical results. As, the wave propagates the wave spectra tends to spread over a wider range of frequencies and for the wave gauge located on the downslope of the bar, results show that the energy gets distributed more towards the higher frequencies than the lower frequencies. Also, some secondary small peaks disappear, this is shown both by the numerical and the experimental results. Simulations with case 2 show that breaking occurs, due to a larger wave height as compared to the water depth. Rest all hydrodynamic phenomena is same as in the case 1 apart from the breaking. Comparison of the last two wave gauges, which are located on the flat crest before the breaking occurs and on the downslope, respectively that the dissipation of energy takes place while breaking. This is shown by the lowering of the primary peak, also more energy is distributed to the higher frequency range.

The next section of this study validates the numerical model for the wave force on a horizontal submerged cylinder. The numerical model is first validated with the regular waves. The numerical wave forces for regular waves are compared with the experimental results for the same setup. Numerical model is tested for the cylinder with a diameter, $D = 0.21$ m. The simulations are performed for the grid sizes, $dx = 0.05$ m. The numerical force results show a very good agreement with the experimental force results. In the next section, a study is made for the irregular wave force. The simulations are performed for the grid sizes, $dx = 0.25$ m, 0.10 m and 0.05 m. The results with a grid size, $dx = 0.25$ m show a peak value much before than observed by the experiments and after that the spectrum decays very steeply. For the grid size, $dx = 0.10$ m the numerical force spectrum has a lower peak value than the experimental force spectrum. Also, the numerical spectrum is wider as compared to the experimental spectrum. Results with a grid size, $dx = 0.05$ m show a very good match with the experimental results. Thus, a grid size, $dx = 0.05$ m is chosen for the further study. Later, testing is done by varying the KC numbers by changing the value of the peak wave period, T_p. Results show that the wave spectrum with a higher value of T_p have

a higher peak value as compared to the wave spectrum with lower value of T_p. Also, the spectrum is relatively narrow for higher value of T_p. Thus, it can be concluded that the longer waves tend to exert a higher wave force on a horizontal submerged cylinder. It can be inferred that the numerical model REEF3D is able to simulate the similar behaviour as shown by the experiments for the horizontal submerged cylinder.

In the last section, a study is done on the behaviour of wave force on a vertical cylinder of diameter, $D = 0.5$ m for both the regular and the irregular waves. Firstly, the validation is done with the regular waves by comparing the regular wave forces with the force calculated using the Morison formula. Next, the numerical simulations are run for the irregular waves with the significant wave height, $H_s = 0.03$ m, the peak wave period, $T_p = 1.2$ s. Tests are run for the three different grid sizes, $dx =$ 0.25 m, 0.10 m and 0.05 m. A similar shape of the spectra is shown by all the cases. Two peaks are observed in the wave force spectrum. First peak observed at lower frequency has a lower value than the second peak observed at the higher frequency. The simulation with the coarse grid, $dx = 0.25$ m show significantly lower peaks as compared to the fine grid results. Results with the finer grids, $dx = 0.10$ m and 0.05 m tend to converge and show almost the similar peaks and a similar behaviour. A grid size, $dx = 0.05$ m is chosen for the further study.
Numerical simulations are run for different values of peak period, T_p. Three values of T_p =1.0 s, 1.2 s and 1.4 s are chosen. The results show that the waves with a higher value of T_p tend to have a higher peak value of the force spectrum. It can be inferred from this study that the longer waves will exert a higher value of force on a vertical cylinder. A study is also done to compare the regular and the irregular wave force spectrum keeping other parameters same. Two cases are studied, case 1 with the regular waves of $H = 0.03$ m and $T = 1.2$ s, which is compared with the irregular waves of $H_s = 0.03$ m and $T_p = 1.2$ s. Case 2 with the regular waves of $H = 0.03$ m and $T = 1.0$ s which is compared with the irregular waves of $H_s = 0.03$ m and T_p $= 1.2$ s. The results show that for both the cases, the regular wave force spectrum shows a higher peak value than the irregular wave force spectrum. The shape of the regular wave force spectrum is symmetric and similar to the Bell's curve. While, a irregular wave spectrum is asymmetric.
The present study concludes that the numerical model REEF3D can be successfully used to generate and study the irregular waves propagation, their interaction with a structure, the wave force calculations on the horizontal and the vertical cylinder. The numerical model is able to simulate the similar behaviour as observed in the experiments. Thus, the REEF3D can be used as a good tool to make numerical simulations for irregular waves.

7.2 Outlook

Above study shows that REEF3D has shown promising results for the wave interaction with the structures. However, it can be concluded that REEF3D is an effective tool to

make the first hand predictions, and is effective over the small spatial and the temporal domains. The potential of the model can thus be further enhanced to study a more complex wave-structure interaction for offshore wind turbine substructures, the more finer grid simulations, the cases with more cylinders with the different arrangements. And, in future with some more development, REEF3D can prove as a very efficient tool to cater with the real life wave hydrodynamics problems.

Bibliography

Adams, N., Shariff, K., 1996. A high-resolution hybrid compact-eno scheme for shock-turbulence interaction problems. Journal of Computational Physics 127, 27–51.

Afshar, M.A., 2010. Numerical Wave Generation in OpenFOAM. Master's thesis. Chalmers University of Technology.

Afzal, M.S., 2013. 3d numerical modelling of sediment transport under current and waves. Masters thesis, Norwegian University of Science and Technology .

Alagan, C.M., Bihs, H., Myrhaug, D., 2015. Characteristics and profile asymmetry properties of waves breaking over an impermeable submerged reef. Coastal Engineering 100, 326–36.

Arntsen, Ø.A., Krogstad, H.E., 2000. Linear Wave Theory, Part A: Regular Waves. Department of Civil and Transport Engineering, NTNU, Trondheim.

Barth, T., Ohlberger, M., 2004. Finite volume methods: Foundation and analysis. Journal of Computational Physics .

Bascom, W., 1964. Waves and beaches. Doubleday .

Batchelor, G.K., 1967. An introduction to fluid dynamics. Cambridge University Press ISBN 0-521-66396-2.

Beji, S., Battjes, J., 1993. Experimental investigation of wave propagation over a bar. Coastal Engineering 19, 151–162.

Berthelsen, P.A., Faltinsen, O.M., 2008. A local directional ghost cell approach for incompressible viscous flow problems with irregular boundaries. Journal of Computational Physics 227, 4354–4397.

Bosboom, J., M.J.F., S., 2011. Coastal dyanamics 1. lecture notes CT4305, Faculty TU Delft .

Chaplin, J., Subbiah, K., 1997. Large scale horizontal cylinder forces in waves and currents. Applied Ocean Research 19, 211–223.

Chella, A.M., Bihs, H., Myrhaug, D., Muskulus, M., 2015. Breaking characteristics and geometric properties of spilling breakers over slopes. Coastal Engineering 94, 4–19.

Chorin, A.J., 1968. Numerical solution of the Navier-Stokes equations. Mathematics of Computation 22, 745–762.

Clauss, G.F., Schmittner, G.E., St*ü*ck, R., 2005. Numerical wave tank- simulation of extreme waves for the investigation of structural responses, in: Proc., 24th International Conference on Offshore Mechanics and Arctic Engineering, Greece.

Courant, R., 1943. Variational methods for the solution of problems of equilibrium and vibrations. Bulletin of the American Mathematical Society 49, 1–23.

Courant, R., Friedrichs, K., Lewy, H., 1967. On the partial difference equations of mathematical physics. IBM Journal of Research and Development 11, 215–234.

Courant, R., Isaacson, E., Rees, M., 1952. On the solution of nonlinear hyperbolic differential equations by finite differences. Comm. Pure Appl. Math 5, 243–255.

Croce, R., Griebel, M., Schweitzwer, M., 2010. Numerical simulation of bubble and droplet deformation by a level set approach with surface tension in three dimensions. Journal for Numerical Methods in Fluids 62, 963–993.

Dommermuth, D.G., Yue, D.K.P., Lin, W.M., rapp, R.J., Chan, E.S., Melville, W.K., 1988. Deep-water plunging breakers: a comparison between potential theory and experiments. Journal of Fluid Mechanics 189, 434–442.

Engsig-Karup, A., P., 2006. Unstructured Nodal DG-FEM Solution of High-order Boussinesq-type Equations. Ph.D. thesis. Technical University of Denmark, Lyngby.

Erlebacher, G., Hussaini, Y., Shu, C.W., 1997. Interaction of a shock with a longitudinal vortex. Journal of Fluid Mechanics 337, 129–153.

Fletcher, R., 1976. Conjugate gradient methods for indefinite systems. Numerical Analysis, Lecture Notes in Mathematics, Springer Berlin Heidelberg , 73–89.

Goda, Y., Suzuki, Y., 1976. Estimation of incident and reflected wave in random wave experiment. Coastal Engineering .

Goullet, A., Choi, W., 2011. A numerical and experimental study on the nonlinear evolution of long-crested irregular waves. Physics of Fluids 23.

Griebel, M., Dornseifer, T., Neunhoeffer, T., 1998. Numerical Simulations in Fluid Dynamics. SIAM.

Harlow, F., Evans, M., 1957. Los alamos scientific laboratory report lams. LA-2 .

Harlow, F.H., Welch, J.E., 1965. Numerical calculation of time-dependent viscous incompressible flow of fluid with a free surface. Physics of Fluids 8, 2182–2189.

Harry, M., Zhang, H., Lemckert, C., Colleter, G., Blenkinsopp, C., 2011. Remote sensing of water waves: wave flume experiments on regular and irregular waves. 20th Australasian Coastal and Ocean Engineering Conference 2011 and the 13th Australasian Port and Harbour Conference 2011 , 138–143.

Harten, A., Engquist, B., Osher, S., Chakravarthy, S., 1987. Uniformly high-order accurate essentially non-oscillatory schemes iii. Journal of Computational Physics 71, 231–303.

Hestenes, M., Stiefel, E., 1952. Methods of conjugate gradients for solving linear systems. The Journal of Research of the National Institute of Standards and Technology , 49–409.

Higuera, P., Lara, L.J., Losada, I.J., 2013. Realistic wave generation and active wave absorption for navier-stokes models application to openfoam. Coastal Engineering 71, 102–118.

Hirt, C., Nichols, B., 1981. Volume of fluid (vof) method for the dynamics of free boundaries. Journal of Computational Physics 39, 201–225.

Hossain, M.S., Rodi, W., 1980. Mathematical modeling of vertical mixing in stratified channel flow. Second Symposium on Stratified Flows, Trondheim, Norway .

J. William Kamphuis, M., 1996. Experiments on design wave height in shallow water. Coastal Engineering .

Jacobsen, N.G., Fuhrman, D., Fredsøe, J., 2012. A wave generation toolbox for the open-source cfd library: Openfoam. International Journal for Numerical Methods in Fluids 70, 1073–1088.

Jacobsen, N.G., Fuhrman, D.R., FredsØe, J., 2011. A wave generation toolbox for the opensource cfd library: Openfoam. International Journal for Numerical Methods in Fluids 70, 1073–1088.

Jiang, G.S., Peng, D., 2000. Weighted ENO schemes for Hamilton Jacobi equations. SIAM Journal of Scientific Computing 21, 2126–2143.

Jiang, J., Shu, C.W., 1996. Efficient implementation of weighted eno schemes. Journal of Computational Physics 126, 202–228.

Johnson, C., 1987. Numerical solutions of partial differential equations by the finite element method. Cambridge University Press .

Kamath, A.M., 2012. Calculation of wave forces on structures using reef3d. Masters thesis, Norwegian University of Science and Technology .

Ladeinde, F., O'Brien, E., Cai, X., Liu, W., 1995. Advection by polytropic compressible turbulence. Physics of Fluids 7, 2848–2857.

Larsen, J., Dancy, H., 1983. Open boundaries in short wave simulations-a new approach. Coastal Engineering 7, 285–297.

Launder, B., Sharma, B., 1974. Application of the energy-dissipation model of turbulence to the calculation of flow near a spinning disc. Letters in Heat and Mass Transfer 1, 131137.

Liu, X.D., Osher, S., Chan, T., 1994. Weighted essentially non -oscillatory schemes. Journal of Computational Physics 115, 200–212.

Madsen, P.A., Murray, R., SØrensen, O.R., 1991. A new form of the boussinesq equations with improved linear dispersion characterstics. Coastal Engineering 15, 371–388.

Menter, F.R., 1993. Two-equation eddy-viscosity turbulence models for engineering applications. AIAA Journal 32, 1598–1605.

Mittal, R., Dong, H., Bozkurttas, M., Najjar, F., Vargas, A., Loebbecke, V.A., 2008. A versatile sharp interface immersed boundary method for incompressible flows with complex boundaries. Journal of Computational Physics 227, 4825–4852.

Morinishi, Y., Lund, T.S., Vasilyev, O.V., P., M., 1998. Fully conservative higher order finite difference schemes for incompressible flow. Journal of Computational Physics 143, 90–124.

Nwogu, O., 1993. Alternative form of boussinesq equations for nearshore wave propagation. Journal of waterways, Port, coastal and ocean engineering 119, 618–638.

Osher, S., F., L., 1996. High-order 2-dimensional nonoscillatory methods for solving hamilton-jacobi scalar equations. Journal of Computational Physics 123, 235–253.

Osher, S., Sethian, J., 1988a. Fronts propagating with curvature-dependent speed: algorithms based on hamilton-jacobi formulation. Journal of Computational Physics 79, 12–49.

Osher, S., Sethian, J.A., 1988b. Fronts propagating with curvature- dependent speed: Algorithms based on hamilton-jacobi formulations. Journal of Computational Physics 79, 12–49.

Osher, S., Shu, C.W., 1991. High-order essentially nonoscillatory schemes for hamilton-jacobi equations. SIAM Journal on Numerical Analysis 28, 907–922.

Paulsen, B.T., Bredmose, H., Bingham, H., 2014. An efficient domain decomposition strategy for wave loads on surface piercing circular cylinders. Coastal Engineering 86, 57–76.

Peng, D., Merriman, B., Osher, S., Zhao, H., Kang, M., 1999. A PDE-based fast local level set method. Journal of Computational Physics 155, 410–438.

Peric, M., Ferziger, J., 2001. Computational methods for fluid dynamics. Springer .

Rainey, R., 1989. A new equation for calculating wave loads on offshore structures. JFM 204, 295–324.

Richardson, L., F., 1910. The approximate arithmetical solution by finite differences of physical problems involving differential equations, with an application to the stresses in a masonry dam. Philosophical Transactions of the Royal Society of London. Series A, Containing Papers of a Mathematical or Physical Character 210, 307–357.

Rogers, W.E., Kaihatu, J.M., Hsu, L., Jensen, R.E., Dykes, J.D., Holland, K.T., 2007. Forecasting and hindcasting waves with the swan model in southern california bight. Coastal Engineering 54, 1–15.

Seiffert, B., Hayatdavoodi, M., Ertekin, R.C., 2014. Experiments and computations of solitary wave forces on a costal-bridge deck. part 1: Flat plate. Coastal Engineering 88, 194–209.

Shekari, M., M., S., 2013. An experimental study on the reshaping of berm breakwaters under irregular wave attacks. Applied Ocean Research 42, 16–23.

Shu, C.W., Oscher, S., 1988. Efficient implementation of essentially non-oscillatory shock capturing schemes. Journal of Computational Physics 77, 439–471.

Shu, C.W., Oscher, S., 1989. Efficient implementation of essentially non-oscillatory shock capturing schemes ii. Journal of Computational Physics 83, 32–78.

Shu, C.W., Zang, T.A., Erlebacher, G., Whitaker, D., Oscher, S., 1992. High order eno schemes applied to two- and three- dimensional compressible flow. Applied Numerical Mathematics 9, 45–71.

Stokes, G., 1846. British Association Report .

Suryanto, A., 2006. Estimation of incident and reflected waves in irregular wave experiments. Journal of the Indonesian Mathematical Society (JIMS) 12.

Sussman, M., Smereka, P., Osher, S., 1994. A level set approach for computing solutions to incompressible two-phase flow. Journal of Computational Physics 114, 146–159.

Tseng, Y.H., Ferziger, J.H., 2003. A ghost-cell immersed boundary method for flow in complex geometry. Journal of Computational Physics 192, 593–623.

Tucker, M., J., Pitt, E, G., 2001. Waves in ocean engineering. Elsevier ocean engineering book series, volume 5.

Van Leer, B., 1979. Towards the ultimate conservative difference scheme. Journal of Computational Physics 32, 101–136.

Von Arx, W.S., 1962. An introduction to physical oceanography. Addison-Wesley .

Van der Vorst, H., 1992. Bi-gstab: A fast and smoothly converging variant of bi-cg for the solution of nonsymmetric linear systems. SIAM J. Sci. Stat. Comput. 13, 631–644.

Wallin, S., Johansson, A.V., 2000. An explicit algebraic reynolds stress model for incompressible and compressible turbulent flows. Journal of Fluid Mechanics 403, 89132.

Walsteijn, F., 1994. Robust numerical methods for 2d turbulence. Journal of Computational Physics 114, 129–145.

Weinan, E., Shu, C.W., 1994. A numerical resolution study of high order essentially non-oscillatory schemes applied to incompressible flow. Journal of Computational Physics 110, 39–46.

Wheeler, J., 1970. Method for calculating forces produced by irregular waves. Journal of Petroleum Tech. 249, 359–367.

Wilcox, D., 1994. Turbulence modeling for cfd. DCW Industries Inc. La Canada, California .

Xu, F., Perrie, W., Toulany, B., Smith, P.C., 2007. Wind-generated waves in hurricane juan. Ocean Modeling 16, 188–205.